

GaAs nanowires: from doping to plasmonic hybrid devices

THÈSE N° 6838 (2016)

PRÉSENTÉE LE 22 JANVIER 2016

À LA FACULTÉ DES SCIENCES ET TECHNIQUES DE L'INGÉNIEUR
LABORATOIRE DES MATÉRIAUX SEMICONDUCTEURS
PROGRAMME DOCTORAL EN SCIENCE ET GÉNIE DES MATÉRIAUX

ÉCOLE POLYTECHNIQUE FÉDÉRALE DE LAUSANNE

POUR L'OBTENTION DU GRADE DE DOCTEUR ÈS SCIENCES

PAR

Alberto CASADEI

acceptée sur proposition du jury:

Prof. F. Sorin, président du jury
Prof. A. Fontcuberta i Morral, directrice de thèse
Prof. R. Grange, rapporteuse
Dr M. Tchernycheva, rapporteuse
Prof. F. Stellacci, rapporteur



ÉCOLE POLYTECHNIQUE
FÉDÉRALE DE LAUSANNE

Suisse
2015

Starting a new journey scares us,
but after each step we realize
how dangerous it was standing still.
— Roberto Benigni

To my parents...

Acknowledgements

Four years of PhD consists of moments of work, discussion, disappointment, satisfaction and fun. Besides everything I learned, I am very grateful for the people that during this journey walked along with me. This work would not have had the same spirit and enthusiasm without the academic, cultural, social and human support provided by them.

I am very grateful to **Prof. Anna Fontcuberta i Morral**. She always supported me in the difficult moments and she gave me the possibility to follow my ideas and show my motivations. I thank her for teaching me her human side before her career achievements, for always continuing to look for solutions without giving up, for building a very diverse and friendly group and for bringing us so much chocolate.

I would like to thank my colleagues. I shared with them much more than the scientific work and they have been for me like a big family. I would start by thanking **Federico Matteini**: after his arrival we have shared ideas, experiences, activities, offices, houses, and friends. He was always ready to help me. **Esther Alarcon Llado** for the great scientific advisory, for listening and for supporting my work and my projects. **Gözde Tütüncüoglu** for the apéro, the evenings, nice moments together and for taking care of the MBE. **Anna Dalmau** for the skiing, the hiking, the discussions about life and her clean room advice. **Yannik Fontana** because he was ready to help even without me asking. **Daniel Rüffer** for sharing his great technical competences, for his help in contacting the nanowires and for his positive and friendly attitude. **Martin Heiss** for his great academic competences and his help in the lab. **Jelena Vukajlovic Plestina** for the nice stories and the kind invitations to eat Croatian food. **Jil Schwender** for working with me, for her joy and for her laugh. **Mohammad Ramezani** for his enthusiasm and motivation that transformed the routine work into something exciting. **Heidi Potts** for the nice conversations and the after work activities. I would also express my gratitude to **Francesca Amaduzzi**, **Eleonora Russo Averchi**, **Dmitry Mikulik**, **Sonia Conesa-Boj**, **Eleonora Frau**, **Martin Friedl**, **Jean-Baptiste Leran**, **Luca Francaviglia** and **Luca Del Carro** for their help, for transmitting me motivation, for the support and for contributing to this very social and friendly group.

A big thank goes to:

Carlo Colombo, to introducing me to the PhD world, for guiding me in many decisions, for supporting me and showing me how to tackle life combining the analytical prospect with the human side.

Acknowledgements

Luca Dal Negro, for his great advisory in optics and plasmonics, for the productive collaboration on the nanowire/nanoantennas platform, for hosting me in Boston, for giving me the opportunity to become a friend before a collaborator and for all the extra-work activity we did together during his sabbatical year and during my stay in Boston.

Dominik Zumbühl, for hosting me several times in Basel University, for his great help in contacting modulation doped nanowires, for all his advice and all the effort he put into this project.

Jaime Gomez Rivas, for our fruitful collaboration on the nanowire/Yagi-Uda antennas platform.

The professors and researchers who evaluated and supported my work. In particular, **Francesco Stellacci** who followed my work year by year giving advice and ideas. **Jagadish Chennupati** for never judging me, but always providing a true and kind support. **Jordi Arbiol**, **Erik Bakkers**, **Jean-Christophe Harmand** and **Philippe Caroff** for the nice scientific conversations, for their interest in my work, their advice and for making me feel part of the scientific community.

Yvonne Cotting and **Monika Salas-Tesar**, for helping me to solve the administrative problems within and outside EPFL.

The entire staff of CMI, for doing a downright amazing job and providing a professional and friendly work environment. Without their professional advice and support, the sample fabrication would have been much more painful. In particular, I would like to thank **Zdenek Benes**, **Guy-François Clerc**, **Cyrille Hibert**, **Philippe Langlet**, **Joffrey Pernollet**, **Giancalo Corradini** and **Didier Bouvet**.

The collaborators **Emanuele Francesco Pecora**, **Jacob Trevino** and **Carlo Forestiere**, for the optical measurements and simulations of the nanowire/nanoantennas plasmonic coupling; **Peter Krogstrup**, for growing Be-doped GaAs nanowires and helping in the electrical measurements and interpretation of the results, **Grzegorz Grzela**, for the discussions on the nanowire directional emission, **Reza Zamani**, for the TEM images, **Pirmin Weigele**, for teaching me how to use the lab instruments in Basel.

Sergio Allegri, **Daniele Dragoni** and **Fedeico Valmorra**, for the great and successful collaboration in organizing the EDMX winter school *New Materials from Physics to Applications 2015*

My friends for providing emotional support and for being with me in the disappointment and happiness.

Un ringraziamento speciale va ai miei genitori **Marzia Alessi** e **Massimo Casadei** per avermi incoraggiato e aiutato in tutti i momenti della mia vita.

Infine vorrei ringraziare **Line Zolliker** per il suo sostegno, per rendere felici i miei momenti tristi e per essere stata sempre al mio fianco.

Abstract

Semiconductor nanowires (NWs) are filamentary crystals with the diameter ranging from few tens up to few hundreds of nanometers. In the last 20 years, they have been intensively studied for the prospects that their unique quasi-one dimensional shape offers to both fundamental and applied science. More recently particular attention has been dedicated to use NWs as building blocks for nano-electronic devices. In this thesis we investigate the electro-optical properties of NWs in order to put some light on the mechanisms governing the electrical transport and the light coupling between NWs and metal nanostructures.

We investigate Be and C doping in GaAs NWs synthesized by Molecular Beam Epitaxy (MBE). We obtain a doping control over a large range of densities and we identify a new *in situ* incorporation path. Since strong surface impurity scattering in III-V materials degrade the electronic performances, we grew NWs passivated with an AlGaAs layer and we investigate their properties. The NW passivation allows for the increase of the electron mean free path by a factor of almost 10. In addition, we designed AlGaAs/GaAs modulation doping NWs. The modulation doping structure allows for the to enhancement of the NW electron mobility revealing excellent properties for the realization of nano-electronic devices. We calculate the electron distribution in the modulation doped NWs and we observe a six-fold symmetry with six 1D electron channels when the carrier concentration is high, while for low concentrations, electrons are delocalized in the GaAs NW core.

Thanks to their special interaction with light, semiconductor NWs have opened new avenues in photonics, quantum optics and solar energy harvesting. Here, we design a new system composed of a NW and an array of nanoantennas. Initially, we successfully demonstrated the plasmonic coupling between NWs and nanoantennas, observing an electric field enhancement in the NW as a function of the nanoantenna's gap distance. This finding represented an initial step toward the development of coupled nano-structures for the realization of a new generation of solar cells, detectors and non linear optical devices. Near field coupling was also used between a NW and Yagi-Uda antennas to obtain directional emission. In particular the precise tuning of the Yagi-Uda dimensions and positions leads a strong variation of the NW emission, being able to change this from backward to forward.

One of the major challenges for NWs full technological deployment has been their strong polarization dependence in light absorption and emission. Here, we demonstrate that a hybrid structure formed by GaAs NWs with a highly dense array of bow-tie antennas is able to modify the polarization response of a NW. As a result, the increase in light absorption for transverse polarized light changes the NW polarization response, including the inversion of

Acknowledgements

the polarization response. We calculated that the absorption of transverse polarized light can be enhanced up to 15 times. We also fabricate several electrical devices proving our calculated predictions.

Keywords:

GaAs nanowires, doping, plasmonic, nanoantenna, modulation doping, mobility, transistors, absorption and light interaction.

Riassunto

I nanofili semiconduttori sono filamenti di cristallo con un diametro che varia da decine a centinaia di nanometri. Negli ultimi 20 anni, sono stati studiati estensivamente per via della loro forma quasi uno-dimensionale che offre prospettive per la scienza fondamentale e applicata. Recentemente è stata dedicata una particolare attenzione all'uso di nanofili come parti fondamentali di nano-dispositivi elettronici. In questa tesi investighiamo le proprietà ottiche ed elettriche dei nanofili in modo da gettare un po' di luce sui meccanismi che governano il trasporto elettrico e l'interazione della luce fra nanofilo e strutture metalliche.

Abbiamo investigato il drogaggio ottenuto con Be e C nei nanofili di GaAs sintetizzati con l'epitassia da fasci molecolari. Abbiamo ottenuto un controllo del drogaggio per un'ampia gamma di concentrazioni e abbiamo identificato una nuova via per l'incorporazione del drogaggio *in situ*. La forte dispersione sulla superficie dovuta alle impurità, degrada le prestazioni dei materiali III-V. Per questo abbiamo cresciuto nanofili con uno strato di AlGaAs per rendere passiva la superficie e ne abbiamo studiate le proprietà. La passivazione dei nanofili permette di aumentare di un fattore 10 il libero cammino medio degli elettroni. In aggiunta abbiamo progettato nanofili di AlGaAs/GaAs con drogaggio modulato. Questa struttura permette di aumentare la mobilità degli elettroni nel nanofilo mostrando proprietà eccellenti per la realizzazione di nano-dispositivi elettronici. Abbiamo calcolato la distribuzione elettronica nei nanofili con drogaggio modulato e abbiamo osservato: ad alte concentrazioni, una geometria a sei simmetrie con canali uno-dimensionali, mentre a basse concentrazioni, una delocalizzazione degli elettroni nel nucleo del nanofilo.

Grazie alla loro speciale interazione con la luce, i nanofili semiconduttori hanno aperto nuove strade nel capo della fotonica, ottica quantistica e produzione di energia solare. Qui, abbiamo progettato, un nuovo sistema formato da un nanofilo e una matrice di nano-antenne. Inizialmente, abbiamo dimostrato con successo l'accoppiamento plasmonico fra il nano-filo e le nano-antenne, riportando un aumento del campo elettrico nel nanofilo in funzione della distanza delle nano-antenne. Questa scoperta rappresenta il primo passo verso lo sviluppo di una nano-struttura accoppiata per la realizzazione di una nuova generazione di celle solari, rivelatori e dispositivi non-lineari. Inoltre abbiamo utilizzato l'accoppiamento del campo vicino fra un nanofilo e antenne Yagi-Uda per generare emissione direzionale. In particolare il preciso controllo delle dimensioni e della posizione delle antenne Yagi-Uda, provoca una forte variazione nell'emissione del nanofilo, da una direzione all'altra.

Una delle più grandi sfide nell'utilizzo tecnologico dei nanofili è stata la loro forte dipendenza dalla polarizzazione della luce sia in assorbimento che in emissione. Qui dimostriamo che

Acknowledgements

una struttura ibrida formata da un nano-filo e da una matrice densa di antenne bow-tie è in grado di modificare la dipendenza alla polarizzazione del nanofilo. Come risultato, l'aumento dell'assorbimento della luce per una polarizzazione trasversale cambia la risposta alla polarizzazione del nano-filo. Abbiamo calcolato che l'assorbimento della luce trasversale può aumentare fino a 15 volte. Abbiamo anche realizzato numerosi dispositivi elettrici che validano le nostre previsioni teoriche.

Parole chiave:

GaAs nanofili, drogaggio, modulazione drogaggio, plasmonica, nanoantenna, mobilità, transistori, assorbimento e interazione della luce.

Contents

Acknowledgements	i
Abstract (English/Italiano)	iii
1 Introduction	1
1.1 Towards the nanoscale	2
1.2 III-V materials	3
1.3 III-V nanostructures on Silicon	4
1.4 Nanowires	5
1.4.1 Novel physical properties	6
1.4.2 Application oriented studies	7
1.5 Overview of the thesis	8
2 Fabrication and characterization techniques	11
2.1 Nanowire growth	12
2.2 Ohmic contacts on GaAs Nanowires	13
2.3 Device fabrication	15
2.4 Electrical characterization	16
2.4.1 Electrical transport measurements:	17
2.4.2 Electron beam induced current (EBIC):	18
2.5 Optical techniques	19
2.5.1 Dark-field scattering:	20
2.5.2 Second harmonic generation (SH-G):	20
2.5.3 Photo-conductivity measurements:	22
3 Doping, incorporation paths and surface effects	25
3.1 NW doping	26
3.2 Doping incorporation paths	28
3.3 Surface states and passivation	30
3.3.1 Fermi Level pinning at the surface	30
3.3.2 Surface passivation with AlGaAs	31
3.4 Be-doped NWs: new incorporation path	32
3.4.1 Device fabrication	32
3.4.2 Measurements and discussion	32

Contents

3.5	C-doped NWs: surface passivation effects	36
3.5.1	Device fabrication	36
3.5.2	Hole mobility in function of doping and surface	37
3.5.3	Minority carrier mean free path	40
3.6	Conclusions	42
4	Modulation doped nanowires	43
4.1	Modulation-doped GaAs	44
4.2	Modulation doping simulations of the nanowires geometry	47
4.2.1	Doping concentration	47
4.2.2	Spacer width	50
4.2.3	$Al_xGa_{1-x}As$ alloy composition	50
4.3	Electron mobility in nanowires	51
4.3.1	GaAs:Si nanowires	51
4.3.2	AlGaAs/GaAs:Si modulation doping nanowires	53
4.4	Conclusions	53
5	Photonic-plasmonic coupling of GaAs NWs and nanoantennas	55
5.1	State of the art	57
5.1.1	Metallic nanoparticles: light interaction	57
5.1.2	Optical properties of semiconductor nanowires	59
5.1.3	Nanowires and metal nanostructures: coupled systems	60
5.2	Sample preparation	61
5.3	Photonic-plasmonic coupling of GaAs NWs with disk nanoantennas	63
5.3.1	Dark field scattering	63
5.3.2	Near-field distribution	66
5.3.3	Second harmonic generation (SH-G)	68
5.4	Controlling the directional emission of GaAs NWs with Yagi-Uda antennas	70
5.5	Results and discussions on NW/Yagi-Uda systems	71
5.5.1	Fourier spectroscopy microscope	71
5.5.2	Fourier spectroscopy measurements	72
5.6	Conclusions	73
6	Nanoantennas to control the nanowire polarization response	75
6.1	Introduction	76
6.2	NW photonics	76
6.2.1	Resonant modes	77
6.2.2	Cross-section and substrate dependence	77
6.3	Geometry optimization of the nanoantennas	79
6.4	Absorption in the hybrid system	82
6.5	Photocurrent response	86
6.6	Photocurrent scanning map	88
6.7	Conclusions	89

Conclusions	91
A List of publications	113
B List of conferences and seminars	115

1 Introduction

This thesis is dedicated to the study of GaAs nanowires opto-electrical properties for the realization of technological devices. Several aspects have been analyzed such as the doping mechanisms, the surface states, the light interaction and the coupling with optical nanoantennas.

In the first part of this introductory chapter are presented some historical facts of technological down-scaling of devices and integrated circuits. We introduce the advantages in having III-V materials and the main issues related to the III-V integration on Si. Then, semiconductor nanowires are presented as the best platforms to investigate new nanoscale physical properties and the best building blocks for new technological devices. In the second part of the chapter we define the scope and the overview of the thesis. Here we introduce the opto-electrical properties of GaAs nanowires that are discussed in the following chapters: the doping mechanism, the surface states effects, the light interaction and the coupling with optical nanoantennas.

1.1 Towards the nanoscale

In 1947 at Bell Lab J. Bardeen, W. Brattain and W. Shockley invented the bipolar transistor. This revealed to be the most important invention of the century, giving official birth to the electronic industry. In 1956 the Nobel Prize was given to the three American physicists for their contribution on semiconductor materials and for the discovery of the transistor effect. In the same period (1950) another invention was intended to revolutionize the electronic industry: the integrated circuits. This discovery was performed by Jack Kilby, who devised a way to assemble all the components of a circuit (resistor, transistor, capacitors, etc) on the same die. This idea was the initial step that brought the electrical technology to develop by improving performances, reducing the costs and it begins the age of the micro-technology.

For four decades the micro-technology experienced an explosive growth. Integrated circuits became more and more powerful and complex. Silicon is the semiconducting material mostly used in the fabrication of transistor and other active electronic components and the field developed at the point that the last historical period is also indicated as *the age of silicon*. In 1965 Gordon E. Moore, cofounder of Intel observed that the number of transistors in a dense integrated circuit doubles approximately every two years. His prediction was proved to be accurate for several decades, and his law was used in the semiconductor industry to guide long-term planning and to set targets for research and development. This possibility to concentrate more and more components in an integrated circuit brought at two main consequences: the reduction of the costs and the reduction of the sizes. This down scaling has been the driving force in the development of more advanced microelectronic devices. Indeed, the down-scaling brought significant advantages also in decreasing the consumption power and increasing the circuit speed. In 1959 the Nobel Prize Richard Feynman proposed to shrink the electrical components to their physical limit and he pronounced his famous sentence "*there is plenty of space at the bottom*". In recent years the microelectronic industry reached this limit, pushing the components sizes to the nanoscale.

In the last years the miniaturization has decreased considerably. The difficulties and the costs to further reduce the size are combined with the apparition of new physical properties peculiar to the nanoscale systems. In particular when the size reduces to the nanometer scale, surface effects, quantum confinements, electrical band alignment, light interaction etc... can be profoundly modified respect to the bulk material counterpart. The scope of this thesis is to characterize GaAs nanowires. They are ideal candidates as building block of future technological devices and in addition to this promising role they constitute an ideal platform for: (i) investigate new physics effects, mostly related to surface and interfaces properties, (ii) study the physics associated to quantum confinement and small dimensions, (iii) create materials with properties (crystalline structure, electrical bands, stress relaxation etc.) different from the bulk materials, (iv) reaching complex architecture and combine material with different lattice parameters.

1.2 III-V materials

The reduction in size is leading to better performances in integrated circuits, but it is not the only way to improve the devices electronic properties. Electrical devices can be faster if realized with materials with high mobility and devices for absorbing and emitting light would largely benefit from active materials with direct band-gap. For these reasons modern opto-electronics has also turned the attention to III-V compound semiconductors.

III-V compounds are formed by elements from the III group in the Mendeleev table (like: Al, Ga and In) and elements from the V group (like N, P, As and Sb). The most common materials are GaAs, InAs, GaP, AlAs and InP, which show a one to one stoichiometry. Many of the III-V compounds have high mobility due to the carrier effective masses lighter than those in silicon. Some of them present a direct band-gap and they have a range of spectral absorption covering a wide part of the solar spectrum. These peculiar characteristics are optimal for opto-electronic devices and make III-V ideal materials for applications like lasers, light-emitting diodes (LED), detectors, optical systems and photovoltaics. For this last application the world record efficiency is today obtained with a III-V multi-junction solar cell.

A big advantage in the nowadays technology would be the integration of III-V materials with silicon. This would lead to the combination of the mature, consolidated and world-wide spread platform (Si platform) with the advantageous optical and electric properties of III-V materials. Unfortunately their combination presents challenging issues for a monolithic integration. The most important is probably the *lattice mismatch*. The lattice constant of GaAs is $a_{GaAs} = 5.65 \text{ \AA}$ while the one of Si is $a_{Si} = 5.43 \text{ \AA}$. The lattice constants of other IV and III-V semiconductors are shown in figure 1.1.

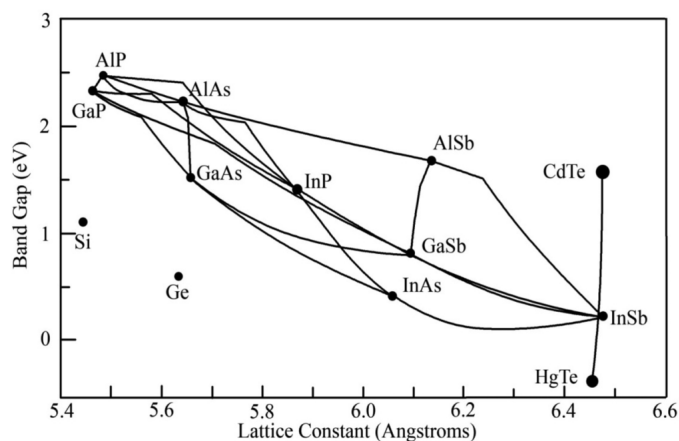


Figure 1.1: Band-gaps of group V and the mayor III-V bynary semiconductor materials as function of the cubic lattice parameter. In open access from [1].

The lattice mismatch is the major responsible of the formation of cracks and defects at the

interface between the two materials. The lattice mismatch is associated with a strain which need to be relaxed in order to have a defect free junction. This happens when the mismatch is accommodated by the elastic deformation of the lattice. This process is particular important in nanostructures where this lattice deformation can quickly reach the surface and be fully relaxed. If the strain energy cannot be completely relaxed the mismatch is accommodated with the formation of dislocations at the interface. Different materials can also have large differences in *thermal expansion coefficient*. The mismatch of GaAs and Si is 60 % at room temperature. This mismatch causes thermal stress and can lead to the distortion of the crystalline lattice and subsequent the degradation of material optical properties and the formation of bending and cracks. Finally, silicon and GaAs have similar crystalline structure (fcc), but silicon is a *non polar* material (both sublattices are occupied by the same atom), while GaAs is a *polar* material (the two fcc lattices have different atoms, one is occupied by Ga atoms and the other by As atoms). The coexistence of areas with As atoms and Ga atoms at the Si-GaAs interface leads to the formation of As-As and Ga-Ga bonds that should be avoided in order to preserve the device performances. Some of these effects can be minimize by growing III-V nanostructures on a Silicon platform.

1.3 III-V nanostructures on Silicon

If the III-V compound semiconductors are in form of nanostructures, the lattice and thermal mismatch can be overcome. This is thanks to the reduced contact area with the silicon substrate and the small nanostructures dimensions that allow to elastically relaxed the crystalline lattice at the interfaces. Due to the presence of a moderate strain the formation of dislocations and defects at the interface between the two materials can be reduced or eliminated. Moreover, the single event nucleation of III-V nanostructure on Si drastically reduces the probability of Ga-Ga and As-As bonds at the interface. For their opto-electrical properties and the adaptability to be integrated on Si, III-V nanostructures hold the promise to be building blocks of future opto-electronics devices. The first step for their integration on Si is the need to synthesize them in a reproducible way, with a control in morphology, composition, crystalline structure and dimensions. Indeed, size and crystalline structure strongly affect the material band structure and therefore its electronic properties. Defects like twins or stacking faults reduce the electron mobility and introduce recombination centers and deep traps. Finally, the control on the composition is important for the realization of heterostructure, the engineering of the semiconductor bandgap (i.e. the $Al_xGa_{1-x}As$ bandgap depends on the Al percentage x) and the control of the doping. Much progress have been done in the last years both in the III-V integration on Si and in the engineering nano-devices with superior performances. The most promising nanostructure blocks are the nanowires.

1.4 Nanowires

Nanowires (NWs) are filamentary crystals with diameters ranging from few tens up to few hundred nanometers with an aspect ratio of at least 10. They can be made of different materials, including insulators (e.g. SiO_2 , TiO_2), semiconductors (e.g. Si, Ge, GaAs, InAs, InSb, ZnO) and metals (e.g. Ag, Au, Ni). The synthesis of high aspect ratio crystals was performed by Wagner and Ellis in 1964 [2] and almost 30 years later, in the early 90s, the topic was recovered by the Hitachi group [3]. This research group in Japan reported on growth of InAs and GaAs whiskers with diameters of only a few tens of nanometers. With a clear vision, they identified the change of the crystal structure in the whiskers from zinc-blende to wurtzite, pointed out the importance of the surface passivation of the NWs and demonstrated for the first time a functional NW device: a light emission from a p-n junction NW [4]. These results have triggered the attention of several research groups and in a short time period the field of NWs has become one of the attractive topics in low-dimensional semiconductor physics, attracting more and more research groups worldwide and resulting in a constantly increasing number of publications over the years. Figure 1.2 shows the number of papers published each year for the last 20 years found in WEB of Science searching for "Nanowires".

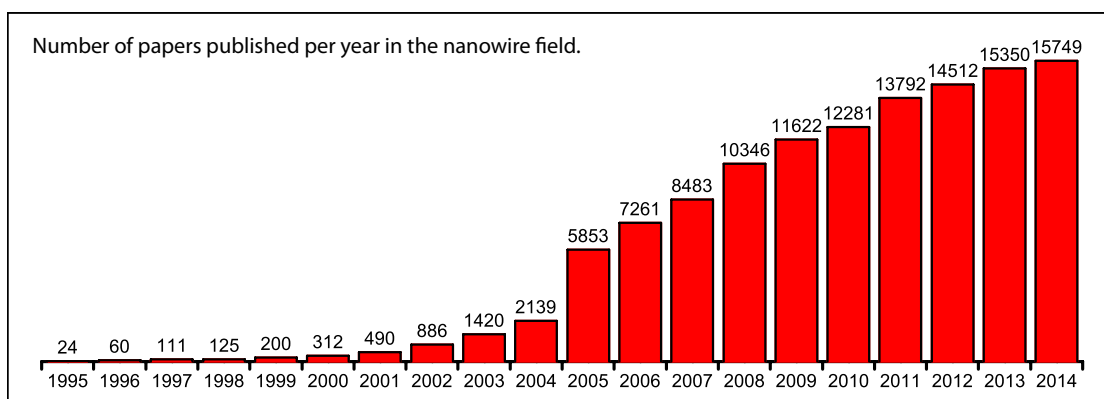


Figure 1.2: Number of papers published per year in the NW field. The data are obtained for "Nanowires" as topic in 'WEB of Science'.

A large variety of materials, from metals to semiconductor has already been synthesized in the form of nanowires through several growth mechanisms and fabrication techniques. The most common fabrication techniques are the *Molecular Beam Epitaxy* (MBE), the *Metal Organic Vapor-Phase Epitaxy* (MOVPE), the *Chemical Beam Epitaxy* (CBE), the *Chemical Vapor Deposition* (CVD) and the *Laser Ablation* (LA). In this thesis MBE is used to grow GaAs nanowires on Si substrate. MBE has the advantage to be extremely clean and it allows to produce ultrapure structures with very high crystalline quality.

NWs constitute an elegant platform for achieving novel physical properties. The small dimensions, the high quality material, the high surface-volume ratio and the large control in the

growth allow us to study and engineer *physical phenomena* not accessible in bulk materials. Furthermore, the unique one-dimensional geometry makes NWs ideal candidates for scaling down the dimensions of *opto-electronic devices*.

1.4.1 Novel physical properties

NWs have been shown to have the ideal dimensions and properties to support novel physical properties. For example a signature of *Majorana fermions* have been found in hybrid superconductor-semiconductor NWs. This work was published in 2012 from the group of L. P. Kouwenhoven and E. Bakkers attracting the interest of the full physics community. NWs are here represented as the best candidates for the investigation of these particular particles [5]. Majorana fermions are particles identical to their own antiparticles and they have been theoretically predicted to exist in topological superconductors. For the first time evidence of these particles has been experimentally observed in InSb NWs.

From the perspective of materials science these one-dimensional crystals are especially interesting because they allow for the combination of *different materials in the form of heterostructures*. Due to their small diameter, the strain can be relaxed in a more effective manner, thus enabling the combination of materials with a large lattice mismatch. Consequently, combinations of materials otherwise not possible in bulk can lead to the development of different technologies. Particularly interesting is the growth of Ge/Si core/shell NWs which has been used to create 1D hole gas systems [6] and high performance field-effect transistors [7]. Strain induced by different lattice parameters and thermal properties offers additional degrees of freedom for tailoring materials, but often at the expense of dislocation generation, wafer bowing, and cracks. The group of L. Miglio eliminated these drawbacks by epitaxial growth of Ge and SiGe crystals onto micrometer-scale tall Si pillars [8]. Faceted crystals were shown to be strain- and defect-free.

An additional important point is the existence of the wurtzite structure in NWs. While most of the III-V bulk materials (arsenides and phosphides) crystallize in a zinc-blende structure, NWs can crystallize in pure zinc-blende, pure wurtzite or a mixture of both. This gives direct access to the physical properties of the wurtzite phase. Because the energy position of the band-gap of the two crystalline structures is different, it is possible to combine these structures to *engineer the band-gap* of a material. One of the major challenges toward Si NW based photonic devices is controlling the electronic band structure of the Si NW to obtain a direct band-gap [9]. Predictions of NW band-gap modification have shown that the band structure modulation with lattice strain is strongly dependent on the crystal orientation and diameter of Si NWs [10]. In the case of $\langle 100 \rangle$ and $\langle 111 \rangle$ Si NWs, tensile strain enhances the direct band-gap characteristic, whereas compressive strain attenuates it. $\langle 110 \rangle$ Si NWs have a different strain dependence in that both compressive and tensile strain make Si NWs exhibit an indirect band-gap. More recently, S. Assali *et al.* demonstrated the conversion of indirect band-gap semiconductors into direct semiconductors by tailoring the crystal structure [11]. The approach was shown for

GaP and AlP, and by transferring the crystal structure epitaxially it can be tested for a variety of other materials.

The possibility to grow core-multi-shell NWs allows for the fabrication of complex heterostructures with a unique geometry. For example, modulation doping structures can host a high-mobility electron gas, similarly to high-mobility two-dimensional electron gases (2DEGs), but wrapped around the core. Due to the prismatic shape of the core and to electron-electron interaction, in the NW core channel the electron gas will not be uniformly distributed at the heterointerfaces, but will localize along six *quasi-1D channels* at the edges of the interface, to maximize the average electron-electron distance [12]. Depending on the doping density and, possibly, the applied gate potential, the charge density reshapes between quasi-1D and quasi-2D distributions and moves between facets and edges localization. This might also have an impact on the effectiveness of different scattering mechanisms in different regimes. The first demonstration of such unambiguous 1D- and 2D electron channels and the respective charge carrier properties in these advanced NW-based quantum heterostructures is presented in 2013 by S. Funk *et al.* [13]. With the same core-multi-shell system in 2013 the group of A. Fontcuberta i Morral demonstrated the self-assembly of a high-quality quantum-dot in NW using two basic components, GaAs and AlAs. Individual *quantum dots* are bright and spectrally pure emitters of highly anti-bunched light, with non-resonant excitation and positioned just a few nanometres from the NW surface [14]. This constitute an extremely interesting platform for both the investigation of quantum dot physical properties and NW applications as single-photon sources.

1.4.2 Application oriented studies

In strict relation with novel and interesting physical properties come a broad area of applications based on NW devices. One that has attracted an increasing amount of attention is surely the *solar cell*. The new geometrical degree of freedom introduced by the building of radial p-n junctions gives the possibility of engineering solar cells using less material without sacrificing efficiency. The first theoretical considerations on this topic were published in 2005 by Atwater and coworkers [15]. Large light absorption and efficient carrier extraction have been indicated as requirements for the realization of NW based solar cells. Much progress has been made in this direction and in 2013 J. Wallentin *et al.* showed the fabrication of an InP NW array solar cell achieving an efficiency of 13.8%. This work was aimed to demonstrate that photovoltaics based on NW arrays could reduce cost and materials consumption compared with planar devices and exhibit relatively high efficiency of light absorption and carrier collection. The same year P. Krogstrup *et al.* demonstrated that an optimal NW p-n junction combined with optimal light absorption can lead to a solar cell efficiency above the Shockley-Queisser limit. They showed this by studying photocurrent generation for a single core-shell p-i-n junction vertical GaAs NW solar cell grown on a silicon substrate [16]. The enhanced light absorption is shown to be due to a light-concentrating property of the standing NW and the results imply new limits for the maximum efficiency obtainable with III-V based NW solar cells.

The development of the fabrication techniques and the possibility of homo and heteroepitaxy also allowed for the introduction of different NW-based optoelectronic devices. In 2001 Duan *et al.* demonstrated that single electrically-contacted InP NWs with a p-n junctions grown along the NW axis can work as *electronic transistors* [17]. NWs also proved to be optical waveguides in which Fabry-Pérot modes gave rise to lasing as reported by Huang *et al.* in 2001 for zinc oxide (ZnO) NWs [18]. These discoveries led to the demonstration of electrically driven NW *lasers* in 2003 [19]. In this field much progress was made and thanks to the NWs' small dimensions and the large surface to volume ratio, in 2014 Themistoklis *et al.* built a plasmonic NW laser with time pulses shorter than 1 *ps*. These were generated thanks to surface plasmon polaritons (electromagnetic excitations at metal-dielectric interfaces) on a ZnO NW. Spontaneous recombination, gain switching and gain recovery have all been shown to be accelerated compared with conventional ZnO photonic NW lasers.

One of the main disadvantages in NWs is that the large surface area introduces traps that can limit the NW's electrical properties. For this reason NW mean free paths and carrier mobilities are shown to be reduced in comparison with their bulk counterparts. One of the most investigated geometries to overcome the surface effects is coating with a wider band-gap material. GaAs/AlGaAs core shell NWs structures have been shown to present electron mobilities approaching the bulk limits and carrier lifetime significantly improved in comparison with single GaAs NWs [20, 13, 21]. This thesis is also contributing to the investigation of this geometry which is deeply investigated in chapter 4.

NWs have been used also for building high density packed arrays of light emitting diodes, which could have superior brightness [22, 23] and nanoscale efficient sensors [24, 25, 26]. They have also been interfaced with living cells [27, 28]. In fact their small diameter can reduce the invasiveness and the high surface area provides proper cell-NW communication. Finally, they can be also used as efficient thermoelectric devices, because of the combination of poor thermal conductivity and good electrical conductivity [29, 30].

1.5 Overview of the thesis

In this thesis, we investigate the electrical and optical properties of GaAs NWs. In chapter 2 we define all of the fabrication and characterization techniques used in the following chapters. The device fabrication was performed at EPFL in the *Centre of MicroNano Technology* (CMi), the electrical measurements in our laboratory: *Laboratory of Semiconductor Materials* (LMSC) and the optical measurements both in LMSC and in Boston University.

In chapter 3 the NWs' doping mechanism is investigated. Doping is fundamental for the realization of electronic devices. This characterization is performed with resistance and field effect measurements on single NWs. The analyzed GaAs NWs are doped with Be and C with different p-type doping concentrations. In our work we observed that Be diffuses from the surface shell into the core of the NW. We indicate this as a 'new' *in situ* incorporation path for the doping in addition to the doping incorporation through the droplet and through the

vapor-solid growth. We, then, show that the NWs are conductive and that we have doping control over a large range of values between $6 \cdot 10^{17}$ and $2 \cdot 10^{19} \text{ cm}^{-3}$.

Because of the large surface-volume ratio, the surface has a dominant role in the NW electrical properties. In order to avoid the formation of deep traps at the NW surface we grow NWs with a GaAs-AlGaAs core-shell structure. The hole (majority carriers) mobility, depends on the doping concentration and on the surface treatment. We surprisingly found that for low doping, the unpassivated NWs have higher mobilities than the corresponding passivated ones. We relate this effect to the partial migration of holes from the doped shell into the intrinsic core where they have higher mobility. To the best of our knowledge, this work is the first work reporting this unexpected behavior. On the other hand, electron-beam-induced-current (EBIC) showed that the AlGaAs passivation layer increases the electron (minority carriers) mean free path by one order of magnitude in comparison with unpassivated NWs, from 20 to 190 *nm*.

In thin films, modulation doping of structures allows the formation of a 2D electron gas and devices with electron mobilities higher than bulk materials. In chapter 4 we simulate, with NextNano, modulation doping structures in NWs. For a high doping concentration, we observe the creation of a six-fold symmetry with six 1D channels, while for low doping, electrons are delocalized inside the core. Several geometries are analyzed in order to investigate the influence of the doping layer on the carrier distribution. We found that a high carrier concentration in the core can be achieved both by increasing the doping and by increasing the doped layer thickness.

In the last part of the thesis, chapter 5 and 6, we focus on the coupling between gold nanoantennas and NWs. We design an array of nanoantennas around single GaAs NWs and we investigate the system with dark field scattering and second harmonic generation measurements. Both measurements and calculations show the system coupling and the enhancement of the NW absorption in the infrared region. Near field coupling is also used to modify the NW emitted light. In fact, Yagi-Uda antennas have been engineered around a NW in order to obtain directional emitted light. We then design a NW/bow-tie antennas system in order to maximize the NW absorption for transverse polarized light and in the visible range. For the first time we demonstrate the possibility to tune the NW light polarization response. We also demonstrate an absorption enhancement of 3 times related to the nanoantennas' effect. Finally, with this work we show that the NW/nanoantenna platform gives the opportunity to engineer the light interaction response.

2 Fabrication and characterization techniques

Nanowires are filamentary crystals with the diameter in the order of a few to 200 nm. Thanks to their special geometry and reduced dimensions, they are expected to play an important role and offer new findings for this century's technology and basic science.

In this chapter, the growth of semiconductor nanowires via molecular beam epitaxy is introduced, paying particular attention to the vapor liquid solid mechanism of GaAs nanowires. We extended the explanation of nanowire growth to the fabrication of radial heterostructures. After this, the principles for the fabrication of nanowire based electrical devices are discussed. In the last part of the chapter are described the electrical and spectroscopy techniques used in this thesis. These techniques are particularly developed for characterization at the nanoscale and provide information both on the physical properties and on the technological performances of nanowire based devices.

2.1 Nanowire growth

NWs are most commonly obtained by the Vapor-Liquid Solid mechanism (VLS), proposed for the first time by Wagner and Ellis in 1964 [2]. This method described the growth of silicon whiskers from Si gas phase atoms, in the presence of a liquid gold droplet used as catalyst. This process is based on the ability of gaseous species to be absorbed in a liquid metal droplet and precipitate in the solid form underneath leading to the NW growth.

Since the experiment by Wagner and Ellis, gold has been the catalyst most commonly used for NW growth. Even if it has important advantages for controlling the growth, it introduces deep levels in Si [31] and in other semiconductor materials like GaAs [32, 33]. In 2008 Fontcuberta *et al.* demonstrated the Ga-assisted synthesis of GaAs NWs by Molecular Beam Epitaxy (MBE) on GaAs substrates [34, 35] and later on Si substrates [36]. In our group we use MBE because it is favored among other techniques for obtaining very high purity samples thanks to its ultra-high vacuum conditions, to the absence of chemical precursors and to the extreme purity of the source materials. The growth of GaAs NWs with MBE on a SiO_2 layer proceeds as follows. When Ga and As sources are opened, ad-atoms and molecules reach the substrate where they can be absorbed. At high temperatures, As molecules will desorb while Ga ad-atoms will diffuse and form droplets on the substrate. When the Ga droplets reach supersaturation the GaAs NW growth starts at the droplet/substrate interface. This process is schematically depicted in figure 2.1.

During growth, Ga acts as a liquid reservoir for GaAs deposition and determines the NW diameter. For high Ga rate, low V/III beam equivalent pressure (BEP), the NW diameter tends to increase over time because Ga accumulates in the droplets and enlarges them. It is possible to reach a dynamical steady state by increasing the V/III ratio. This leads to a constant droplet size and it turns to a constant diameter along the wire. If the ratio becomes too high, the Ga droplets shrink over time leading to a tapered geometry [37]. The complete consumption of the Ga droplets is necessary to stop the VLS mechanism.

VLS conditions strongly affect the NW crystalline structure. The use of a Ga droplet leads to a prevalent zinc-blende crystal structure. Several works have analyzed the conditions for which NWs adopt a zinc-blende (ZB) or wurtzite (WZ) structure and how it is possible to favor one or the other [38]. In many cases it was found that the key elements were the V/III ratio and the contact angle. In addition to the crystalline structure, the control of the VLS

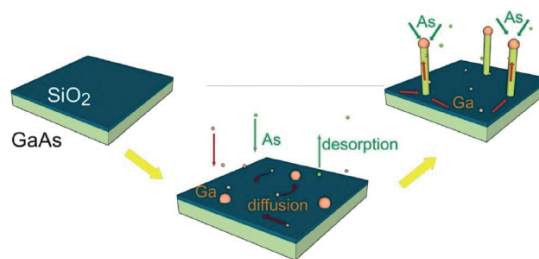


Figure 2.1: Cartoon of the VLS growth model. On the SiO_2 layer, the seeds of the GaAs NWs nucleate and grow, being continuously fed by the Ga adatoms that diffuse from the neighboring SiO_2 surface, and form droplets. The Ga droplets act as catalyst for the NW growth. The As_4 molecules are then impinging on the Ga top droplet and after the droplet saturation they precipitate leading to the GaAs crystalline growth of the nanowire [35]. Copyright ©2008, American Physical Society.

mechanism is also fundamental for the NW growth direction [39, 40], the NW density on the substrate [41, 42] and NW shape [43, 44].

After the VLS growth an additional step can be performed in order to grow a layer around the existing NWs. The radial growth is realized using conditions of two dimensional epitaxy and is of fundamental importance in: *(i)* creating different types of doping necessary for the realization of solar cells [45, 46, 16], photodetectors [47] or LEDs [48, 49], *(ii)* passivating the surface states and confining the electrical carriers to the core in order to improve the electronic performance [12, 50, 51, 20], *(iii)* generating quantum wells or quantum dot structures [14, 52] and *(iv)* integrating systems with different properties [53, 54]. In our group extensive studies have been done by M. Heigold and D. Spirkoska [55, 39], in order to find the optimal conditions for establishing radial growth on the (110) facets of self-catalyzed GaAs NWs. They concluded that radial growth occurs when the temperature is decreased down to 460°C and the As_4 pressure is increased up to $1.8 \cdot 10^{-5}$ mbar. By doing this the droplet gets crystallized, with the following interruption of the axial VLS growth and the diffusion of Ga atoms is suppressed leading to a more directional deposition.

In order to fabricate opto-electronic devices, dopant atoms need to be incorporated in the NWs. The more efficient and less invasive way is to incorporate the doping during the NW growth. In this way, the incorporation paths depends on the NW growth conditions. This topic will be deeper analyzed in the next chapter.

2.2 Ohmic contacts on GaAs Nanowires

Semiconductor NWs have attracted intense interest because their promise to act as building blocks in opto-electronic applications. For this to become a reality NW devices require both n- and p-contacts with very low specific contact resistances. In the electrical contact, the carriers have to tunnel through the electronic barrier formed at the metal/semiconductor interface. The barrier height is defined by the metal-semiconductor work function difference. The work functions Φ are shown in figure 2.2.

Whether a given metal-semiconductor junction is an ohmic contact, or Schottky barrier, depends on the Schottky barrier height, Φ_B , of the junction. For a sufficiently large barrier height, where $e\Phi_B$ is significantly higher than the thermal energy kT , the semiconductor is depleted near the metal and behaves as a Schottky barrier. For lower Schottky barrier heights, the semiconductor is not depleted and instead forms an ohmic contact to the metal. In addition, the barrier thickness, is inversely proportional to the square root of the doping level in the semiconductor. When the barrier thickness is small the carriers can tunnel through it, in this case we have the formation of an ohmic contact. Low-doped semiconductors tend to have a diode-like I-V characteristic where charge carriers only can flow in one direction. For a low doped semiconductor, the realization of ohmic contacts is therefore more difficult. In this section, ohmic contacts on GaAs NWs are analyzed for both p- and n-doping.

Au-alloys are by far the most used material to make ohmic contacts on GaAs due to their reliability, excellent contact resistivity, and usefulness over a wide range of doping levels [56]. Many works on ohmic contacts are reported in literature. For p-type GaAs the most used metal contacts are formed by Ti/Pd/Ti/Au [57] or Pd/Ti/Au [46]. Typical NW contact resistances can range between $1\text{ K}\Omega$ for high doping level ($> 5 \cdot 10^{18}\text{ cm}^{-3}$) to several $M\Omega$ for doping level below 10^{18} cm^{-3} [58].

The fabrication of contacts to p-GaAs is favored both due to the higher density of states in the valence band and the lower hole barrier. Therefore, low-resistive p-contact to GaAs are reported in NWs. One of the critical tasks is the realization and characterization of highly doped n-type GaAs NWs [59]. As a consequence, the fabrication of low resistance n-contacts is more difficult. One of the first reports on ohmic contacts to n-GaAs NWs is from Gutsche *et al.* in 2011 [60]. In their study they report the fabrication and characterization of Ge/Au ohmic contacts on GaAs followed by a rapid thermal annealing. The thermal annealing ensures the Ga out-diffusion and the Ge in-diffusion required to obtain good ohmic contacts. The best ohmic contacts were obtained with a metal stack of Ge/Ni/Ge/Au annealed at 320°C and with Pd/Ge/Au at 280°C . In this last configuration

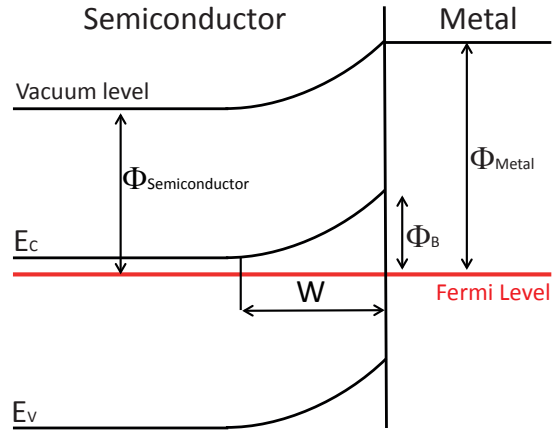


Figure 2.2: Band diagram for metal-semiconductor junction at zero bias (equilibrium). Shown is the graphical definition of the Schottky barrier height, Φ_B , for an n-type semiconductor as the difference between the inter-facial conduction band edge E_C and Fermi level E_F . W represent the junction barrier thickness.

Pd forms Ga-rich compound during the Pd-GaAs reaction and rapidly and uniformly penetrates the inter-facial native oxide leading to a contact resistance of less than $3 \cdot 10^{-7}\text{ }\Omega\text{cm}^2$. One shall mention that Au facilitates the out-diffusion of Ga that creates excess numbers of Ga vacancies into which Ge can diffuse [61]. Because of the small NW volume, at temperatures higher than 320°C , the increased Ga out diffusion might be very detrimental for the NWs [60]. An example of contacts on n-type GaAs NWs is shown in this thesis in chapter 4.

Particularly challenging is the formation of ohmic contacts on GaAs/AlGaAs core-shell NWs. The AlGaAs capping layer is an elegant solution to preserve the carriers from the influence of surface defects without introducing strain due to lattice matching and to engineer modulation doped structures. Unfortunately since the access to the conductive core is screened by the insulating AlGaAs shell, the formation of ohmic contacts is demanding. Two approaches are possible: etching of the AlGaAs shell or using GeAu alloys as metal contact followed by rapid thermal annealing. In the first approach citric acid/ H_2O_2 is the best candidate to selectively etch the AlGaAs/GaAs structures [62]. The etch rate and volume ratio between citric acid and H_2O_2 are strongly dependent on the Al concentration. This technique has been successfully

applied in this thesis to contact passivated p-doped NWs [51], observing an etching rate of 1.4 nm/s for an $Al_{33}Ga_{67}As$ shell.

The use of AuGe compounds is particularly necessary for modulation doped structures. Here the doping sits on the AlGaAs shell while the carriers are moving into the core. For this reason the etching of the shell would modify the NW electronic properties. Wirths *et al.* in 2012 report on the preparation of ohmic contacts on modulation-doped GaAs/AlGaAs core-shell NWs by the use of a contact layer system consisting of 5 nm Ni, 90 nm AuGe of eutectic composition (12 wt. % Ge), 25 nm Ni, and 100 nm Au [63]. They systematically varied the annealing time and temperature finding the optimal parameters to achieve ohmic contacts in a modulation doped GaAs/AlGaAs core/shell NW. The NW

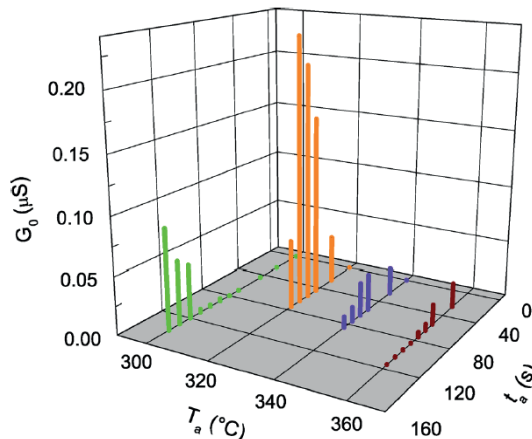


Figure 2.3: Conductance G_0 for a set of NWs for different annealing time t_a and temperatures T_a . Copyright ©2012, AIP Publishing LLC [63].

2.3 Device fabrication

In this section, the fabrication process of our devices is described. In order to electrically contact individual NWs, they are transferred onto an insulating substrate. As a substrate, we use Si and silica wafers covered with 200 nm of SiO_2 produced by dry oxidation. To transfer the NWs, we cut a piece of the grown substrate, put it into a small beaker with isopropanol and insert it into a bath with ultrasound. The ultrasonic waves detach the NWs from the growth substrate and bring them in solution. Then, by simply dropping droplets of this solution with dispersed NWs onto the substrates, the NWs are transferred. In order to fabricate the devices the following lithography steps have been developed. The substrate consists of an oxidized Si substrate with a grid of metal markers. The markers have circular shapes because it leads to the most precise and reliable detection by the electron beam lithography (e-beam). The center position of a circle is independent of its diameter. This makes the pattern tolerant to over- or under-exposure in photo-lithography. The described markers are shown in figure 2.4a.

Optical microscopy is then used to localize the NWs on the substrate. The optical images should contain the framing markers, which can be recognized by an automated software developed by Daniel Ruffer and Martin Heiss [64]. This software encodes the relative position on the wafer and it has a sub-micron precision in the alignment. The position is determined via shape recognition algorithms leading to an accuracy of less than 50 nm . We then use the Ebeam (Vistec EBPG5000) to position the contacts and the nanoantennas as shown in figure 2.4b. MMA and PMMA resist layer are spin coated on the substrate before the e-beam

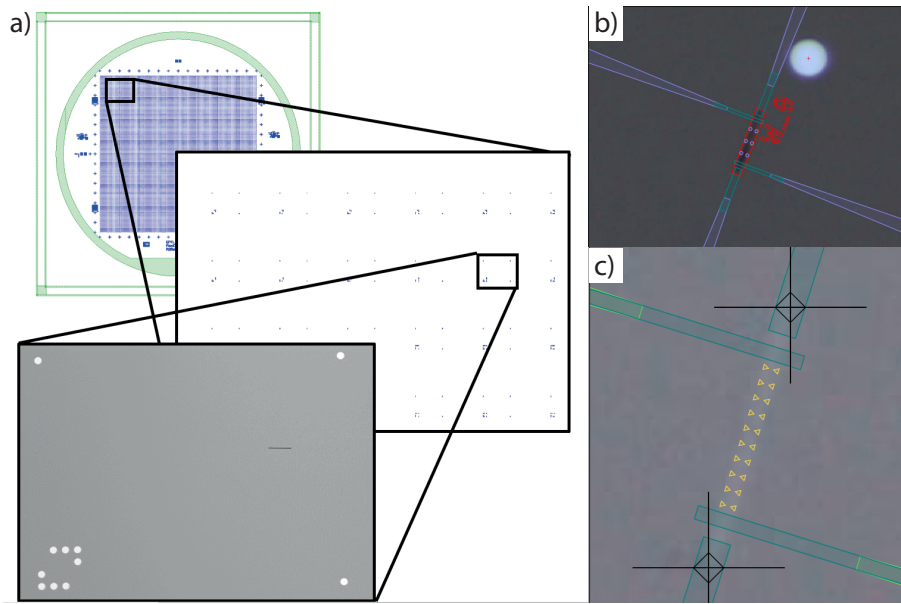


Figure 2.4: a) Pattern design. The white dots of the optical image correspond to the markers used by the e-beam for the substrate alignment and the NWs localization. b) and c) are examples of a 4 points contact design realized by our automated e-beam software. The different colors of contacts and nanoantennas represent different e-beam layers.

exposure. An additional step was introduced for e-beam on silica substrates. When the electron beam is incident on an insulating substrate, electric charges are accumulated on the surface and the incoming electrons are then deviated from their original direction leading to detrimental effects on the final pattern design. To avoid this, silica substrates are covered with MMA, PMMA and a further Cr layer of 40 *nm* thickness which provides the required electron evacuation.

The process requires various evaporation steps. For the metal pads, 10 *nm* Ti followed by around 100 *nm* Au are used. Ti is needed to improve the wetting of Au on the substrate. Specific metal layer systems are used to make ohmic contacts, as discussed in the previous paragraph, and before the deposition a fast HCl or HF etch is conducted to remove the GaAs native oxide on the NWs.

2.4 Electrical characterization

The small dimensions of the NWs demand that traditional characterization techniques to be adapted or new techniques be developed. In the following, we review the state-of-the-art characterization techniques used in this thesis, for the characterization of carrier concentration and mobility.

2.4.1 Electrical transport measurements:

One of the most common approaches for characterizing NW carrier concentration is the measurement of the conductivity with a four-point probe configuration, combined with field-effect measurements [65]. Four-point probe measurements are effective in removing the spurious effects of the contact resistance or non-linearity due to the eventual formation of Schottky contacts [57, 66, 67]. The measurements provide a conductivity value that is averaged over the separation between the contacts and across the diameter. Variations in conductivity along the NW can also be tested by addressing different segments.

The most widely used device for the characterization of NW carrier mobility is the field effect transistor (FET). In NWFETs, transistor ON-OFF behavior is achieved by applying a gate voltage that electro-statically induces free carriers in the NW channel. When carriers of the same as the original doped carriers type are introduced in the accumulation regime, there will be a measurable enhancement in electrical conductance. In the linear regime, the conductance is expressed as:

$$\frac{\partial I_{sd}}{\partial V_{sd}} = \mu \cdot \frac{C \cdot (V_{gate} - V_{(threshold)})}{L^2} \quad (2.1)$$

where μ is the majority carrier mobility, C the gate-NW capacitance, and L the gated NW length. For V_{gate} of opposite polarity, the doped carriers are repelled and the channel becomes depleted of majority carriers, reducing the electrical conductivity. A Further enhancement in the gate voltage results in the accumulation of free charge carriers with the opposite sign, i.e., inversion. The carrier mobility is determined from the NW conductance as a function of V_{gate} . It is therefore critical to know the gate NW capacitance for accurate assessment of the carrier mobility and doping level.

The extracted transconductance is used to calculate the field-effect mobility and carrier concentration in the semiconductor NWs. In literature there are different geometries for gating NW based devices, the most common configurations are the back gate [68], wrap-gate [69, 70, 71, 72] (fig. 2.5a) or top-gate [73, 74] (fig. 2.5b).

Calculations provide useful information about current transport in NWs on a relative basis. Unfortunately, the influence of the parasitic components on these measurements and calculations have shown to be extremely relevant for nanostructures. In particular, effects on the gate hysteresis [75], electrostatic screening from surface traps and the NW capacitance can deeply affect the NW transistors performances. In 2007 Khanal *et al.* numerically analyzed in 2D the effective capacitance of a NW based transistor in the bottom gate configuration [76]. In particular three effects are taken into account: (i) the gate capacitance, which depends on the properties of the device geometry, dielectric and charge distribution within the NW; (ii) the dielectric screening and doping effects on the semiconductor NW and (iii) the electric field distortion near the metal electrodes. Indeed, in small-sized devices, the source and drain contacts can screen the gate potential, which in turn leads to artifacts in the measurements. As

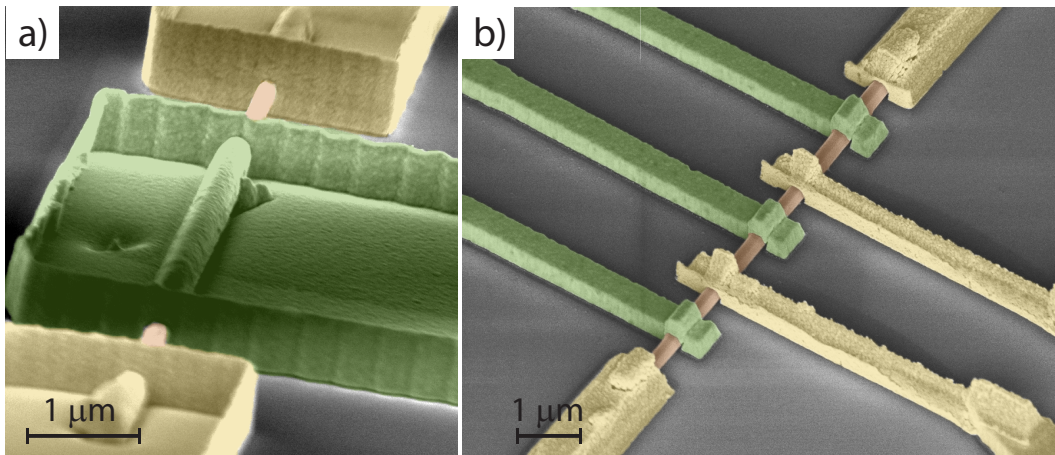


Figure 2.5: a) SEM view of a NW wrap gate transistor. b) Tilted and top-view SEM images of the NW with multiple contacts and multiple gates. In both micro-graphs electrical contacts are represented in yellow and gates in green colors.

a consequence, measured field-effect-dependent mobilities represent just an approximation to the real mobility values.

In bulk or thin film materials, Hall measurements are often used method for the determination of the carrier concentration and mobility. On the other hand, these measurements are challenging in NWs due to their one-dimensional morphology and small dimensions. In 2012, the group of Samuelson and the one of Shäpers independently performed Hall effect measurements on individual NWs [77, 78]. The Hall voltage is proportional to the carrier concentration and it enables the determination of the carrier concentration in the case of diffusive transport (high mobilities can quench the Hall effect in one-dimensional nanostructures [79]). Then, by measuring the conductivity, it is possible to determine the carrier mobility. By comparing Hall and field-effect measurements on the same NW, they found that field-effect measurements overestimate carrier densities up to a factor 4, corresponding to an underestimation of the mobility also of a factor 4.

2.4.2 Electron beam induced current (EBIC):

Electron beam induced current is a technique used to identify buried junctions or defects in semiconductors [80, 81], or to investigate minority carrier properties [82, 83, 84]. EBIC consists of an excitation by an electron beam (usually SEM is used) which generates electron-hole pairs in the semiconductor sample. Inelastic interactions of the primary electrons with the sample pushes electrons into the conduction band, thereby producing free electrons and free holes. A single primary electron can produce up to 10,000 electron-hole pairs. In semiconductor devices, at the presence of a built-in drift field, electrons and holes flow in opposite directions across. This generates an external current that can be 1000x higher than the beam current.

If the semiconductor sample contains an internal electric field, as will be present in the depletion region at a p-n junction or a Schottky junction, the electron-hole pairs will be separated by drift due to the electric field. If the p- and n-sides (or semiconductor and Schottky contact, in the case of a Schottky device) are connected through a picoammeter, a current will flow.

In this work EBIC is used to measure the minority carrier mean free path in p-type NWs. In fact, the incident electron beam leads to the formation of free electrons and holes in the NW. At the junction between NW and metal contacts holes are repulsed into the semiconductor material due to the Schottky barrier while electrons are attracted into the contact. This separation generates a current that exponentially decays in function of the distance to the Schottky barrier (Fig: 2.6). By the analysis of the current decay it is then possible to extract the minority carrier mean free path, which is an important parameter to take into account in the realization of p-n junction devices.

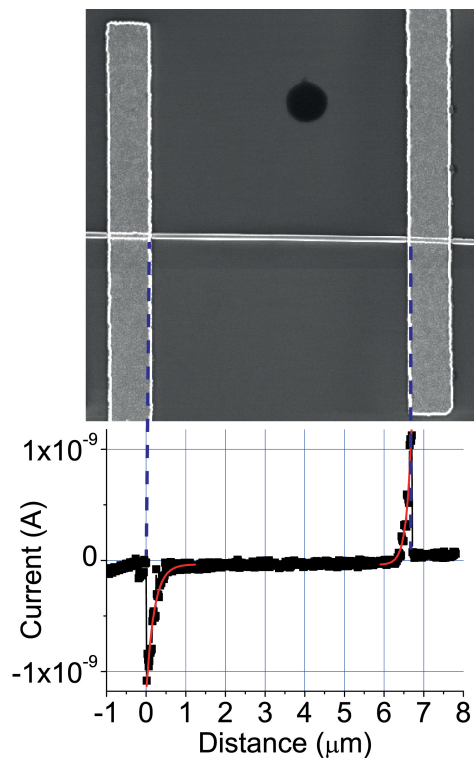


Figure 2.6: On top, SEM image of a contacted GaAs NW doped with carbon. On the bottom, electron beam induced current in function of the electron beam position on the NW.

2.5 Optical techniques

The interaction of light with objects of sub-wavelength dimensions can be described in a first approximation by Mie theory [85] based on the solution of Maxwell's equations. Due to the difference in refractive index between the medium and the object, the incident light can be scattered. This means, that energy of a beam incident on the object is removed

from the direction of propagation and redistributed in other directions. Light can also be absorbed if the object is made of a material with complex refractive index. Both scattering and absorption phenomena remove part of the intensity of the incident beam from the direction of its propagation. The difference between the intensity of light incident on the object and the intensity that continues propagating in the same direction after interacting is referred to as extinction. Knowledge on these parameters is of fundamental importance in the determination of the object optical properties.

In this thesis the following techniques are used: dark field scattering measurements, second harmonic excitation measurements (SHE) and photoconductivity measurements. Other techniques like Raman scattering, photoluminescence (PL), EDX, terahertz spectroscopy, directional Fourier microscopy and transmission electron microscopy (TEM) have been performed by collaborators on the same samples. They are not specifically discussed in this thesis.

2.5.1 Dark-field scattering:

In optical microscopy, dark-field describes an illumination technique used to enhance the contrast of the investigated samples. Rather than illuminating the sample with a filled cone of light, the condenser is designed to form a hollow cone. The light at the apex of the cone is focused at the plane of the specimen. When this light moves past the specimen plane it spreads again into a hollow cone. The objective lens sits in the dark hollow of this cone. Although the light travels around and past the objective lens, no rays enter it. When a sample is on the stage, the light at the apex of the cone is incident on it. The final image is made only by those rays scattered by the sample and captured in the objective lens. The advantage of using dark-field instead of bright-field comes in how the image of low contrast material is created: an object is seen against a dark background if it scatters light which is captured by the objective lens. In this thesis (chapter 5) dark-field scattering is used to investigate the far-field interaction between a NW and an array of disk antennas. This project is addressed to demonstrate the coupling between the semi-conducting NW and metallic nanostructures.

2.5.2 Second harmonic generation (SH-G):

Second harmonic generation (SH-G) is a nonlinear optical process, in which photons with the same frequency interacting with a nonlinear material are *combined* to generate new photons with twice the energy, and therefore twice the frequency and half the wavelength of the initial photons. Second harmonic generation, as an even-order nonlinear optical effect, is only allowed in mediums without inversion symmetry such as GaAs.

The optical response of a material is expressed in terms of induced polarization \vec{P} . In nonlinear optics, the response of the material can be described as a Taylor expansion of the material

polarization \vec{P} in powers of the electric field \vec{E} :

$$P_k = \epsilon_0 \left(\chi_{ik}^{(1)} E_i + \chi_{ijk}^{(2)} E_i E_j + \chi_{ijkl}^{(3)} E_i E_j E_l + \dots \right) \quad (2.2)$$

where χ is the susceptibility and $\chi^{(n)}$ correspond to the tensor of the n-th order nonlinear process. If we only consider the second harmonic term for a harmonic input field at frequency ω , $E_i = \epsilon_i \exp(-i\omega t) + c.c$, the resulting second order polarization is:

$$P_k^{(2)} = \chi_{ijk}^{(2)} \left(\epsilon_i \epsilon_j \exp(-i2\omega t) + \epsilon_i^* \epsilon_j^* \exp(i2\omega t) + \epsilon_i^* \epsilon_j + \epsilon_i \epsilon_j^* \right) \quad (2.3)$$

The second term of this expression shows that the non-linear polarization contains a component that radiates at twice the frequency of the input light. We should also notice that the intensity of the second harmonic signal is proportional to P^2 and therefore to E^4 . Second harmonic generation can then be used as powerful technique to investigate the localization of the electric field in GaAs NWs.

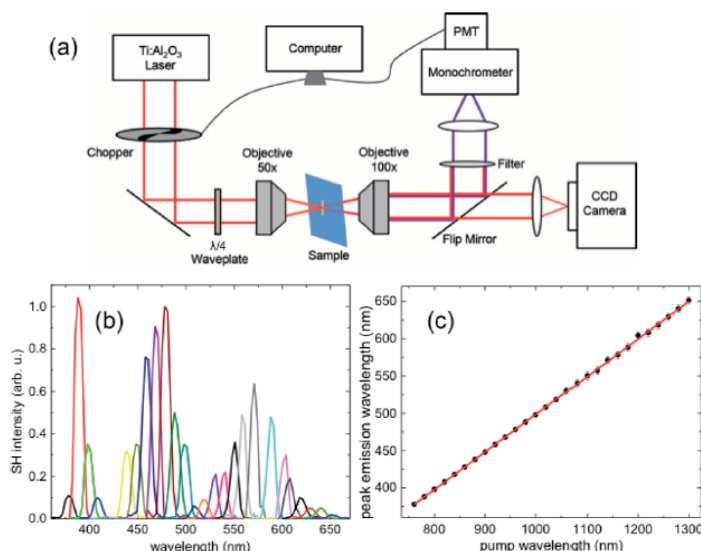
In the SH-G experiment (chapter 5), ultrafast laser pulses are generated by a tunable mode locked Ti:sapphire laser with a pulse duration of 100 *fs* and a duty cycle of 82 *MHz*. In our set-up, the beam is modulated at 67 *Hz* by a mechanical chopper with a 50% duty cycle and is steered with Ag mirrors. We use the Ti:sapphire output in the range 740 *nm* - 1040 *nm*. We further extend the investigated range down to 1300 *nm*. For this we use of a tunable optical parametric oscillator system (Spectra Physics Inspire) pumped by the Ti:sapphire laser operated at 820 *nm*. The OPO output has the same temporal width and repetition rate of the pumping laser, and we can tune it between 340 *nm* and 2200 *nm*. We uses a 700 *nm* long pass filter prior to the sample to remove any SH-G signal produced by the optical components. Additionally, the linearly polarized beam is passed through a quarter-wave plate. This create a circularly polarized beam to allow for consistent pumping conditions regardless of the NW's orientation on the substrate. The excitation beam is then focused on the nanostructure by a 50x objective (NA 0.5) to a spot size of approximately 5 μm from the backside of the sample. The SH-G is collected in transmission mode with a 100x objective (NA 0.8). It is then detected with a photon multiplier tube (PMT) and a lock-in amplifier (Oriel Merlin) after passing through a monochromatic (Cornerstone 260 1/4 m, 1200 *lines/mm*, 500 *nm* blaze). The acceptance angle is of $\pm 30^\circ$, which enables the collection of intense SH-G signal in our experimental configuration. The excitation beam is removed with a 670 *nm* short pass filter prior to the monochromator. A CCD coupled to a reflection microscope is used for alignment. A removable mirror is placed in front of the camera to direct the SH-G signal to the detector. We kept constant the time averaged excitation power at 5 *mW* for all measurements. Absolute values of the second harmonic power have been measured using a procedure discussed elsewhere [86, 87]. Figure 2.7a illustrates a schematic of the experimental setup utilized for the SH-G analysis.

The second harmonic spectra are collected for varying pumping wavelengths and are shown in Figure 2.7b in the case of one of the samples analyzed in chapter 5. In Figure 2.7c we plot for

Chapter 2. Fabrication and characterization techniques

this representative sample the peak wavelengths of the measured SH-G spectra as a function of the pump wavelength. The linear fit to these data shows a slope of 0.5, as expected for the SH-G process.

Figure 2.7: (a) Diagram of experimental setup used in second harmonic excitation spectroscopy. (b) Second harmonic emission spectra from single GaAs NW. Each color represents a different pump wavelength. (c) Peak wavelength of second harmonic emission spectra as a function of pump wavelength with a linear fit (red line, $slope = 0.5$), highlighting the second harmonic process. Copyright ©2014, American Chemical Society.



2.5.3 Photo-conductivity measurements:

Photocurrent spectroscopy is a very useful technique to measure light absorption. Photocurrent spectroscopy explores the photogeneration carriers of electrically contacted semiconductor NWs as a function of the excitation wavelength, bias voltage, and light polarization. The first investigations of photocurrents in NWs were performed at the beginning of the millennium [17, 88].

Photocurrent involves two main physical process: optical absorption and charge transport. It allows the investigation of different properties.

(i) At the metal-semiconductor interface, a space charge region occurs [89]. This has been observed for GaAs [90] and many other different NWs. Photo-conductivity related to the presence of an electric field (like in the case of Schottky junction) can be used to determine the contacts quality.

(ii) NWs can be grown with a pn-junction leading to a photo-voltaic effect when illuminated. In this case, the photocurrent at zero bias can be related to the absorption in the semiconductor. Krogstrup *et al.* demonstrated that the absorption of a single standing NW is enhanced due to its light concentrating property [16].

(iii) Persistent photo-conductivity describes a class of phenomena that occur in a very large time scale from seconds to hours. As NWs have a large surface-to-volume ratio, they are very sensitive to surface effects, such as the Fermi-level pinning. Surface band bending leads to

a spatial separation of photo-generated carriers and therefore to a reduced recombination rate [91, 92]. This sensitivity depends on the NW diameter [93] and on the ambient gas conditions [94]. Recently, GaAs/AlGaAs core-shell NWs have been investigated by photocurrent measurements as AlGaAs shell reduces the Fermi level pinning at the NW surface [95, 96, 50].

(iv) Because of the elongated geometry of NWs, their absorption depends on the polarization of the incident light. Light polarized parallel to the NW can be better absorbed than perpendicularly polarized light. This can be explained by the dielectric difference between vacuum and NW materials [97]. Photocurrent response also depends on the NW Fano resonances and plasmonic modes [98].

(v) Over the last years different hybrid structures have been introduced and investigated with regard to photovoltaic and photodetector devices. For example metal nanoparticles can be used to concentrate light or create plasmonic resonances resulting in an enhancement or modulation of the NW photo-conductivity [99]. In this thesis photo-conductivity measurements have been particularly addressed to investigate the effect of bow-tie nanoantennas on a NW [100]

3 Doping, incorporation paths and surface effects

In the path towards the development of opto-electronic devices based on NWs, two issues are central. The incorporation of electrically active dopants and the control and passivation of the NW surface.

In the first part the current state of the research field on NW doping and surface passivation is reported. We then proceed by presenting our results. GaAs NWs doped with beryllium (Be) and with carbon (C) have been investigated by the use of electrical measurements. We demonstrate that Be can diffuse into NW leading to an alternative incorporation path. Surface effects have been evaluated by comparing unpassivated with passivated NWs. We shown the influence of the surface: the pinning of the Fermi level and the consequent existence of a depletion region lead to an increase of the mobility for low doping concentrations. We also measure the minority carrier diffusion path, which can be as high as 190 nm for passivated NWs.

Publications:

A. Casadei*, P. Krogstrup*, M. Heiss, J. A. Rohr, C. Colombo, T. Ruelle, S. Uphadyay, C. B. Sorensen, J. Nygard, A. F. i Morral, *Doping incorporation paths in catalyst-free Be-doped GaAs NWs*, Appl. Phys. Lett, 102, 013117 (2013)

A. Casadei, J. Schwender, E. Russo-Averchi, D. Ruffer, M. Heiss, E. Alarcon-Llado, F. Jabeen, M. Ramezani, K. Nielsch and A. F. i Morral, *Electrical transport in C-doped GaAs NWs: surfaces effects*, Phys. Status Solidi RRL 7, 10, 890-893 (2013)

*equal contribution.

3.1 NW doping

Semiconductor NWs have gained in the recent years, the attention of researchers as both powerful building blocks for integration in nanoscale devices and playground for the study of unique physical phenomena. For this to become reality there are still some questions to be answered. Two of them concerns the controlled introduction of impurities (doping) and the surface effects.

Doping consists in the intentional incorporation of atoms with different atomic number in the crystal structure of the hosting crystal. A semiconductor material system is called intrinsic without having any dopant atoms and has negligible conductivity. The added atom will be called donor if it has higher valence electrons and it will be called acceptor if it has lower valence electrons; the semiconductor in this case is called n-type and p-type respectively. The dopant atom embedded in the semiconductor needs very small energy to donate an electron to the conduction band or a hole to the valence band. This energy, which is called ionization energy, is considerably smaller than semiconductor band gap. Adding donor or acceptor impurity atoms to a semiconductor will change the distribution of electrons and holes in the material. Since the Fermi energy is related to the distribution function, the Fermi energy will change as dopant atoms are added and will move from the middle of the band gap (if one considers the same effective mass for electrons and holes) in the case of intrinsic semiconductor toward the conduction band or valence band for n-type or p-type semiconductors respectively. Intrinsic carrier concentration is too low for having acceptable conductivity in semiconductors while by adding an extremely small amount of an impurity atom (dopant) it could increase by many orders of magnitude. So dopant concentration, which has a direct effect on carrier concentration, plays an important role on conductivity of NWs.

Overall three different strategies have been investigated for the control of doping in NWs: incorporation during growth, *ex situ* incorporation after growth through atomic diffusion [101] and ion implantation. All three techniques have led to the demonstration of both n- and p-type doping in group IV and III-V semiconductors. Each of the techniques is associated with certain advantages and disadvantages. The most successful and most used technique for doping semiconductor NWs has been the incorporation *in situ* during growth. It allows a vast control of doping concentrations, sharp doping profiles and it avoids the creation of damages which are present in case of ion implantation.

In principle, although the semiconductor planar technology is nowadays able to control dopant position and concentration with high level of precision, many questions are still open regarding the doping mechanisms in the bottom-up NWs growth. In fact NWs are most commonly obtained by the vapor-solid-liquid method (VLS) that is more complex than the standard planar technology due to the growing mechanism that takes place in non-equilibrium conditions. During the VLS growth gaseous precursor is incorporated in the solid NW form through a liquid droplet which is usually made of gold. For GaAs growth with MBE, Ga is often

used as catalyst because it offers a wider process window and guarantees that the NWs will not be contaminated by gold [35]. When VLS is used for the *in situ* doping during growth, the dopants need to be sufficiently soluble in the metal droplet for the incorporation to be successful.

In situ doping allows a relatively vast control of doping concentrations and relatively sharp doping profiles, both, in the axial as well as radial directions. Until today, silicon NWs constitute the best studied material system in terms of doping. Reproducible dopant incorporation of n and p-type dopants can be achieved up to concentrations of $1.5 \times 10^{20} \text{ cm}^{-3}$ [102]. Additionally, doping does not provoke any significant change in the number of defects and/or growth rate in silicon NWs. This means that silicon NWs can be used reproducibly as future nanoscale device components as the doping is completely controlled. Doping in arsenides and phosphides such as GaAs, InAs and InP has shown to be more challenging.

Successful doping has been achieved by adding the corresponding flux of Zn [103], Te [104], Be [58, 105, 106] and Si [57, 107, 108] (or related precursors) during the NW growth. In some cases, only a slight change in the NW morphology has been found [109, 110]. In some cases the density of carriers is lower than the density of incorporated dopants [111]. The origin of this discrepancy can be the incorporation of dopants in non-substitutional sites and/or amphotericity. For example, silicon in GaAs can be incorporated on Ga or As sites, resulting respectively in n or p-type semiconductors. Silicon added to the NW growth process leads to the main incorporation on the As sites. At silicon concentrations close to 10^{18} cm^{-3} it is observed that Si tends to form Si pairs, leading to amphotericity and to a limit in an effective doping concentration of $2 \times 10^{18} \text{ cm}^{-3}$. An electrical deactivation of more than 85% of the silicon acceptors was found for a nominal silicon concentration of $6 \times 10^{19} \text{ cm}^{-3}$. In particular, this was performed by Raman spectroscopy in transmission configuration where it was made use of modified Raman selection rules to study the interaction of plasmons with the LO phonons and to estimate the carrier density and mobility [107].

One of the main questions which still had to be completely explored at the beginning of this thesis is the incorporation path. During the *in situ* growth two ways are possible: (i) the vapor-solid (VS) mechanism, where dopants are directly deposited on the NWs sidewall or (ii) the Vapor-Liquid-Solid (VLS) mechanism where atoms first dissolve in the catalyst and then are transported across the liquid solid interface to the core of the wire (Fig.3.1a). An important insight in the mechanism, in the case of Au catalyzed Si NWs, has been reported by the group of Lauhon in 2009 [112]. Lauhon and coworkers used the atom probe tomography to make a 3-dimensional reconstruction of the NW composition. They looked at the doping distribution in Ge NWs Au catalyzed, doped by Phosphorous. As shown in Fig.3.1b, the core is substantially under-doped while the shell is over-doped. This large discrepancy between the two dopings reflects the differences in the reaction kinetics for the two incorporation paths, showing a much higher incorporation rate for the VS way than for the VLS one.

In 2010 Colombo and coworkers analyzed the doping mechanism of catalyst-free MBE Si-

doped GaAs NWs [57]. They used electrical measurements and Raman spectroscopy as complementary technique to distinguish between silicon incorporated during the axial growth and the proportion of silicon incorporated in the parasitic radial growth. They demonstrated two competing mechanisms occur: incorporation from the side facets and from the Ga droplet. They achieved p-type doping concentrations of $2.4 \times 10^{18} \text{ cm}^{-3}$ (Fig. 3.1a).

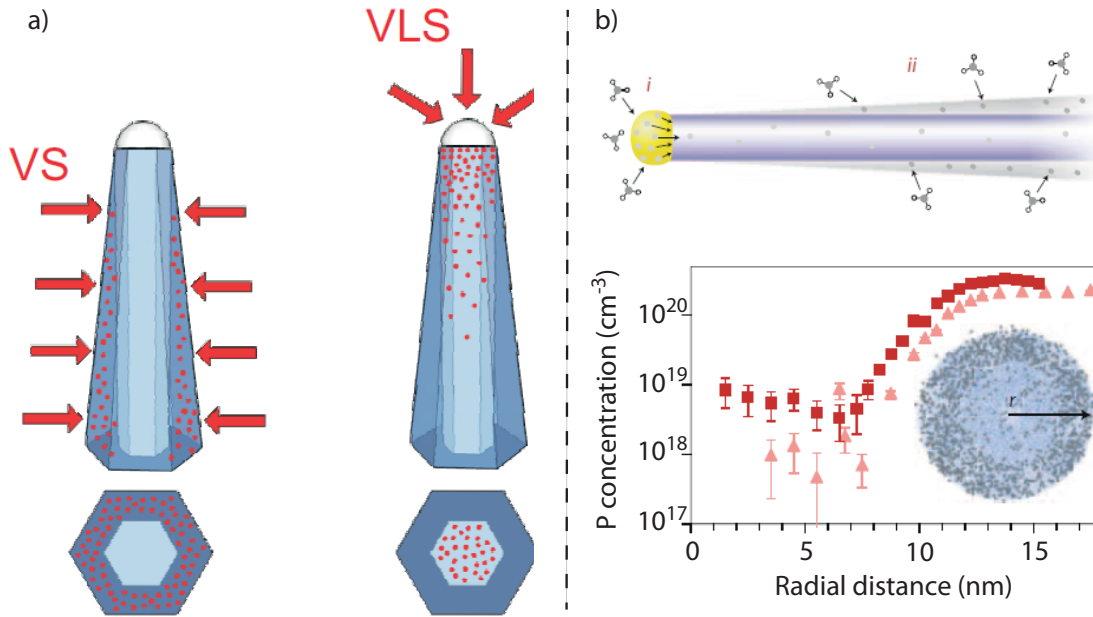


Figure 3.1: a) Sketch of the two different doping pathways for VLS grown NWs from [57]. Copyright ©(2010) American Chemical Society. b) On top, schematic representation of dopant incorporation pathways via the catalyst (*i*) and surface deposition (*ii*). On bottom, radial plot phosphorus concentration for germanium NWs. From [112]. Copyright ©(2009), Rights Managed by Nature Publishing Group.

3.2 Doping incorporation paths

In this thesis we have studied the following dopants in GaAs NWs: Si, C and Be. Figure 3.2 summarizes in a schematic manner what we have learnt in the last few years about the different incorporation paths between the three types of dopants for NWs grown by the vapor-liquid-solid mechanism. There are mainly three incorporation paths: (*i*) through the droplet leading the axial growth, (*ii*) through the side facets via parasitic or intentional radial growth and (*iii*) by diffusion from the facets into the NW core.

The incorporation of dopants through the liquid droplet depends mainly on the solubility of the dopant in the droplet and on the distribution coefficient which determines what proportion of dopant can precipitate from the liquid droplet to the solid NW [113]. Silicon is soluble in Ga, while Be and C are not. The incorporation of silicon occurs mainly on the As sites,

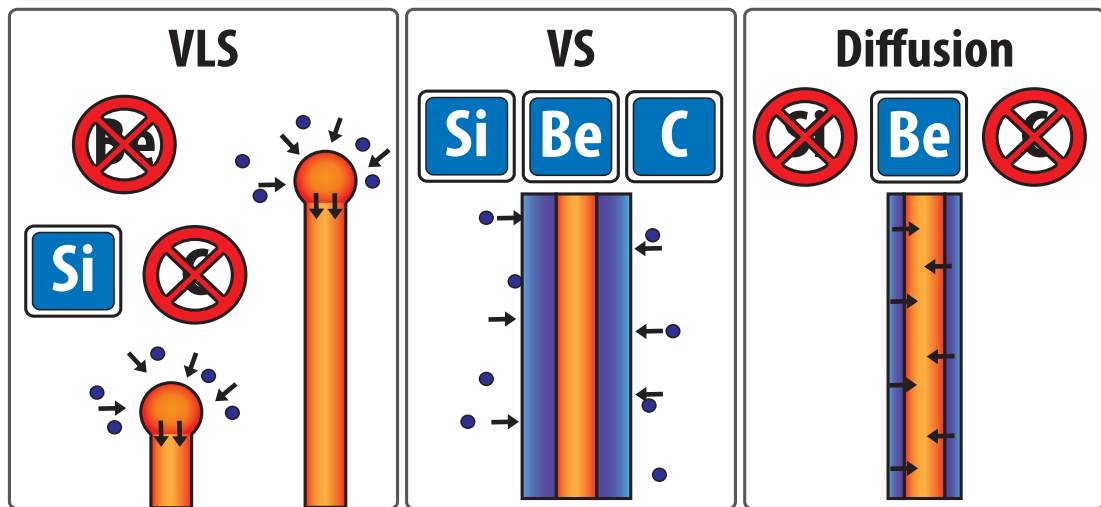


Figure 3.2: Schematic drawing of the incorporation paths for dopants in NWs grown by the vapor-liquid-solid mechanism: dopants incorporate through the liquid droplet, directly on the NW facets or by diffusion from the NW facets into the core.

similarly to what had been found in liquid-phase-epitaxy [114]. It is directly proportional to the concentration in the Ga droplet and so inversely proportional to the growth rate of the NW. At high silicon concentrations, the electric field of the Si ions drives the formation of silicon pairs. Therefore, silicon is not the most optimal dopant for highly doped p-type NWs.

As silicon, carbon and beryllium are incorporated in thin GaAs films grown on $\langle 110 \rangle$ surfaces, they can also be incorporated during the radial growth of the NWs. Radial growth can be engineered after stopping the axial growth or can be parasitic to the axial growth. As it is the case for $\langle 110 \rangle$ surfaces, Si doping of the GaAs shells can lead to both p- and n-type doping.

It is generally accepted that incorporation paths of dopants are similar from the growth precursors and result either from the radial growth of the NW or through diffusion through the catalyst [115, 116, 112, 117, 105]. Still, one may consider a third path, which consists on the diffusion of dopants in the core and/or from the shell to the NW core. The relevance of this path should depend on the diffusion coefficient of the dopant and the growth temperatures used [118]. Typical dopants with a high diffusion coefficient in III-Vs are Be and Te [119, 120]. Silicon and carbon have an extremely low diffusion coefficient in GaAs at the growth temperatures typically used for GaAs NWs ($\approx 630^\circ\text{C}$). As a consequence, diffusion does not play a role in their incorporation. On the contrary, beryllium exhibits a relatively high diffusion coefficient around 600°C . Beryllium incorporates on the facets of the NWs during growth via the parasitic radial growth. Thanks to the high diffusion coefficient, Be distributes in a homogeneous manner along the whole NW axis. After growth, the conductivity is homogeneous along the whole NW length. Concentrations between 6×10^{17} and $5 \times 10^{19} \text{ cm}^{-3}$ have been obtained.

3.3 Surface states and passivation

3.3.1 Fermi Level pinning at the surface

Due to the abrupt discontinuity of the crystal lattice at semiconductor surfaces, a large number of localized energy states can be introduced to the surface region [121]. These surface states play an extremely important role in the opto-electronic properties of GaAs NWs. In ambient conditions there is a formation of a thin oxide layer on the NW surface resulting in a pinning of the Fermi level. Landgren *et al.* have experimentally determined the surface Fermi level of oxidized (110) GaAs. They obtained values of 0.5 eV above the valence band for p-type material and 0.6 eV below the conduction band for n-type GaAs respectively [122]. The existence of this region reduces the electrically active part of the NWs [123, 124] and its width depends on the GaAs doping level. The depletion region (W) position is represented in fig. 3.3a. With increased doping the electric field is screened more efficiently, therefore reducing the depletion region. We can avoid this problem by passivating the GaAs with a wider band gap semiconductor, such as AlGaAs [125, 126].

In a semi-classical model the band bending is obtained by the difference φ of the Fermi level at surface states with respect to the Fermi level of the bulk. The Poisson equation in cylindrical coordinates, can be used to describe the variation of φ in the NW geometry:

$$\frac{1}{r} \frac{\partial}{\partial r} r \frac{\partial \varphi(r)}{\partial r} = - \frac{eN_A}{\epsilon\epsilon_0} \quad (3.1)$$

The equation is solved by using the boundary conditions of a vanishing electric field at the surface: $\varphi(r_0) = \Phi$, where Φ corresponds to the pinning position of the Fermi level. For high doping concentrations, the difference in the Fermi level and the valence (conduction) band is negligible compared to the surface potential which is found to be 0.5V in p-type GaAs [122]. The result is an implicit equation for the NW depletion layer width w which depends on the NW radius r_0 and the doping concentration N_{shell} [123]:

$$-\frac{w^2}{2} + r_0 w - (r_0 - w)^2 \ln\left(\frac{r_0}{r_0 - w}\right) = \frac{2\epsilon\epsilon_0\Phi}{eN_{shell}} \quad (3.2)$$

The values of the depletion region w as a function of the doping concentration and for two different NW radii is shown in Figure 3.3b. For high doping concentrations, the depletion region can be as small as few nm. It increases rapidly for lower doping concentrations. Already in the case of doping concentration close to $10^{18} \text{ atoms/cm}^3$, the depleted region corresponds to several tens nm. For example, a NW with $r_0 = 40 \text{ nm}$ would be completely depleted and therefore insulating for carrier concentrations below $1 \times 10^{18} \text{ atoms/cm}^3$.

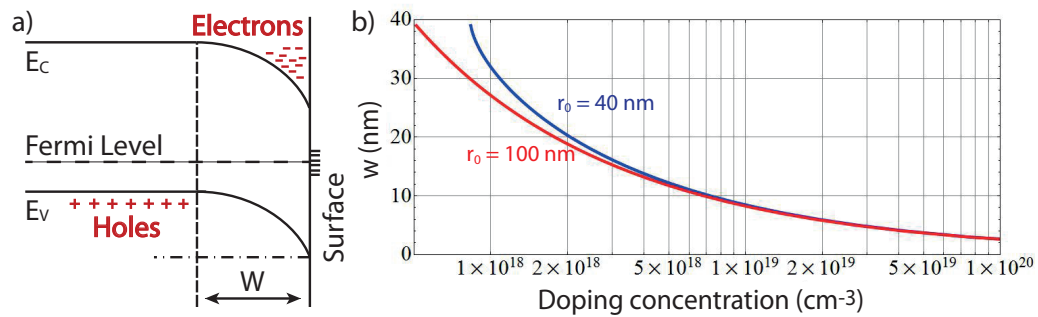


Figure 3.3: a) Schematic band alignment of p-doped GaAs material at the interface with air. b) Calculated depletion region width in dependence of NW concentration for radii $r_0 = 40 \text{ nm}$ and $r_0 = 100 \text{ nm}$. Rights managed by AIP Publishing LLC.

3.3.2 Surface passivation with AlGaAs

So far there are several well established techniques for GaAs passivation based planar devices involving treating the surface with sulfur (S) or antimony (Sb). Still, the most used method is epitaxial growth of a protective layer of higher band gap material [127]. AlGaAs has a higher band gap than the GaAs and completely encloses the GaAs and furthermore both materials are lattice matched enabling formation of perfect interface. This is important since it significantly reduces the interface recombination rate. It is also important to additionally protect the AlGaAs with a GaAs layer. AlGaAs rapidly oxidizes in air. Oxygen acts as a deep level trap, reducing the carriers recombination life time and the quantum efficiency.

The NWs electronic properties such as carrier lifetimes and mobility are extremely dependent on the surface and interface states due to the NW high surface-to-volume ratio. Research on planar structures has shown that the GaAs surface recombination can be dramatically reduced by replacing the free GaAs surface with a GaAs/AlGaAs hetero-interface. Both the growth techniques [128, 20] and the NW crystal structure [129] are reported to influence carrier lifetimes in GaAs/AlGaAs core-shell NWs. Despite several works have been devoted to optically characterize the surface effects in NWs, demonstrating that AlGaAs capping reduces the recombination centers [130, 129, 20, 96, 131], electrical measurements remain challenges. In 2012 Chang *et al.* combined time resolved photoluminescence measurements (PL) and EBIC measurements on GaAs single core and GaAs/AlGaAs core-shell NWs. They observed a 48-fold enhancement in the PL intensity and a 6-fold increase in the minority carrier diffusion length with surface passivation. The surface recombination velocity was calculated to lie in the range from $1.7 \cdot 10^3$ to $1.1 \cdot 10^4 \text{ cm/s}$. For the passivated NWs, they estimated the minority carrier mobility to lie in the range from 10.3 to $67.5 \text{ cm}^2/(V \cdot s)$, based on the measured lifetimes and diffusion length at room temperature. They also claimed that the relatively long minority carrier diffusion lengths indicate that twin stacking faults do not limit the minority carrier lifetimes in passivated NWs [50]. These results represented a further proof that surface passivation is advantageous. In this chapter some of these results are confirmed on C-doped

GaAs NWs and a more deep investigation of the doping and passivation effects on the electrical mobility is performed with electrical measurements on NW based transistors.

3.4 Be-doped NWs: new incorporation path

In this section, we show our results concerning the doping of GaAs NWs with Be. By measuring the spatial dependence of the conductivity of NWs deposited with a flow of Be under different conditions we identify the incorporation paths and discuss the advantages and limitations of this dopant. In principle, this work can be extrapolated to other III-V materials.

3.4.1 Device fabrication

The NWs were grown on (111) Si using a self-catalyzed (VLS) method [35, 39, 38]. Ga deposition rate corresponds to a nominal growth of 0.27 \AA/s , for times ranging between 30 and 60 minutes (table 3.1), at 630°C substrate temperature and a V/III flux ratio of 60[132]. The vertical growth rate for all the NWs was around $15 \mu\text{m/h}$. P-doping was achieved by adding a flux of beryllium either during growth of the core or *a posteriori* during the growth of a shell. The shell was obtained at a lower temperature (465°C), switching the As source from As_4 to As_2 and increasing the V/III ratio to 150 [99]. Six different types of growths with varying doping profiles were carried out to give some insight into the Be incorporation mechanisms during axial VLS and radial VS growth of self-catalyzed GaAs NWs (table 3.1).

Sample	Growth time [min]	Nominal shell [nm]	Nominal conc. [atoms/cm^3]	Conductivity $(\Omega \times m)^{-1}$
1	30	0	5×10^{18}	0.06 ± 0.03
2	60	0	2.5×10^{19}	16000 ± 5000
3	45	30	1×10^{18}	3 ± 2
4	45	30	5×10^{18}	50 ± 20
5	30	10	1.5×10^{19}	1000 ± 600
6	30	30	1.5×10^{19}	2200 ± 500

Table 3.1: Time of axial NWs growth, nominal shell thickness, nominal doping concentration (corresponding to the planar growth under the same conditions) and measured conductivity obtained by 4-point contact configuration.

3.4.2 Measurements and discussion

The effective resistance in the NWs was measured by carrying out 4-point electrical measurements at room temperature [57] on around 50 samples. The high number of devices were obtained within a reasonable time frame with our auto-contacting software. The electrical contacts consisted of Pd/Ti/Au (40/10/250 nm) and the samples were annealed at 300°C for 20 minutes in order to ensure ohmic and reproducible contacts.

3.4. Be-doped NWs: new incorporation path

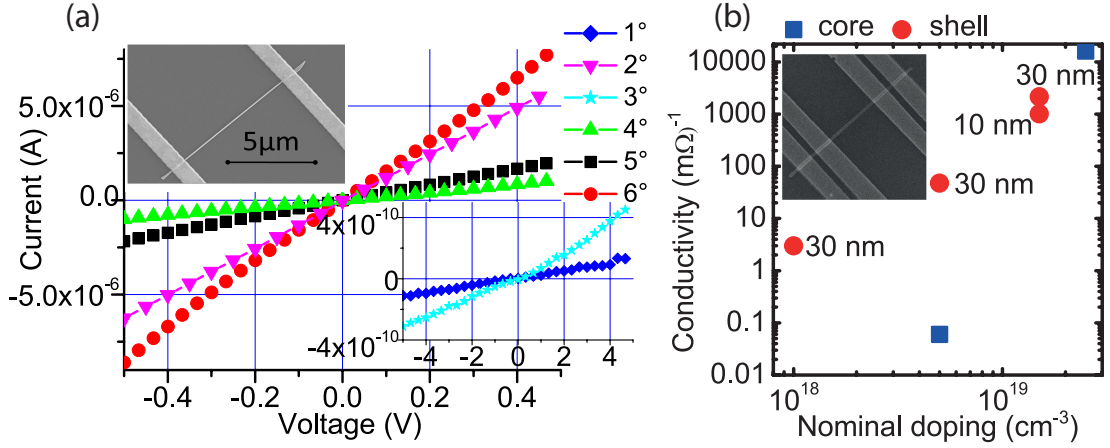


Figure 3.4: (a) I-V examples of each growth performed with single 2 contact configuration. The linearity of the curve shows that Pd/Ti/Au electrical contacts are ohmic on Be doped GaAs NWs. In the insert a SEM image of a contacted NW. (b) NWs conductivity obtained from 4 point measurements and a corresponding SEM image. *Rights managed by AIP Publishing LLC.*

Figure 3.4a shows a typical contacted NW for single 2 point contact configuration. Multiple contacts were also realized to understand the spatial dependence of the conductivity along the NW axis. Figure 3.4a shows examples of 2-point current-voltage. The linearity of the curves indicates that all contacts are ohmic, even for the highly resistive samples. The conductivity of the NWs obtained from 4-point probe measurements can be found in table 3.1 and in Fig. 3.4b.

Two observations induced us to conclude that Be is not incorporated through the NW droplet during the vertical growth. First, we did not find any clear dependence of the conductivity with the NW diameter within a given type of growth. Second, the apparent conductivity obtained in the NWs grown with a nominally doped core and without a shell (sample 1) is much lower as compared to the nominal doping concentration. Sample 4 has been grown with the same core conditions as Sample 1 with an additional shell of 30 nm with the same Be flux. By comparing the two samples we can separate the transport contribution due to the VLS and the VS growth. The doping contribution from the VLS step is negligible indicating that the flux of Be atoms to liquid-solid growth front is relatively small [59, 133]. We therefore deduce that the incorporation path of Be through the droplet can be neglected.

The average carrier concentration in GaAs at room temperature can be obtained from the relation $p = N_A$, where N_A is the doping density. We then obtain:

$$N_A = \frac{\sigma}{\mu \times e} \quad (3.3)$$

where e is the electrical charge of the electrons, μ is the mobility in the NWs and σ is the conductivity. We assume $\mu = 31 \text{ cm}^2/(V \times s)$, as recently measured in similar NWs and doping

Chapter 3. Doping, incorporation paths and surface effects

concentration range [134]. From the electrical measurements, we obtain the current crossing the NW. In order to extract the doping concentration we taken into account the following effects: (i) non-uniform radial doping distribution, (ii) surface effects such as depletion and dopant deactivation and (iii) diffusion of dopants during the growth. Our model considers these three effects.

We present the effect of surface band bending, especially important for small diameters and/or low doping concentrations. The Fermi level pinning due to the surface traps was discussed previously in this chapter. The equation used to calculate the depletion region (w) in function of the doping concentration (N_{shell}) and the radius (r_0) of the NWs is here reported:

$$-\frac{w^2}{2} + r_0 w - (r_0 - w)^2 \ln\left(\frac{r_0}{r_0 - w}\right) = \frac{2\epsilon\epsilon_0\Phi}{eN_{shell}} \quad (3.4)$$

The actual doping profile in the NW depends on the Be diffusion during growth [118, 135]. In fact, during axial growth there is a concentration of Be adatoms on the NW sidewalls which can be incorporated [35, 57]. The concentration of Be in the vicinity of the NW surface is considered constant due to the constant incident Be flux, which leads to a quasi steady state concentration at the surface during growth, p_0 . Diffusion of Be from the surface to the NW core is driven by the gradient in Be concentration and by the high temperature in the chamber. It is sufficient to solve the one-dimensional diffusion equation, which gives [136]:

$$p(x, t) = p_0 \times \text{erfc}\left(\frac{x}{2 \times (Dt)^{1/2}}\right) \quad (3.5)$$

where p_0 is the doping concentration at the interface, x is the distance from the interface, t is the diffusion time and D is the diffusion coefficient

$$D = D_0 \times e^{-E_0/kT} \quad (3.6)$$

where for Be diffusion in GaAs, $D_0 = 0.655 \text{ cm}^2/\text{s}$ and $E_0 = 2.43 \text{ eV}$ [136]. The diffusion length is defined as the distance with which the concentration is $1/e$ of the initial concentration (Table 3.2). As schematically drawn in Fig. 3.5, the existence of a depletion region and the diffusion of Be strongly modify the range of electrically active part of the NWs.

The 4-point measurements are performed in the center of the NW. it is therefore assumed that the diffusion at that point corresponds to half of the full VLS growth time. If we now consider the doping diffusion and the carrier depletion region at the surface we can deduce the doping concentration and electrical carrier concentration:

$$\begin{cases} \int_0^{r_0} \int_0^{2\pi} p(x, t) x \sin(\theta) dx d\theta = \frac{L}{\mu R e} \\ -\frac{w^2}{2} + r w - (r - w)^2 \ln\left(\frac{r}{r-w}\right) - \frac{2\epsilon\epsilon_0\Phi}{eN_{shell}} = 0 \end{cases} \quad (3.7)$$

where R/L is the resistance per unit length, N_{shell} is the shell concentration and the doping

3.4. Be-doped NWs: new incorporation path

Sample	Carrier conc. cm^{-3}	Shell conc. [$atoms/cm^3$]	Total shell [nm]	w [nm]	(1/e) Diff. [nm]
1	$(1 \pm 0.5) \times 10^{15}$	$(1.2 \pm 0.6) \times 10^{18}$	4	27	38
2	$(3 \pm 1) \times 10^{19}$	$(5 \pm 1) \times 10^{19}$	8	3.5	53
3	$(5 \pm 3) \times 10^{15}$	$(5 \pm 1) \times 10^{17}$	36	50	46
4	$(1 \pm 0.5) \times 10^{17}$	$(6 \pm 3) \times 10^{17}$	36	39	46
5	$(3 \pm 2) \times 10^{18}$	$(5 \pm 3) \times 10^{18}$	14	12	38
6	$(4 \pm 1) \times 10^{18}$	$(7 \pm 2) \times 10^{18}$	34	10	38

Table 3.2: Carrier concentration, shell doping concentration calculated with the model described previously, total expected shell, depletion region (w) and diffusion length defined by the distance which the concentration is 1/e of the shell concentration.

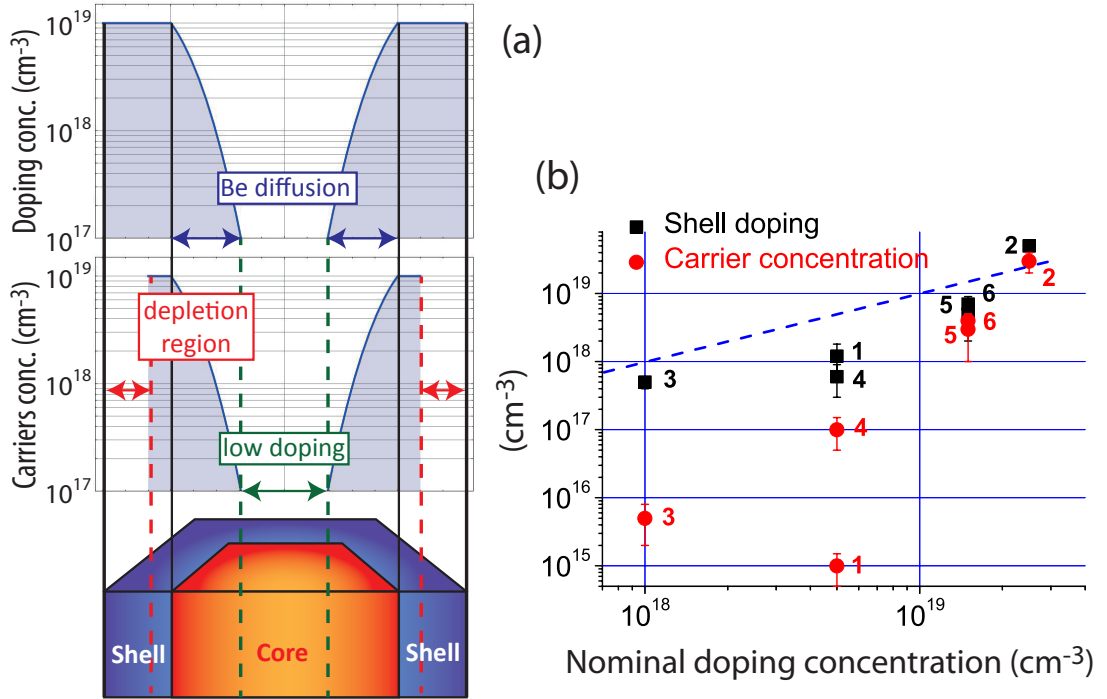


Figure 3.5: (a) Section view of a NW. The doping and the carrier concentration are reported as a function of position along the NW diameter. (b) Comparison between carrier density concentration (red) and calculated doping concentration in the shell (black). The blue dotted line represents $N_a = N_{shell}$. The error bar reported for every dots represent only the standard deviation calculated on the electrical measurements. *Rights managed by AIP Publishing LLC.*

distribution ($p(x, t)$) is:

$$p(x, t) = \begin{cases} N_{shell} \times \text{erfc} \left[\frac{x}{2 \times (Dt)^{1/2}} \right] & \text{core} \\ N_{shell} & \text{active part of shell} \\ 0 & \text{depletion region} \end{cases} \quad (3.8)$$

For low doping concentrations (below $5 \times 10^{18} \text{ cm}^{-3}$) the depletion region is larger than the shell thickness. This concerns sample 1, 3 and 4. These three samples exhibit a very low conductivity. By taking into account the depletion region at the surface, we can extract the doping concentration at the shell. This is very close to the nominal doping concentration. For higher doping concentrations, the depletion region it is only few nm and it affects much less the overall conductivity. It is interesting to note that even though the incorporation of Be via VLS mechanism is negligible, it is possible to dope the NWs almost homogeneously if we keep the growth temperature at very high values and for enough time. Indeed, for nominal doping concentration higher than 10^{19} cm^{-3} the highly doped shell and the long growth time results into a strong diffusion of Be inside the core, leading to an almost fully doped NW [137]. This is extremely advantageous for example in the case where an ohmic contact with a substrate is relevant (e.g. solar cells).

3.5 C-doped NWs: surface passivation effects

3.5.1 Device fabrication

The NWs consist of an undoped GaAs core of about 70 nm in diameter and a C-doped shell. GaAs NWs are grown on a (111) Si substrate under conditions that maximize the yield of vertical NWs [132, 39]. We set the MBE parameters in order to have a rotation of 7 rpm , a flux of Ga equivalent to a planar growth rate of 0.3 \AA/s , a substrate temperature of $640 \text{ }^\circ\text{C}$ and a V/III beam equivalent pressure (BEP) ratio of 50. After the vertical growth, the growth conditions were radically changed for obtaining a 40 nm GaAs doped shell. The substrate temperature was lowered to $465 \text{ }^\circ\text{C}$ and the Ga flux was stopped for about 10 min while the V/III BEP ratio was increased to 130[55]. A p-type doping was achieved by adding a flux of Carbon during the growth of the shell. We grew a series of samples with different C flux given by the current applied to the cell, as reported in table 1. To test the effect of the surface, equivalent samples have been fabricated with the addition of a capping layer consisting of 15 nm $\text{Al}_{0.3}\text{Ga}_{0.7}\text{As}$ and 6 nm of intrinsic GaAs. The geometrical cross section of unpassivated and passivated NWs are shown in fig. 3.6. The SEM picture represents a forest of vertical GaAs C-doped NWs.

Multiple four point measurements have been performed on around 100 samples to give an accurate estimation of the resistivity of the NWs. Thanks to our auto-contacting software[138], the realization of a large number of devices has been automatized. The electrical contacts consists of Pd/Ti/Au (40/10/250 nm) metal layer directly in contact with the doped shell. For the capped NWs, the $\text{Al}_{0.3}\text{Ga}_{0.7}\text{As}$ shell was etched away using a solution of citric acid and hydrogen peroxide (2:1) leading to an etching rate of 1.4 nm/s . In order to extract the NW majority carrier mobility, we realized bottom gate transistors, with 200 nm thick SiO_2 layer used as a gate dielectric.

3.5. C-doped NWs: surface passivation effects

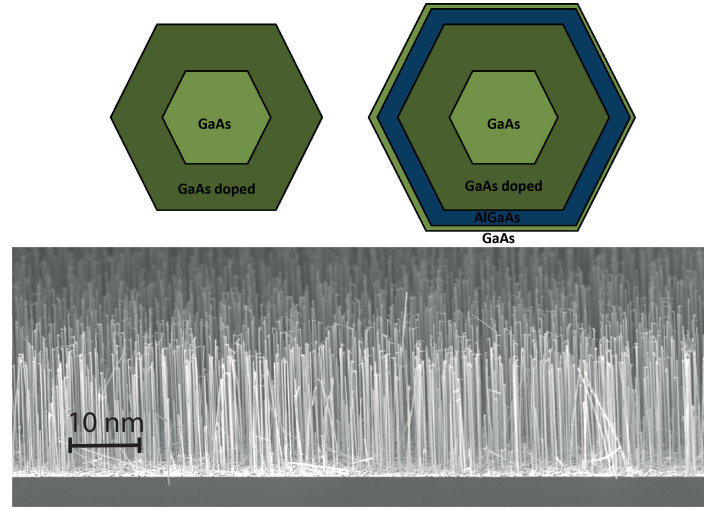


Figure 3.6: On top, Geometrical cross section of unpassivated and passivated NWs. Below, SEM image of a forest of vertical GaAs C-doped NWs.

3.5.2 Hole mobility in function of doping and surface

As previously discussed, in ambient conditions there is a formation of a thin oxide layer on the NW surface resulting in a pinning of the Fermi level. In GaAs the pinning occurs near the middle of the band gap, producing a depletion region. The existence of this region reduces the electrically active part of the NWs[123]. A solution to avoid this problem is to passivate the GaAs with a wider band gap semiconductor, such as AlGaAs[125, 126]. In this study we show how a passivation layer affects the electronic properties of GaAs NWs with different doping concentrations.

Seven types of samples have been analyzed. The shell doping concentration, the resistance and the mobility are reported in table 3.3.

Sample	Doping conc. [cm^{-3}]	Res/Length [$\text{k}\Omega/\mu\text{m}$]	Mobility [$\text{cm}^2/(\text{V}\cdot\text{s})$]
1p	8×10^{18}	91	8
2p	5×10^{18}	53	12
3p	2.5×10^{18}	103	14
4p	1×10^{18}	2700	20
1u	4×10^{18}	329	8
2u	2×10^{18}	300	20
3u	1.3×10^{18}	528	30

Table 3.3: Doping shell concentration, resistance per unit length and mobility of the NWs analyzed. "p" corresponds to the passivated NWs and "u" to the unpassivated ones.

Chapter 3. Doping, incorporation paths and surface effects

We obtained the conductivity σ from 4 point measurements and the mobility μ is derived from bottom gate field effect transistor characteristics:

$$\mu = -\frac{\partial I}{\partial V_g} \frac{L^2}{C \times V_{sd}} \quad (3.9)$$

where V_g and V_{sd} are respectively the gate and the source-drain voltages, L is the distance between source and drain and C is the device capacitance. For this structure, formed by a NW gated through a SiO_2 substrate, it is found [76] :

$$C = 2\pi\epsilon_0\epsilon_r \frac{L}{x \times \cosh^{-1}((r_0 + h)/r_0)} \quad (3.10)$$

where $\epsilon_0\epsilon_r$ is the dielectric constant of insulating layer, r_0 is the NW radius and h the dielectric thickness. For passivated NWs we consider the capping layer as a capacitance in series with the bottom gate dielectric. For 200 nm SiO_2 thickness with $\epsilon_r = 3.9$ the typical capacitance value of our devices is around 1 fF. From the output curves (Fig. 3.7a) we also observe that carbon acts as p dopant [139].

We assume that all acceptors are ionized at room temperature. This means that the holes concentration can be directly linked to the C concentration. In the case of passivated NWs (1p, 2p, 3p and 4p) we can consider that the electrically active part corresponds to the entire doped shell because there is no depletion region. We can therefore measure the conductivity of the doped shell σ_{shell} calculated on the doped cross section area and directly extract the doping density

$$N_{A(passivated)} = \frac{\sigma_{shell}}{\mu \times e} \quad (3.11)$$

When NWs are not passivated, one needs to consider the Fermi level pinning at the NW surface that generates a depletion layer. Solving the Poisson equation and using the boundary conditions of a vanishing electric field at the surface we can calculate the depletion region width. For the doping concentration analyzed, we use a surface potential Φ at the GaAs surface of 0.5 eV[122]. The depletion region w follows[58]:

$$-\frac{w^2}{2} + r_0 w - (r_0 - w)^2 \ln\left(\frac{r_0}{r_0 - w}\right) = \frac{2\epsilon_r\epsilon_0\Phi}{eN_{shell}} \quad (3.12)$$

where $\epsilon_r = \epsilon_{GaAs} = 12.9$ is the GaAs dielectric constant and N_{shell} the doping concentration in the shell. N_{shell} and w can be deduced from the electrical measurements using the following system:

$$\begin{cases} \int_{r_{core}}^{r_0-w} \int_0^{2\pi} N_{shell} x \sin(\theta) dx d\theta = \frac{L}{\mu R e} \\ -\frac{w^2}{2} + r_0 w - (r_0 - w)^2 \ln\left(\frac{r_0}{r_0 - w}\right) - \frac{2\epsilon_r\epsilon_0\Phi}{eN_{shell}} = 0 \end{cases} \quad (3.13)$$

where R/L is the resistance per unit length, μ is the carrier mobility and r_{core} is the radius of

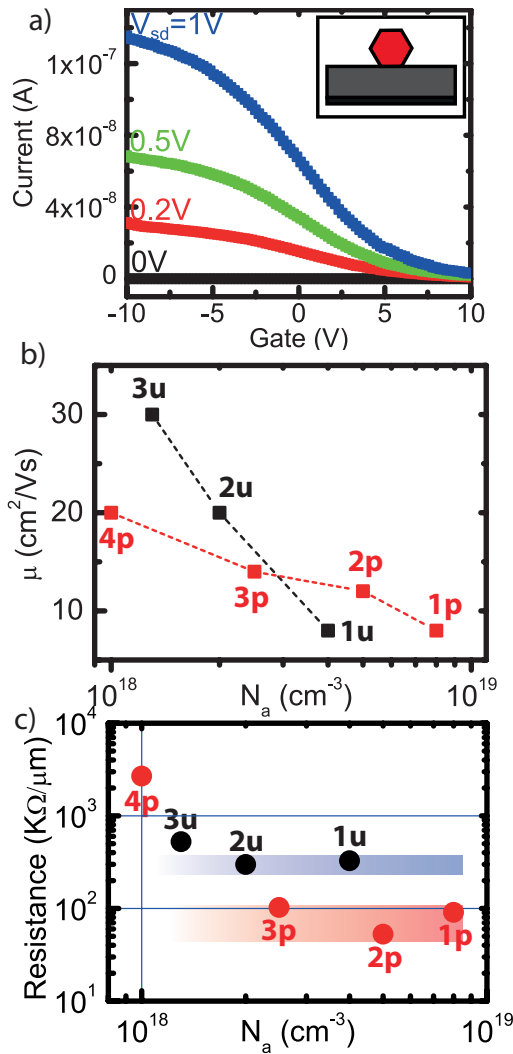


Figure 3.7: a) Example of a transistor output curve for different source-drain voltages V_{sd} . The inset shows the NW bottom-gate transistor configuration. b) Mobility vs shell doping concentration for the 7 types of NWs analyzed. 1u, 2u and 3u are unpassivated NWs while 1p, 2p, 3p and 4p are passivated. c) NW resistance per length in function of the doping concentration. The black and red stripes highlight the region of minimum resistance per length for unpassivated and passivated NWs. Copyright ©2013 WILEY-VCH Verlag GmbH & Co. KGaA, Weinheim.

the undoped NW core.

The results of the mobility and the resistance obtained for all different types of NWs are shown in Fig 3.7b and 3.7c. The mobility measured increases for decreasing doping concentration, for both passivated and unpassivated NWs. This behavior is commonly observed in semiconductors and is related to a decrease of ionized impurity scattering related to the doping atoms. Interestingly, we observe a saturation of the resistivity for doping concentrations higher than $2 \times 10^{18} \text{ cm}^{-3}$. The saturation values correspond to $\approx 80 \text{ k}\Omega/\mu\text{m}$ and $\approx 330 \text{ k}\Omega/\mu\text{m}$ respectively for the passivated and unpassivated NWs.

A priori we would expect a higher mobility for passivated NWs with respect to the unpassivated. Surprisingly, in Fig. 3.7b, we observe that this is only true for the doping concentrations higher than $3 \times 10^{18} \text{ cm}^{-3}$. In order to shed some light to this issue, we have simulated the band profile across the NW with *nextnano*³ software (copyright (c) 2012, nextnano GmbH, Germany). We

calculated the majority carrier (holes) distribution inside the NWs. Figure 3.8 shows the profile of the holes concentration for both passivated and unpassivated NWs. There are two doping concentrations (ρ : on the left $\rho = 4 \times 10^{18} \text{ cm}^{-3}$ and on the right $\rho = 1 \times 10^{18} \text{ cm}^{-3}$ (Fig. 3.8). In the unpassivated case the Fermi level pinning was used.

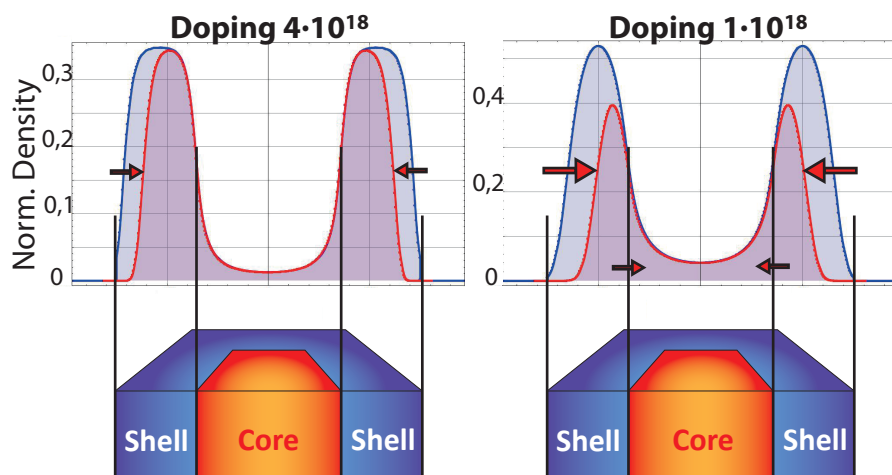


Figure 3.8: Transverse section view of 2 NWs with intrinsic core and a doped shell (4×10^{18} and $1 \times 10^{18} \text{ cm}^{-3}$). The distribution holes profile is represented in the case of NWs capped (blue lines) and NWs uncapped (red lines). In the unpassivated NWs, the depletion region has the effect of keeping the holes far from the surface. The numerical analysis has been performed with *nextnano*. Copyright ©2013 WILEY-VCH Verlag GmbH & Co. KGaA, Weinheim.

Holes are mainly distributed in the doped shell, but a small portion is also found in the core (Fig. 3.8). In the unpassivated wires, the surface depletion leads to a decrease in the amount of carriers in the shell. This is especially relevant for low doping concentration. From this we conclude that two mechanisms may contribute to the observation that unpassivated NWs have higher mobility. First, the depletion region ensures that transport of carriers occurs at a certain distance from the surface reducing the surface-related scattering. Second, a higher proportion of the transport occurs through the undoped core, which exhibits highest mobility due to the absence of dopants. The resulting mobility in unpassivated and low doped NWs is therefore higher than the respective passivated NWs.

3.5.3 Minority carrier mean free path

In this last part of the chapter we investigate the mean free path of minority carriers (electrons) using electron beam induced current (EBIC). At the semiconductor-metal interface a Schottky barrier is produced. When exciting electron-hole pairs with light or an electron beam, the potential gradient produced by the Schottky barrier attracts minority carriers (electrons) into the contacts. This leads to a current that is measured with a picoammeter. This current

exponentially decays with the distance from the contact [116]:

$$I = I_0 e^{x/l} + c \quad (3.14)$$

where l is the electron mean free path. In order to understand the electron beam interaction volume, we simulate the trajectory of electrons in the NW with Casino [140], shown in (Fig. 3.9a). We calculate the trajectories of 200 incident electrons with an energy of 3 keV and a probe current of 200 pA , corresponding to the experimental conditions used. As it can be seen in Fig. 3.9a, the excitation is limited to the doped shell of the NW.

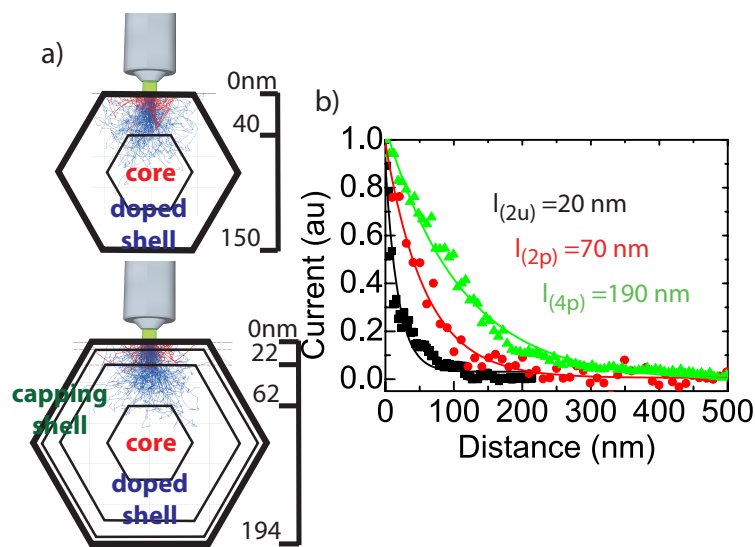


Figure 3.9: a) Electron trajectory in the NWs simulated by Monte Carlo. The simulations are performed for 200 electrons with energy of 3 keV and a probe current of 300 pA . b) Experimental current decay as a function of distance to the contact for 3 NWs samples (2u, 2p and 4p). The minority carrier mean free path extracted increase up to 190 nm for passivated NWs with a doping concentration of 10^{18} cm^{-3} . Copyright ©2013 WILEY-VCH Verlag GmbH & Co. KGaA, Weinheim.

Figure 3.9b shows the exponential decay of the current for an unpassivated and two passivated NWs. For the unpassivated NW, we obtain the lowest mean free path: 20 nm . The passivated NWs exhibit longer electron mean free paths, up to 190 nm . Despite the majority carrier (holes) mobility is lower for passivated NWs, a longer diffusion path is found for the minority carriers (electrons). This is explained by surface oxidation generating the Fermi level pinning. Indeed holes are repulsed from the surface, but electrons are attracted. Consequently, the electron main free path in unpassivated NWs is reduced due to the large defect and trap densities at the surface.

3.6 Conclusions

In conclusion, we have discussed the doping incorporation paths and the surface effects in semiconductor NWs. We have shown that GaAs NWs can be doped with Si, Be and C according to the following restrictions: *(i)* only Si is incorporated through the droplet, *(ii)* Be can diffuse from the NW shell to the core and *(iii)* all Be, Si and C can be incorporated during the VS growth. We presented the results obtained with electrical measurements on Be doped GaAs NWs, demonstrating that Be atoms are mostly incorporated from the side facets and that the incorporation through the Ga droplet is negligible. The doping concentration can be tuned between 6×10^{17} and $5 \times 10^{19} \text{ cm}^{-3}$.

We have measured the carrier concentration, mobility and minority diffusion length for core-shell GaAs NWs where the shell is C-doped at different concentrations. The effect of surface states is evaluated by comparing the values for passivated and unpassivated NWs. At low doping concentrations, the highest mobility is observed for unpassivated nanowires showing a mobility of $30 \text{ cm}^2 / (\text{V} \cdot \text{s})$. Finally, we have measured a minority carrier diffusion length up to 190 nm for passivated NWs showing an order of magnitude enhancement respect to the unpassivated one.

4 Modulation doped nanowires

The modulation doping is the doping of a heterostructure (e.g. *GaAs/AlGaAs*) implemented in such way that the resulting free electrons are spatially separated from the positive donor ions. As a result scattering of moving electrons on the dopant atoms is avoided leading to a superior electron mobility. In addition the nanowire geometry allows to switch between 3D, 2D and 1D electron transport in function of the doping concentration opening ways to interesting physical properties.

In this chapter we analyze *GaAs/AlGaAs* modulation doping structure. We investigate the effect of doping and geometrical parameters and we calculate the carrier concentration profile inside the nanowire. We observe the formation of 2D electrons layers and 1D channels in function of the doping concentration. We then experimentally measure the electron mobility in doped *GaAs* nanowires and we compare it with literature values mobility of modulation doping *GaAs/AlGaAs* nanowires.

Publication:

J. L. Bolland, S. Conesa-Boj, P. Parkinson, G. Tutuncuoglu, F. Matteini, D. Ruffer, A. Casadei, F. Amaduzzi, F. Jabeen, C. L. Davies, H. J. Joyce, L. M. Herz, A. Fontcuberta i Morral and M. B. Johnston, *Modulation doping of GaAs/AlGaAs core-shell nanowires with effective defect passivation and high electron mobility*, **Nano Letters**, **15**, 1336-1342, (2015);

4.1 Modulation-doped GaAs

The term *low dimensional system*, in the case of electronic transport, refers to a system in which the mobile charge carriers are constrained by potential barriers so that they lose one or more degree of freedom for motion. The system becomes two, one or zero dimensional, depending on whether the potential barriers confine the electrons in one, two or three dimensions, respectively. The most commonly used heterostructure for two-dimensional transport is composed of two semiconductors, GaAs and $Al_xGa_{1-x}As$, which have nearly the same lattice parameters. In the latter material, a fraction x of the Ga atoms in the GaAs lattice is replaced by Al atoms, thus keeping the III-V ratio the same. For $x < 0.45$ the semiconductor $Al_xGa_{1-x}As$ has a direct band gap. This system is used to create modulation doped heterostructures.

Modulation doping is a doping technique which spatially separates mobile carriers from their parent impurities. Extremely high carrier mobilities (μ) can be obtained due to this separation through a significant reduction in ionized impurity scattering. In this thesis modulation doped heterostructure with confined electron system dimensions have been obtained by introducing n-type dopant impurities in the $Al_xGa_{1-x}As$ at some distance to the interface, whereas the GaAs remains intentionally undoped. Some of the electrons introduced by the Si donors into the conduction band of the $Al_xGa_{1-x}As$ transfer into the lower-lying Γ conduction band of the GaAs. These electrons are confined in the nearly triangular well established by the conduction band discontinuity and the Coulomb potential of the parent ionized impurities (Fig. 4.1a).

The discovery of modulation doping in 1978 [142] led to an immediate improvement in the low-temperature mobility of GaAs because it afforded a physical separation of the electron carriers from the positively ionized donor parent atoms. This improvement has continued for several years leading to an increase of thin films mobility of four order of magnitude (Fig. 4.1b). The major source of scattering under control of the MBE grower is ionized impurity scattering from intentional or inadvertent impurities in either the GaAs channel or substrate, or the AlGaAs barriers. Ionized impurity scattering is expected to be practically temperature independent below 50 K. Thus, as the measurement temperature is reduced to a few degrees K, ionized impurity scattering becomes more and more dominant over the rapidly falling effects of optical and acoustic scattering, and it becomes readily possible to distinguish between samples of differing quality. Figure 4.1b testifies to the progress over the years in reducing ionized impurity scattering. L. Pfeiffer *et al.* also emphasize that ionized impurity scattering imposes no fundamental limit on the low-temperature mobility. In principle, the unintentional impurity content of the modulation-doped structure can be reduced indefinitely, and the undoped setback can be increased greatly so the mobility could yet rise by orders of magnitude at sufficiently low temperatures for sufficiently perfect samples [141]. On the other hand, at high temperatures, polar-optical-phonon scattering is the dominant scattering mechanisms and drastically reduce the modulation-doped GaAs mobility. This very large mobilities are possible because the heterointerface quality is excellent and the crystal periodicity across the interface is not disrupted. In fact, The lattice constant between of AlGaAs and GaAs matches within the 0.5%.

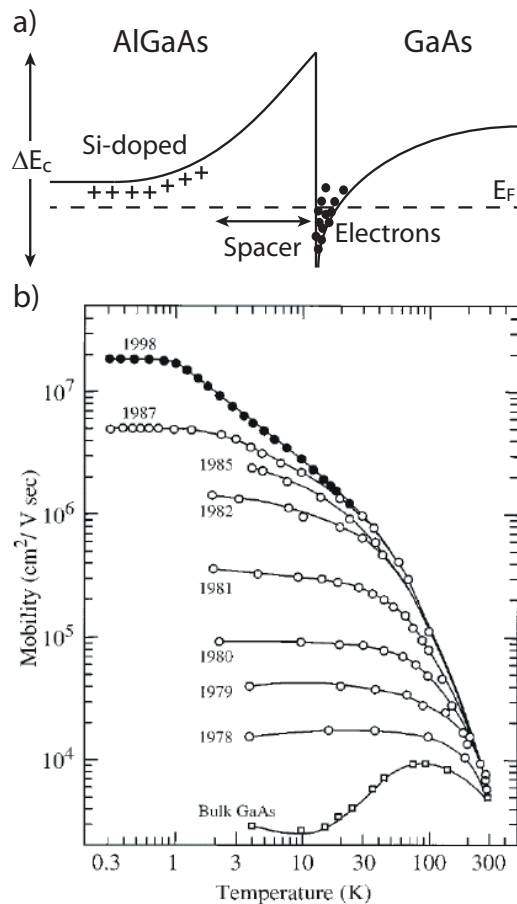


Figure 4.1: a) A sketch of the conduction band structure of a *GaAs/AlGaAs* heterojunction showing the confined electron position, the Fermi energy, the distance between doping position and interface (spacer) and the position of the Si-doped atoms. b) Hall mobility temperature dependence of the history of modulation-doped GaAs (from Ref. [141], *Rights managed by AIP Publishing LLC*). At high temperatures, μ is limited by scattering with photons of the bulk. At the lower temperatures, μ is limited by impurities and defects.

Figure 4.1b gives also a clear indication that the scattering mechanism in GaAs bulk is substantially different from the 2DEG scattering. To put light on this behavior we need to consider that various scattering mechanisms contribute to the mobility temperature dependence, which according to the Mathiesen rule can be added up as scattering rates to give a total scattering rate: $1/\mu = \sum_i 1/\mu_i$. Here some scattering type are listed, first discussed for the bulk 3D GaAs case (Fig. 4.2a):

- *Ionized impurities*: it's an impurity scattering and represent Coulomb scattering. This scattering is particularly important at low temperature, where the kinetic energy is small and electrons can be deflected by big angles. The temperature dependence of the mobility is $\propto T^{3/2} \log(T)$.
- *Deformation potential*: it's an electron-phonon scattering at the lattice deformation ($\propto T^{-3/2}$).
- *Polar scattering*: it's an electron-phonon scattering. GaAs is a polar crystal, lattice vibrations are accompanied by oscillating electric fields, particularly strong for optical phonons ($\propto T^{-1/2}$).

Chapter 4. Modulation doped nanowires

- *Piezo-electric scattering*: it's an electron-phonon scattering. GaAs is also a piezoelectric, meaning that a polarization field develops in response to a crystal deformation ($\propto T^{-1/2}$).

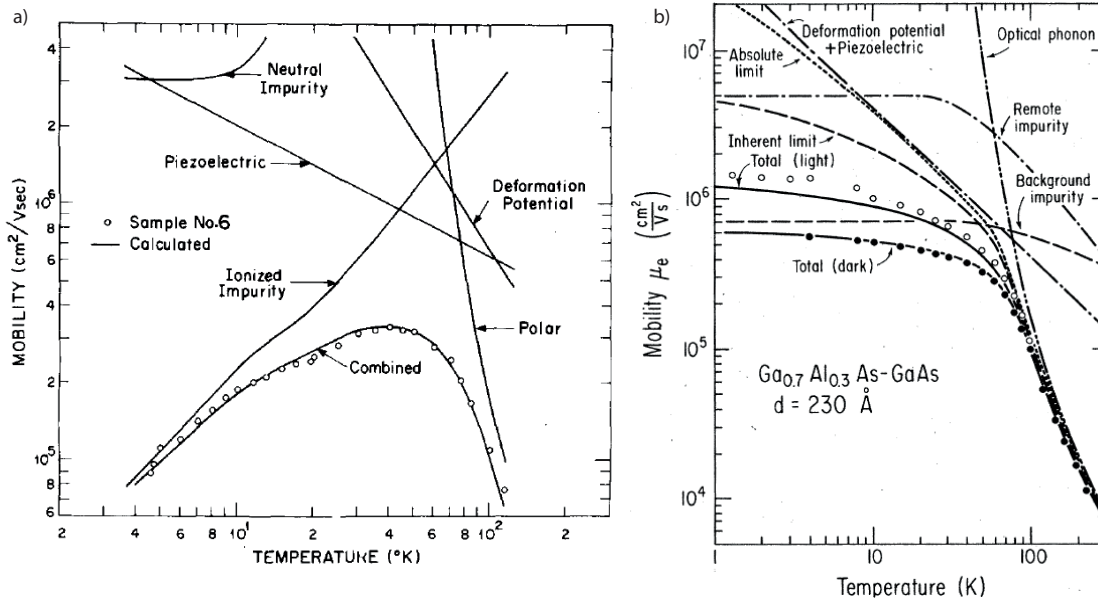


Figure 4.2: a) Experimental temperature dependence mobility of GaAs bulk materials, calculated mobility curves for each scattering process acting separately and for all scattering process combined (from ref: [143], Copyright ©1976 Published by Elsevier B.V. b) Temperature dependence electron mobility in GaAs/AlGaAs heterostructure. The experimental data are obtained in the dark (black points) and under illumination (white points) with a spacer thickness of 23 nm. The dashed line represent the different process and the continuous line the combination of them (from ref: [144]), Copyright ©1984, American Physical Society, Copyright ©2011 American Physical Society.

Scattering in a 2D electron gas is different from the bulk case because the screening and the phase space properties of the electrons are now 2D, while the scattering potentials are still three-dimensional. Decay of the Friedl oscillations in 2D is weaker than in 3D. Also, new scattering mechanisms arise due to the interface and remote impurities. Relevant mechanisms include (Fig. 4.2b):

- *Impurities*: now the ionized donor are spatially separated from the 2DEG by a spacer layer. The small residual donor density can be improved by simply obtaining cleaner materials. In principle to reduce the impurity scattering one could increase the spacer in order to put further away the donors. This would be correct, but the increasing thickness of the spacer would decrease the electron density. This effect will be further discussed in the next section.

4.2. Modulation doping simulations of the nanowires geometry

- *Interface roughness*: Interface imperfections and roughness represent deviation from the perfect crystal and can therefore create scattering.
- *Inherent limit*: the mobility that would result in a sample without the background impurities but including the remote donors.

4.2 Modulation doping simulations of the nanowires geometry

The modulation doped geometry can be reproduced in NWs by the use of radial heterostructure. In particular, in this thesis we study $GaAs/Al_{1-x}Ga_xAs$ modulation doped NWs as represented in figure 4.3.

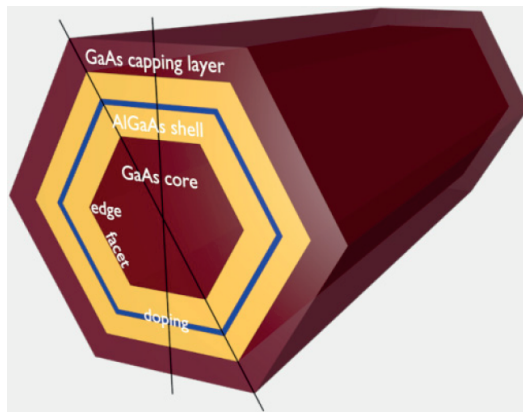


Figure 4.3: Schematics of a modulation-doped radial heterojunction. A GaAs core NW is covered by a AlGaAs shell, which is either n- or p-doped in the middle and capped by an additional GaAs layer. Eventually, an electron or hole gas forms in the core at the heterointerface with the AlGaAs shell. Reprinted with permission from [12] copyright ©2011 American Physical Society.

One of the first theoretical paper was published in 2011 by Bertoni *et al.*. They perform calculations to determine the electron and hole gas distribution in the NW. They observed that electron and hole gases can be tuned to different localizations and symmetries inside the NW core in function of the doping density and gate potential [12]. Electrons do not form a uniform 2DEG localized at the $GaAs/AlGaAs$ interface, but rather show a transition between an isotropic cylindrical distribution and a set of six quasi-1D channels at the core hexagonal edges. These and new calculations have been done in this thesis by the use of *nextnano*³ software, which consists of a Schrödinger-Poisson solver for modeling semiconductor NW structures.

4.2.1 Doping concentration

Now we consider a n-doped modulation doping NW. The geometrical parameters used in the calculations are reported in Table 4.1.

We investigate the electron density as function of the doping density (ρ), the doped layer width (w) and the doped layer material (AlGaAs or GaAs). Figure 4.4a shows a sixfold symmetry where quasi 1D channels are localized at the NW hexagonal edges. The charge density resembles a set of coupled quantum wires more than a 2DEG. Indeed while most of the charges are

Region	Thickness [nm]
Core radius r	40
AlGaAs spacer (d)	1-30
Doped layer (w)	3-10
AlGaAs capping	25
GaAs capping	7

Table 4.1: Radial dimensions of modulation doping NWs used in the calculations. The AlGaAs spacer and the AlGaAs doped layer thickness are respectively between 1 and 30 nm and 3 and 10 nm.

confined in relatively narrow channels at the edges, only a minor part of charges sits on the facets. This charge distribution is the result of high doping concentration ($\rho = 10 \cdot 10^{18} \text{ cm}^{-3}$) and a relatively small doped layer ($w = 3 \text{ nm}$). A reduction in ρ , from 10 to $5 \cdot 10^{18} \text{ cm}^{-3}$ (Fig: 4.4b) leads to a dramatically different electron distribution. For lower doping the charges are not anymore confined at the edges but instead they are localized along the full GaAs/AlGaAs interface leading the formation of a cylindrical 2DEG. As doping is reduced to $3 \cdot 10^{18} \text{ cm}^{-3}$ (Fig: 4.4c), the electron distribution loses any localization at the interface and becomes homogeneous in the core.

Another important aspect is the absolute value of the electron density. Because of the NW small dimensions, an electrical current can be obtained only for high charge density concentrations. In order to have carrier concentrations ρ above 10^{17} cm^{-3} the silicon doping concentration needs to be higher than $5 \cdot 10^{18} \text{ cm}^{-3}$. In practice, for high Si concentrations, Ketterer *et al.* observe the formation of silicon pairs and thus compensation [107]. This is related to the Coulomb interaction between charged defects during growth and limited the maximum free carrier concentration. Because of this limitation, increasing the Si doping above $3 \cdot 10^{18}$ would not have a corresponding effect in the increase of the electron concentration. To overcome this problem, we expand the doped layer (w) instead of increasing the doping concentration (ρ). Figures 4.4d, e and f show respectively the electron density distribution for modulation doping NWs with a shell thickness of 3, 5 and 10 nm and a Si doping density of 10, 5 and $3 \cdot 10^{18} \text{ cm}^{-3}$. In this way we compensate the reduction of the doping with a thicker doped region leading to a similar electron concentration for all the three configurations. The geometry "f" correspond, then, to the ideal case in terms of device electrical properties and maximum physical doping efficiency.

It is important to mention that the thickness of the doped layer cannot be indefinitely extended. Larger is the thickness, more the electrons will tend to stay in this doped region instead of migrate into the NW core. With 10 nm thick doped region already 10% of the carriers are confined in the doped shell and this percentage is increasing fast for larger thicknesses.

In figures 4.4g, h and i is shown the electron concentration of NWs with the same geometry and doping concentration of the previous figures 4.4d, e and f, but with a doped GaAs layer

4.2. Modulation doping simulations of the nanowires geometry

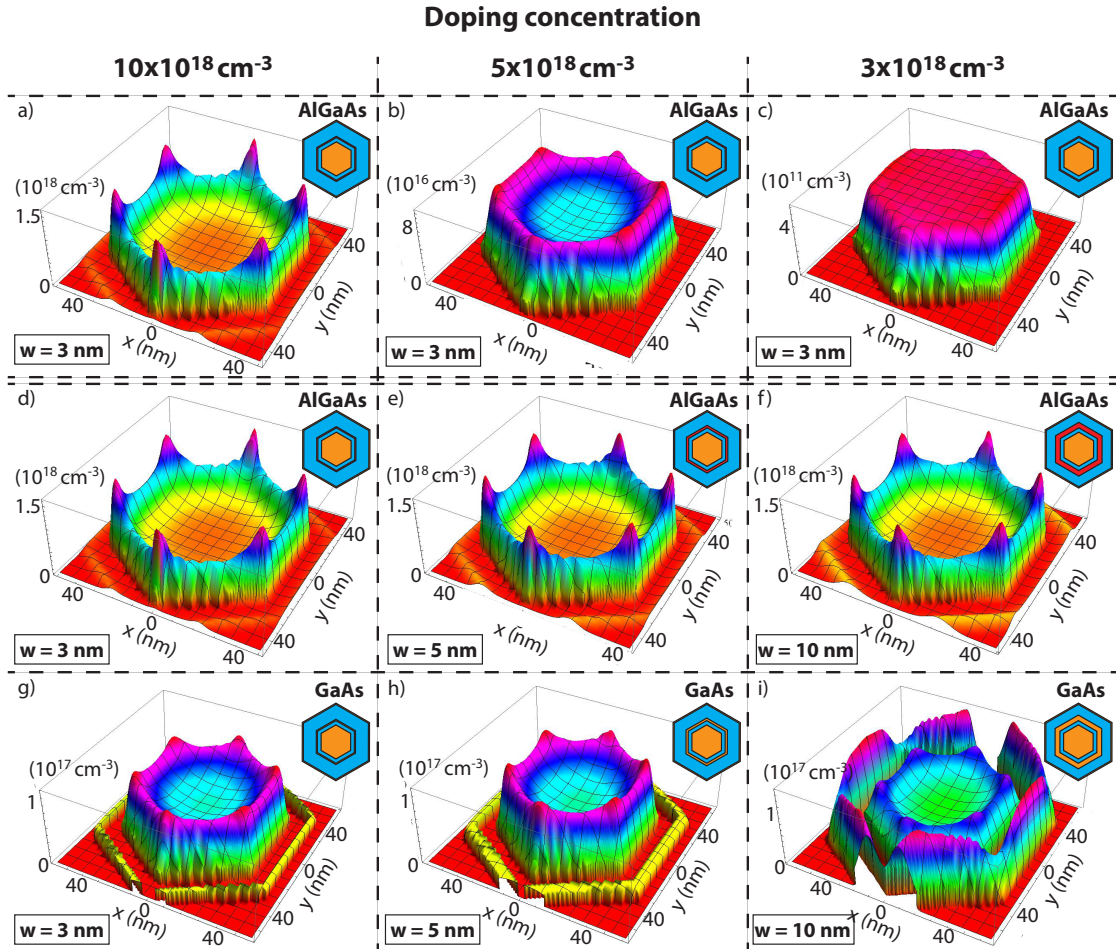


Figure 4.4: Electron density profile in MD NWs. The doping concentration is $10 \cdot 10^{18}$, $5 \cdot 10^{18}$ and $3 \cdot 10^{18} \text{ cm}^{-3}$ respectively for the first, the second and the third column. In a, b and c the AlGaAs doping layer thickness is 3 nm ; in d, e and f the AlGaAs doping layer thickness is 3 , 5 , 10 nm . In g, h and i the doped layer is GaAs and its thickness is respectively 3 , 5 and 10 nm . For all cases the spacer $d = 10 \text{ nm}$. The NW cross section geometry is represented on the top right of each figure.

instead of an AlGaAs one. Because Ga conductive band is lower than the one of AlGaAs, there is a formation of the quantum well in the GaAs doped layer. Electrons will first occupy the quantum well levels and then move to the core leading to the modulation doping behavior. When the doped GaAs layer is 10 nm (Fig. 4.4i), there are enough states in this layer to allow a large part of electrons to stay in the doped region instead of migrating into the core. In each case we observe a lower carrier density than in the case of the AlGaAs doped layer.

In conclusion we have investigated how the doping concentration and the thickness of the doped layer influence the electron density of a modulation doped NW. Considering the physical limitations of the doping efficiency related to the amphoteric behavior of Si in GaAs, we

observed that the maximum number of electron is achieved with $\rho = 3 \cdot 10^{18} \text{ cm}^{-3}$ and an AlGaAs doped layer thickness of 10 nm (Fig. 4.4f).

4.2.2 Spacer width

The basic concept of modulation doping is to separate the 2DEG from the parents ionized donors. This separation allows to limit the ionized impurity scattering from the remote centers. Walukiewicz *et al.* investigated the electron mobility in function of the distance, d , between the 2DEG and the doped region [144]. For $d < 10 \text{ nm}$ the electron mobility decreases rapidly with d . For $d \geq 15 \text{ nm}$, the impurity centers, generated by the doping, are sufficiently far to not affect the 2D electron mobility. Therefore modulation doping exhibits the higher mobility for large spacer width. However, an increase of d leads to a decrease in the electron density, which has a deleterious effect on conductivity. In NWs, we are particularly careful to have as much carrier as possible in order to observe conductivity. Figures 4.5a, b and c show the electron density of a MD NW with spacer d of respectively 1, 10 and 30 nm . We observe that by increasing d more carriers stay in the doped region instead of migrating into the core. For $d = 30 \text{ nm}$ around 40% of electrons are confined in the doped region limiting the performance of the MD structure. In order to avoid this we believe that in modulation doped NWs the optimal spacer is between 10 and 15 nm

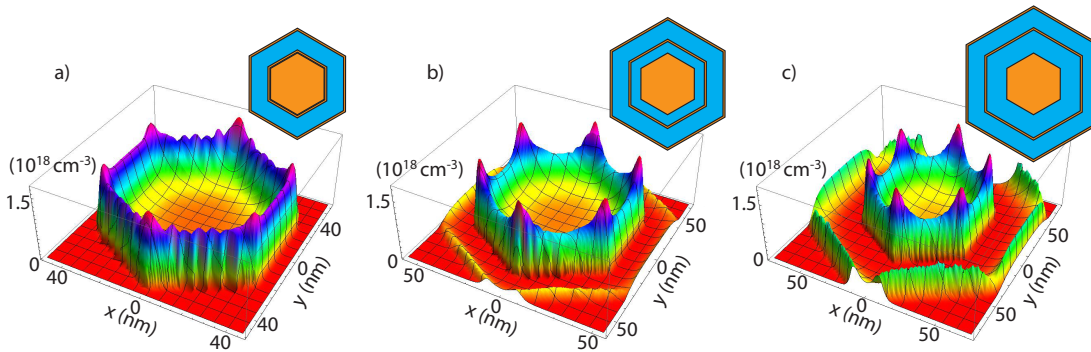


Figure 4.5: Electron density profile in MD NWs in function of the spacer d calculated with NextNano. d is 1, 10 and 30 nm in respectively a, b and c. The NW cross section geometry is represented on the top right of each figure.

4.2.3 $Al_xGa_{1-x}As$ alloy composition

The Al concentration in an $Al_xGa_{1-x}As$ material has mainly two effects on modulation doping structures: it changes the band gap of the AlGaAs layer and it affects the dopant activation energy E_a .

The band-gap energy of $Al_xGa_{1-x}As$ depends on the Al concentration and it varies between

1.42 eV (GaAs) and 2.16 eV (AlAs) according to the following equations:

$$\begin{cases} x \leq 0.45 & E_g = 1.424 + 1.247 \cdot x \text{ eV} \\ x \geq 0.45 & E_g = 1.9 + 0.125 \cdot x + 0.143 \cdot x^2 \text{ eV} \end{cases} \quad (4.1)$$

For $x \leq 0.45$, $Al_xGa_{1-x}As$ has a direct band-gap, characteristic which is especially important for optoelectronic properties. For $x \geq 0.45$ the band-gap is indirect. The AlGaAs band-gap energy determines the position of the AlGaAs valence and conduction bands. In the heterostructure $AlGaAs/GaAs$, the AlGaAs conduction band is always higher than the GaAs one leading to a migration of the free electrons from the higher energy compound (AlGaAs) to the lower one (GaAs). Modulation doping structures (AlGaAs/GaAs) can then be realized for any $x > 0$ but, since Al concentration also influence the quality of the contacts, in this thesis we focus on small x values ($0.20 \leq x \leq 0.33$).

In the early 80s several works have been performed in order to establish the activation energy of shallow and deep traps in AlGaAs bulk materials. In ternary compounds the electronic properties of defects vary with alloy composition, but there are major discrepancies in literature regarding the activation energy levels in $AlGaAs$. For the purpose of this thesis we are only considering the references more representative. In general in $Al_xGa_{1-x}As$ with $x > 0.25$ a large portion of dopants (S, Se, Te, Si, Ge and Sn) appear as deep centers with activation energy ranging from 190 and 560 meV [145, 146]. It is thought that the reason that the concentration of deep states is higher than in GaAs due to the reactivity of Al. In contrast with papers claiming a sharp change in E_a by varying Al concentration [147], particularly relevant, is the work by Schubert *et al.* in 1984 observing that the thermal activation energy of deep donors in $Al_xGa_{1-x}As$: Si does not significantly change with the alloy composition [148]. Temperature-dependent Hall-effect measurements were reported and analyzed for n-type $Al_xGa_{1-x}As$ of composition $0 \leq x \leq 0.40$ grown by molecular-beam epitaxy and highly doped with Si ($Si \geq 5 \cdot 10^{17} \text{ cm}^{-3}$). The thermal activation energy of the deep donor was determined to be $E_a = 140 \pm 10 \text{ meV}$. In this thesis we follow the results of Schubert *et al.* and we use $E_a = 140 \text{ meV}$.

4.3 Electron mobility in nanowires

In this section we compare the electron mobility of GaAs:Si n-doped NWs with the electron mobility of n-type modulation doping NWs.

4.3.1 GaAs:Si nanowires

The GaAs:Si n-type doped NWs have been grown in our MBE with a core-shell structure: an intrinsic core and a n-doped shell. The NW core has been grown at a nominal Ga growth rate of 0.3 \AA/s , As_4 partial pressure of $5.5 \cdot 10^{-6} \text{ Torr}$, at a temperature of 640°C and with 7 rpm rotation. Then, the MBE conditions were changed in order to obtain the shell growth; gallium

droplet was consumed, and the shell has been grown at the nominal Ga growth rate of 0.95 \AA/s , As_4 partial pressure of $1.3 \cdot 10^{-5} \text{ Torr}$ and temperature of $465^\circ C$, with a nominal shell thickness of 40 nm . Silicon has been added to the process at the beginning of the shell growth. The electrical contacts were made with $Pd/Ge/Au$ ($40/170/100 \text{ nm}$) directly in contact with the doped shell.

The conductivity of $GaAs:Si$ n-doped NWs is obtained by extracting the NW resistance from four point measurement. Around 10 devices have been analyzed giving a conductivity of $\sigma = 5300 \pm 400 \text{ \Omega/m}$. Figure 4.6a shows an example of I-V curves for 2 and 4 point measurements. We can observe the non linearity of the 2 point measurements indicating that the contacts are not ohmic. Therefore, we need the four points contacts method to extract the resistance which is obtained by the reciprocal of the I-V curve slope. According to the MBE calibration

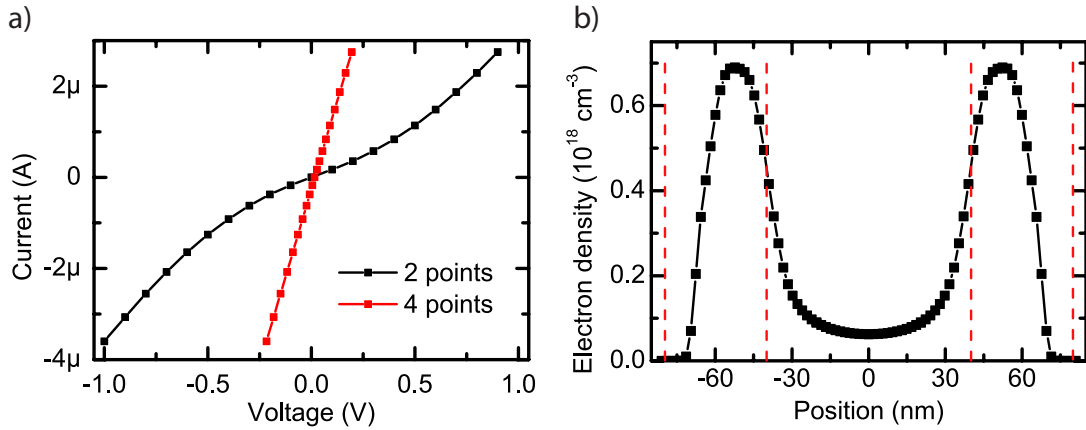


Figure 4.6: a) I-V example of a $GaAs:Si$ n-doped NW with 2 and 4 points configuration. The non linearity of the 2 point measurements shows the contacts are not ohmic. b) Electron distribution profile along the NW cross section. The simulation has been performed with NextNano by assuming a shell doping concentration of $5 \cdot 10^{18} \text{ cm}^{-3}$.

and the NW growth parameter, the n-type shell has a doping concentration of $5 \cdot 10^{18} \text{ cm}^{-3}$, while the core is intrinsic $GaAs$. The electron carrier distribution in the NW is calculated with NextNano considering the pinning of the Fermi level at the surface (0.5 eV) and a doping activation energy of 6 meV (Fig. 4.6b). Electrons are spaced from the NW surface due to the pinning of the Fermi level and a small part of carriers is localized in the intrinsic core region. By integrating on a cylinder we obtain that 87% of electrons are confined in the shell and the remaining 13% in the core.

The NWs mobility, μ , is estimated from

$$\mu = \frac{\sigma}{n \cdot e} \quad (4.2)$$

where n is the carrier concentration and e is the electron charge. We obtain a total NW mobility $\mu = 1000 \pm 100 \text{ cm}^2/V \cdot s$. According to the work of Boland J. F. *et al.*, the electron mobility

in analogues GaAs intrinsic cores is $\mu_{core} = 2200 \pm 300 \text{ cm}^2/V \cdot s$ [21]. We can then consider that carriers traveling into the core have a different mobility than the ones traveling in the doped shell, in particular we can think to have two parallel channels (the core and the shell) where the total conductivity, σ , is the sum of the individual conductivity, $\sigma = \sigma_{core} + \sigma_{shell}$. This method allow us to determined the electron mobility in the doped shell $\mu_{shell} = 700 \pm 100 \text{ cm}^2/v \cdot s$. This result is consistent with literature values for thin films with analogues doping concentration [149], and it is one of the highest mobility reported for GaAs doped NWs. These good electrical properties are also an indication of the NWs high crystalline quality.

4.3.2 AlGaAs/GaAs:Si modulation doping nanowires

In modulation doped semiconductor heterojunctions the impurity scattering is reduced due to the spatial separation between ionized (donor) impurities and electron carriers. In the last years few groups have reported about electrical properties and mobility in AlGaAs/GaAs modulation-doped NWs by the use of different techniques. In the late 2013, the group of Abstreiter demonstrated 1D and 2D free electron gases in modulation doping *GaAs/Al_{0.16}Ga_{0.84}As* core-multishell NWs with a high electron mobility using spatially resolved resonant inelastic light scattering and PL measurements. They obtained inhomogeneous electronic properties along the individual NWs and in certain regions they estimate an electron mobility up to $5 \cdot 10^4 \text{ cm}^2/V \cdot s$ [13]. The same group in 2015 measured the field effect mobility of analogues NWs. They observe the formation of a well-confined free electron gas resulting in a low temperature electron mobility of $5 \cdot 10^3 \text{ cm}^2/V \cdot s$ [150].

A different approach was used by Michael B. Johnston *et al.* They employed optical pump-terahertz probe (OPTP) spectroscopy to measure carrier transport and dynamics at room temperature. As a non contact technique, OPTP spectroscopy circumvents the problems associated to traditional contact-based electrical measurements. It offers a rapid noncontact method of characterizing and hence further improving the electrical properties of NWs heterostructures. Low doped *GaAs/AlGaAs* modulation doping NWs have been analyzed with this technique and an electron mobility of $2200 \pm 300 \text{ cm}^2/V \cdot s$ was found at room temperature [21]. This value is high for GaAs NWs and they show that there is no significant degradation of the electron mobility when compared to an undoped GaAs NW reference.

4.4 Conclusions

We have reported the basic concepts of modulation doping focusing the attention on the doping and the structure geometry. We calculated the free electrons concentration in a modulation doping NW geometry and we have observed the formation of confined electron gas resulting in a 2D layer or six 1D electron channels depending on the doping concentration. We have finally compared the electron mobility of a doped GaAs NW and a modulation doping one. The mobility values for a GaAs:Si NW are calculated with electrical measurements to be around $700 \pm 100 \text{ cm}^2/V \cdot s$. Literature values for room temperature modulation doping

Chapter 4. Modulation doped nanowires

NWs mobility are around $2200 \pm 300 \text{ cm}^2/V \cdot \text{s}$, confirming that these structures appear to be excellent for retaining high electron mobility.

5 Photonic-plasmonic coupling of GaAs NWs and nanoantennas

The small dimensions and the unique opto-electrical properties render nanowires as excellent candidates for electronic and photonic applications. Engineering the light interaction on the NW using metal antennas opens up many new possibilities for the design of different devices with desired properties.

In this chapter, we investigate the resonant coupling of semiconductor NWs and metallic antennas and, in particular, we use Au dimer nanoantennas to couple light into GaAs NWs and Au Yagi-Uda antennas to modify the nanowire directional emission. The precise control of the nanoantennas position leads to the opportunity of engineering coupled systems able to enhance the absorption of determined wavelength and polarization. In the first part of chapter the state-of-the-art of interaction between NWs and metal nanostructures is described. We then, demonstrate the plasmonic coupling between metal nanoantennas and individual GaAs nanowires (NWs). In particular, by using dark-field scattering and second harmonic generation spectroscopy in partnership with analytical and full-vector FDTD modeling, we show controlled electromagnetic coupling between plasmonic nanoantennas and resonant nanowires and show that we can tailor their nonlinear optical response by engineering tuning the near-field plasmonic coupling regime. In the last part, we demonstrate the possibility of controlling the directional emission of individual GaAs nanowires by coupling this emission to Yagi-Uda optical antenna. In particular, we replace the metallic feed element of the nanoantenna by an individual nanowire and measured the photoluminescence as a function of the emission angle. The precise tuning of the dimensions of the metallic elements can lead to a strong directionality of emission.

Publications:

A. Casadei*, E. F. Pecora*, J. Trevino*, C. Forestiere, D. Ruffer, E. Russo-Averchi, F. Matteini, G. Tutuncuoglu, M. Heiss, A. F. i Morral and L. Dal Negro *Photonic-plasmonic coupling of GaAs single nanowires to optical nanoantennas*, Nano Letters, 14, 2271-2278 (2014)

Chapter 5. Photonic-plasmonic coupling of GaAs NWs and nanoantennas

M. Ramezani, A. Casadei, G. Grzela, F. Matteini, G. Tutuncuoglu, D. Ruffer, A. Fontcuberta i Morral and J. Gomez Rivas, *Hybrid semiconductor nanowire-metallic Yagi-Uda antennas*, **Nano Letters**, **15**, 4889-4895 (2015).

*equal contribution.

5.1 State of the art

5.1.1 Metallic nanoparticles: light interaction

The ability of metallic nanoparticles to efficiently absorb and scatter light has been well known since the 4th century. At that time, it was known that such particles, when properly sized, would produce brilliant colors that would not degrade over time. This effect, was much exploited for the fabrication of glass windows for churches and cathedrals. Despite their extensive use, the physics behind this effect remained unexplained until 1857, year in which Faraday performed the first extensive study on the subject. During his work, he observed a clear link between the color of colloidal solutions, the metal and the fabrication method employed for the production. Later, in 1908, Mie provided the first mathematical description of the phenomenon [151]. However, even though Mie's theory was able to explain the reasons behind the different colors of the particles as a function of their size, a complete grasp of the concepts was not yet achieved. After this pioneering work, a long time passed before the concept of plasmons was proposed for the first time in 1957 by Ritchie [152].

Since the dimensions of metal nanostructures are smaller than the wavelength of the exciting light, energy can be confined in a small spatial region through the local excitation of surface plasmon resonances. The electric field of an incoming light wave on a metal nanoparticle induces a polarization of the (free) conduction electrons with respect to the much heavier ionic core. The positive charges in the particle are assumed to be immobile and the negative charges, that is, the conduction electrons, move under the influence of external fields. Therefore, a displacement of the negative charges from the positive ones occurs when the metallic nanoparticle is placed in an electric field, that is, there results a net charge difference at the nanoparticle boundaries. This, in turn, gives rise to a linear restoring force to the system. As a consequence, a bipolar oscillation of the electrons is created (with a particular time period), and this is known as the surface plasmon oscillation. Theories and experiments agree that the shape, the material, the dimension and the dielectric environment are of fundamental importance [153, 154]. When metallic nanoparticles are in resonance condition they act as lenses and they can enhance the light absorption of solar cell devices [99, 155, 156]. In 2010 Atwater and Polman theoretically studied different geometrical configuration in order to maximize the light absorption and reduce the energy lost using spherical gold nanoparticles [157]. They described three ways (Fig. 5.1) of reducing the physical thickness of the photovoltaic absorber layers while keeping their optical thickness constant.

First, metallic nanoparticles can be used as sub-wavelength scattering elements to couple and trap propagating plane waves into the absorbing material; second, they can be used as sub-wavelength antennas that localize the plasmonic near-field in the semiconductor material and third, they can couple sunlight into surface plasmon modes supported at the metal/semiconductor interface.

Once the potential of metal nanostructures became obvious, researchers thought of trans-

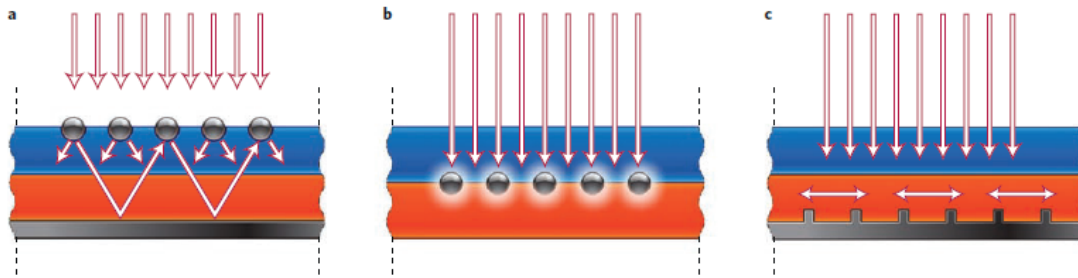


Figure 5.1: a) Light trapping from metal nanoparticles at the surface of solar cell. b) Light trapping by excitation of localized surface plasmons in metal nanoparticles embedded in the semiconductor. The excited particle near-field causes the creation of electron-holes pairs. c) Light trapping by the excitation of surface plasmon polaritons at the metal/ semiconductor interface. From [157]. Copyright ©2010, Rights Managed by Nature Publishing Group.

posing the well-known concept of antennas in the radio wavelength regime to plasmonics. A plasmonic antenna could in fact combine field concentration in the gap and localized surface plasmon resonances in a unique device working in the visible range. The first demonstrations of such a device appeared in 2005 [158, 159]. The experimental realization showed immediately the potential hidden inside the squeezing of light into the near-field. Very high fields in the gap of the dipole/bowtie antenna were used for the first time and the expansion of the field of plasmonics was almost instantaneous as several new applications based on the concept of nanoantennas were proposed. The objective of optical antenna design is equivalent to that of classical antenna design: to optimize the energy transfer between a localized source or receiver and the free-radiation field. In certain recent studies, however, the term *optical antenna* has clearly been stretched beyond its common definition in radiowave technology. An antenna is not simply a resonator or a strong scatterer. Instead, it is defined by its function, namely as a transducer between free radiation and localized energy. In analogy with the electromagnetic antenna, we define the optical antenna as a device that converts freely propagating optical radiation into localized energy, and vice versa.

Among several realizations of plasmonic antennas, dipole antennas have shown particularly good performances in terms of field enhancement, light confinement and control over the spectral features [160, 161]. In fact, these antennas have only two main geometrical parameter that must be controlled, the arm length and the gap width. The first one determines where the resonance will be in the radiation spectrum and the second controls the coupling between the arms as well as the near-field enhancement. This simplicity implies robustness from the fabrication point of view with evident advantages for the practical utilization of these structures and their optical characterization. Figure 5.2 shows examples of dipole nanoantennas.

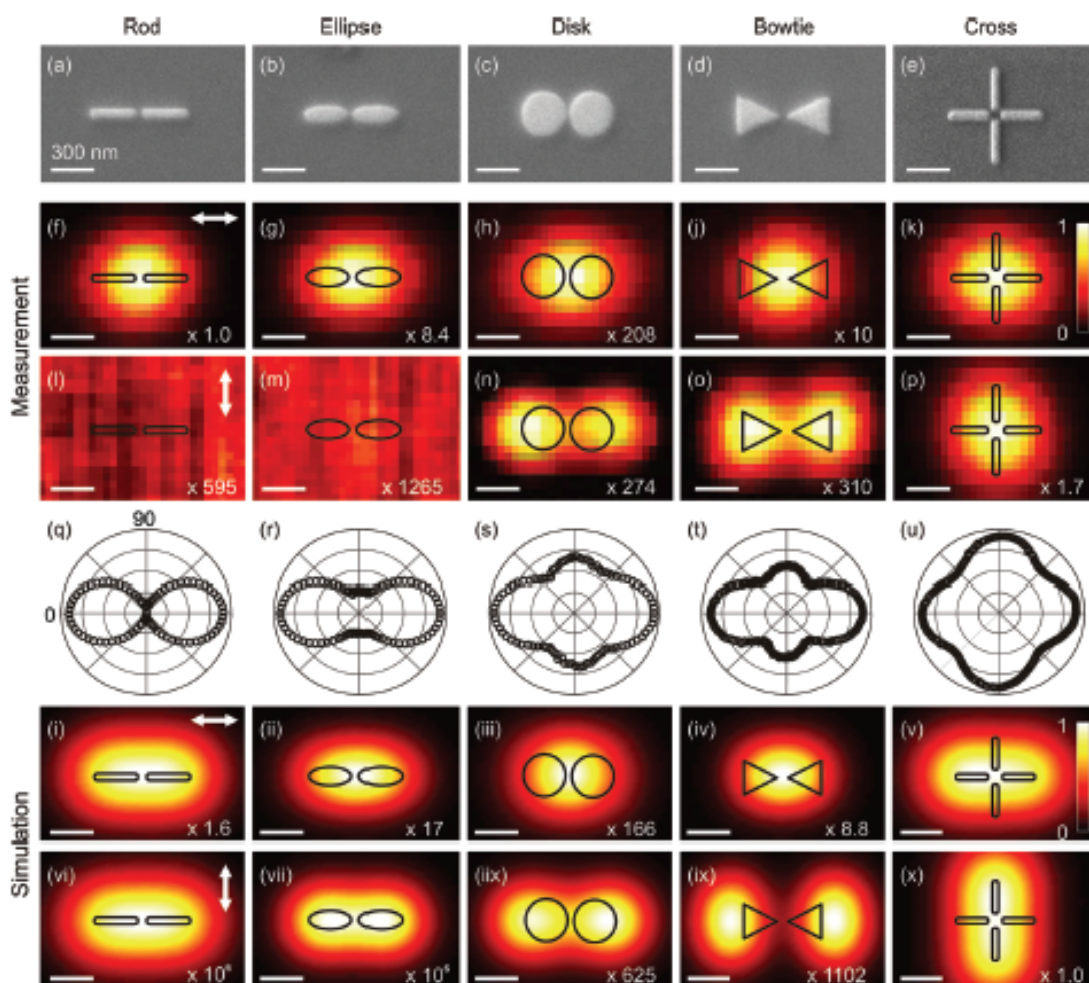


Figure 5.2: Spatially resolved third-harmonic emission from five gold nanoantennas of different shape. (a-e) Scanning electron microscope images. (f-p) Measurement. The metal nanostructures are scanned through the focus of an oil immersion objective ($NA = 1.3$) and excited by femtosecond laser pulses in the near-infrared. Third-harmonic emission intensity is depicted in a normalized color scale as a function of position, recorded for horizontal (f-k) and vertical (l-p) linear polarization of the excitation. (q-u) Polar plots of the third root of the measured third-harmonic intensity as a function of the polarization angle of the exciting beam. (i-x) Boundary element simulations of the third-harmonic intensity for antenna geometries as in the experiment with horizontal (i-v) and vertical (vi-x) polarization of the excitation. All scale bars are 300 nm . Reprinted with permission from [160]. Copyright ©2012 American Chemical Society.

5.1.2 Optical properties of semiconductor nanowires

The optical properties of semiconductor nanowires (NWs) are currently at the center of an intense research effort due to their potential applications in a number of nanoscale optoelectronic devices, such as tunable and enhanced light sources[19, 162, 163], solar

cells[45, 164, 16, 165, 166] and photodetectors[94, 97], optical switches[167], non-linear devices and modulators[168]. NWs with engineered composition, size and morphology offer the possibility to control the electronic structure and the linear and non-linear optical properties of semiconductor materials[169].

The interaction of light with NWs that have diameter comparable to optical wavelengths can be described with Mie scattering theory, i.e, the solution of Maxwell's equations. This approach has been used in literature to describe the extinction, scattering and absorption of plane waves incident on a NW [98, 170, 171]. Analytical solutions are possible for an infinite long cylinder in a homogeneous media, but numerical calculations need to be conducted for more complex systems. An infinite long cylinder supports waveguide modes, that will be further discussed in the next chapter. These modes can be either bound to the cylinder and propagate along its axis, or can radiate into the surrounding medium. In the first case we would have guided modes particularly important for lasing [172, 173], in the other case leaky modes.

5.1.3 Nanowires and metal nanostructures: coupled systems

Recently, the engineering of NWs supporting distinctive resonances, like the ones predicted by the classical Mie theory[174], has been proven as a convenient pathway to enhance light-matter coupling[175]. Moreover, resonant metallic nanostructures supporting traveling or localized SSPs have been deeply investigated as a powerful approach to manipulate optical radiation at the sub-wavelength scale[176, 177, 178, 154, 179]. As shown in the previous paragraph, plasmonic nanoparticle arrays and nanoantennas have shown the ability to strongly concentrate and increase the intensity of local electromagnetic fields [180]. However, while a significant amount of work has been devoted to the understanding of the optical responses of individual semiconductor NWs and individual plasmonic systems, little is currently known on their optical coupling regime and synergistic properties.

In 2011 C. Colombo and coauthors [99] investigated a hybrid system formed by a GaAs NW with a radial p-i-n junction and metal nanoparticles. They observed that engineering of light absorption in semiconductor NW through the leaky mode resonances can be tuned by choosing the interaction with SPP modes on the particles. Light absorption intensity is modulated by the effect of the substrate and the metal particles, but despite the intent to enhance the NW absorption, the overall interference led to a reduction of absorption in comparison with the single NW absorption (fig: 5.3).

Colloidal arrays of plasmonic nanoparticles and lithographically defined metallic nanocylinders coupled to semiconductor NWs have been also explored. They constitute a novel metal-dielectric interacting systems that enhance the optical response of their individual components[181]. The combination of the mature semiconductor NWs platform with the nanoplasmonics technology could potentially open the way to novel technological applications. These could open the possibility to leverage strongly confined optical fields in order to manipulate the linear and nonlinear optical responses (i.e., scattering, absorption, emission,

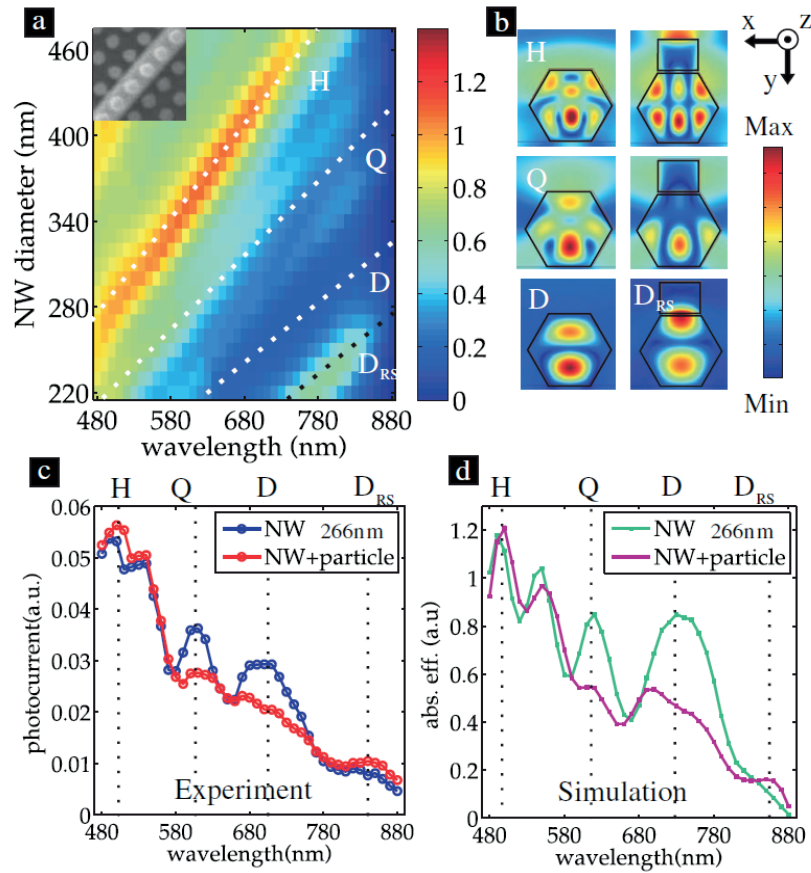


Figure 5.3: a) Simulation of the absorption efficiency for an NW with metal particles deposited on the top facet with respect to the nanowire radius and wavelength. The different letters label the resonant modes of the nanowire: H-hexapole, Q-quadrupole, D-dipole, D_{RS} -dipole red shifted. b) Plots of the absolute value of the magnetic field in the z-direction. The left column shows the field patterns in a 266 nm diameter NW obtained without metal particles for the different resonant modes while in the right one the modification of these patterns by the metal particle is reported. The color scale used is the same for the picture in the left and in the right column. c) Photocurrent as a function of the incoming wavelength for a bare nanowire with a diameter of 266 nm (blue) and for a nanowire with a particle (red). d) Simulation of absorption efficiency for the same nanowire diameter with (light blue) and without (magenta) metal particles. From [99]. *Copyright ©Institute of Physics and IOP Publishing 2010.*

second harmonic generation) of semiconductor and metal structures at the nanoscale.

5.2 Sample preparation

GaAs nanowires were grown on Si(111) un-doped substrates by the Ga-assisted method in a DCA P600 solid source MBE system[40, 39]. The growth parameter were set in order to have

a rotation of 7 rpm, a flux of Ga equivalent to a planar growth rate of 0.3 Å/s, a substrate temperature of 640°C, and a V/III beam equivalent pressure ratio of 50. These conditions lead to a GaAs diameter of around 55 nm and a length of 12 μm. After the growth of the NW core, 4 nm Al_xGa_{1-x}As and 3 nm intrinsic GaAs shells are obtained by turning growth conditions to those corresponding to two-dimensional epitaxy[55], leading to an overall NW diameter of around 70 nm. The concentration of Al(x) in the AlGaAs shell is around 0.3. This passivation layer avoids the oxidation of the GaAs core surface, offering opportunities to investigate the intrinsic properties of the material[125, 51]. We also investigated p-type Si doped GaAs NWs. In this case the core has been grown with the same parameters described above and with an additional flux of Si that leads to a doping concentration of around 5 × 10¹⁸ cm⁻³. These NWs have no AlGaAs capping shell, they are 12 μm long and their diameter measures 70 nm. In our work we compared both types of NWs and obtained identical outcome. This comparison is important also in views of next stage experiments where the NWs are electrically contacted and photoconductivity measurements are performed (chapter 6). Indeed electrical measurement are only possible on doped NWs.

The NWs grow along the <111> direction, with six facets belonging to the <110> family. They mainly present a zinc-blende crystal structure with 0 to 4 twins per μm. This structure also guarantees there is no orientation dependence in the SH-G. In addition we use circular polarized light in order to avoid the effect of the directional polarization. To fabricate the samples on the glass substrate we used electron beam lithography (Vistec EBPG5000) to position the nanoantennas in close proximity to the NW surface and along its axis as described in chapter 2.

Figure 5.4a displays a schematic of the structure of a representative plasmonic antenna-coupled NW sample investigated in this study.

The nanoantennas consist of dimers of Au cylindrical nano-disks with 200 nm diameter and 30 nm of height. The nanoantenna feed-gap regions host the individual NWs. We varied the gap distance from 500 nm to 90 nm in order to investigate the effect of tunable plasmonic near-field coupling. For 90 nm gap the average distance between the nano-disks in the dimer antennas and the NWs is of the order of just few nanometers, requiring an extremely precise position control. The real devices present small deviations from the ideal geometry. These discrepancies come from the variation in the NW sizes and from the alignment between wire and nanoantenna arrays. In particular, the distance between a nanoantenna disk and the NW can change up to 40 nm from the ideal geometry leading in some cases to the superposition of the gold disk and the nanowire. Nevertheless, these NW misalignments do not affect our experimental measurements. In fact, in our SH-G set-up we reduce local deviation by focusing the laser light on the center of each system. Misalignments, if any, are negligible at these locations. Some small deviations arise from the nanowire size. In fact, we observed a slight tapering of our nanowires (diameter variation of about 5 nm from one side to the other of the wire), and a statistical distribution of the nanowire diameter. In the optical measurements, we analyzed nanowires having diameter in the range between 61 nm and 77 nm. The longitudinal

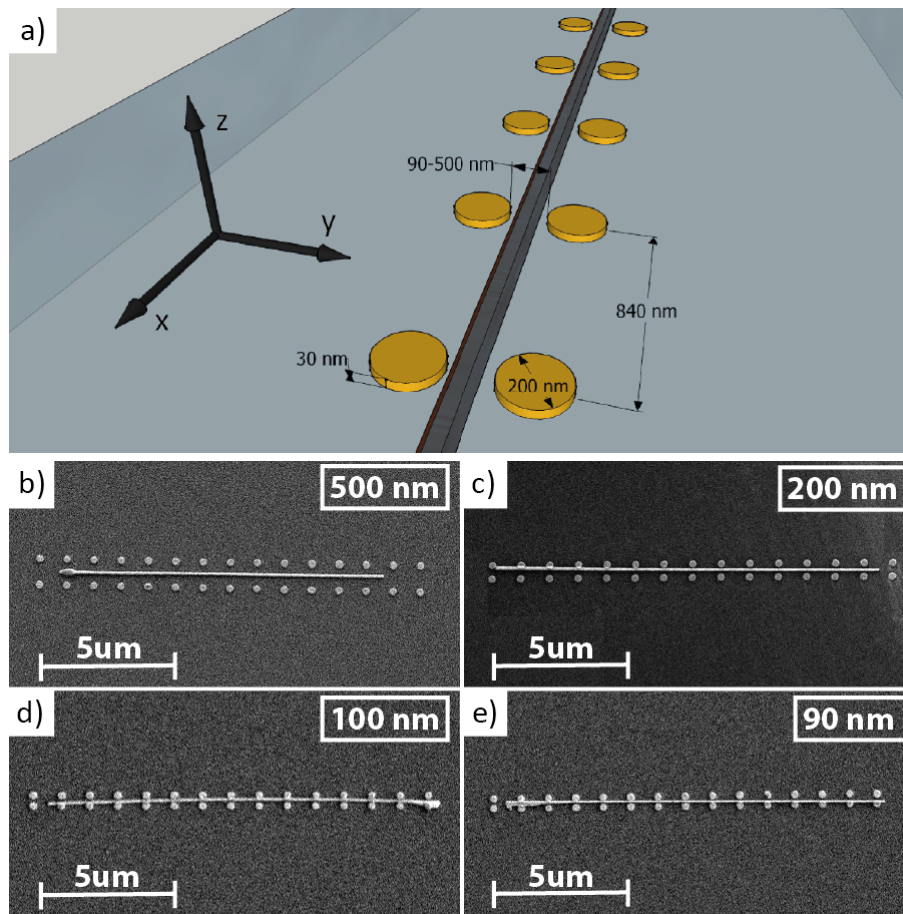


Figure 5.4: (a) Schematic of GaAs NW coupled to nanoantenna with all the geometrical parameters. SEM micrographs of (b) NW-coupled antenna with $d = 500$ nm, (c) NW-coupled antenna with $d = 200$ nm, (d) NW-coupled antenna with $d = 100$ nm, and (e) NW-coupled antenna with $d = 90$ nm. Copyright ©2014, American Chemical Society.

spacing (i.e., x-direction) of the nanoantennas along the length of the NWs is kept fixed to 840 nm. In Fig. 5.4 we also show the SEM images of the devices analyzed as a function of the gap distance: $d = 500$ nm (b), $d = 200$ nm (c), $d = 100$ nm (d), and $d = 90$ nm (e).

5.3 Photonic-plasmonic coupling of GaAs NWs with disk nanoantennas

5.3.1 Dark field scattering

We first investigated dark field scattering of individual NWs as well as antenna coupled NWs, both numerically and experimentally. The single NW is a well-known optical system, accurately modeled by analytical scattering theory in the limit of large aspect ratio.

The scattering cross sections of individual NWs have been calculated using analytical Mie theory under plane wave normal incidence (i.e., perpendicular to the NW axis) considering a NW of circular cross section and incident unpolarized radiation. We have employed this approach to better understand the physical origin of the scattering spectra of NWs. The fused silica substrate is considered as an effective host medium with average dielectric constant. Therefore, we modeled the responses of NWs on an actual silica substrate as well as of the complex antenna-coupled NW structures were modeled by 3D FDTD analysis using the commercial software package Lumerical FDTD Solutions.

The material dispersion parameters of the GaAs NWs and the fused silica substrate are derived from Palik[182], while the optical dispersion of Au nanocylinders is modeled using experimental data as reported in literature[182]. In the FDTD calculations, the simulation grid size surrounding the Au nanoparticles and the NW was set to 2 nm in all three dimensions. We used plane wave excitation at normal incidence (i.e., along the z-axis), as labeled in Figure 5.4a. Perfectly matched layer (PML) boundary conditions to ensure perfect absorption of electromagnetic radiation at the simulation boundaries.

The spectra were acquired using an Olympus IX71 microscope with a $50\times$ long-working distance objective (N.A 0.5) for collection of dark field scattering. The samples were illuminated with a 100 W halogen lamp which was focused on the sample plane using a dark field condenser (N.A 0.92 – 0.80). Scattered light was collected and analyzed with an Andor Shamrock 750 mm focal length spectrometer using a 600 lines/mm grating blazed at 500 nm . We recorded the spectra with an Andor iDus CCD camera (DU420A). These were then background corrected, and corrected for the excitation profile of the lamp and grating efficiency. Additionally, spatial filtering at the CCD detector was used for background noise reduction. The calculated scattering cross sections are obtained by the average of two calculations carried out under incident light longitudinally and transversely polarized with respect to the NW axis. These were compared with experimentally measured dark-field scattering spectra obtained under unpolarized light on the fabricated devices.

In Figure 5.5 (left panels) the calculated scattering cross-sections by the analytical Mie theory and the 3D FDTD simulations are plotted for the isolated NW (a), as well as the antenna coupled NWs (b-d). In the right panels the corresponding experimental data are shown. The analytical solution (panel (a), dashed line) for the single NW features two main resonances in the investigated range. A similar behavior is observed in the FDTD results (solid line), which appear red-shifted due to the influence of the substrate. At shorter wavelengths a narrow peak arises at 450 nm , which corresponds to a resonant feature in the GaAs optical constants[182]. On the other hand, a broad resonant peak centered on 850 nm is also observed in Fig. 5.5a, which is due to the NW leaky modes excited by the longitudinal light polarization. The experimental data exhibit significantly broadened spectral features compared to the calculated spectra. This is due to the finite cone of excitation angles used in the experimental dark-field configuration. Additionally, this deviation can be caused by some differences in the optical parameters of the fabricated material compared to the tabulated ones used in the

5.3. Photonic-plasmonic coupling of GaAs NWs with disk nanoantennas

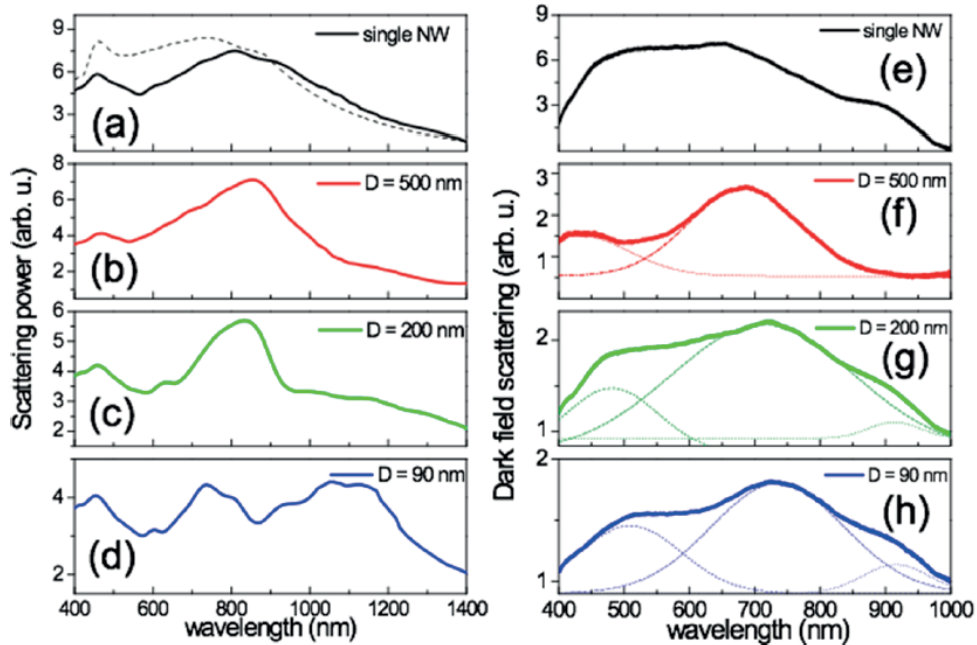


Figure 5.5: The left panel shows FDTD simulated scattering cross section for a single NW (a) and NW-nanoantennas coupled system with d of 500 nm (b), 200 nm (c), and 90 nm (d). In panel (a), dashed line is the scattering cross-section by the analytical Mie theory. In the right panel, correspondent experimentally measured dark-field scattering (e), (f), (g) and (h). Dashed line in panel (a) is the analytical calculation of the Mie scattering resonances in an isolated wire of infinite length. Dashed lines in panels (f-h) represent the deconvolution of the experimental spectra into Gaussian functions. Note that the x-scale is different for the numerical and experimental data. Copyright ©2014, American Chemical Society.

simulations. These could be originate by small variations in the diameter along the NW, by the presence of nanoscale sections of crystallographic phases[183], or surface states. However, the experimental scattering spectrum of the single NW qualitatively matches the theoretical one obtained by the Mie theory and the numerical results by the FDTD.

In Fig. 5.5 we also investigate the NW response in the presence of the plasmonic nanoantennas. In particular, by decreasing the antenna gap d we can gradually tune the electromagnetic response of a single NW and achieve strong near-field plasmon (i.e., quasi-static) coupling. Numerical calculations show additional bands appearing for the devices with nanoantennas. They are related to the resonances of the antenna array as well as the coupling behavior of the combined antenna/NW system. In particular, in Fig. 5.5b, a prominent peak emerges at around 850 nm for $d = 500$ nm, where the NW-nanoantenna coupling is weak. We refer to this situation as the *weak plasmonic coupling regime*. For the closest dimers separations, another peak at longer wavelengths clearly emerges. This trend is confirmed by the experimental data, where for $d = 500$ nm (Fig.5.5f) we observe only one peak, but for $d = 90$ nm (Fig.5.5g and Fig.5.5h) a broad band starts to appear in the infrared region. Due to the limited grating

efficiency of our setup in this spectral region, we can only appreciate the onset of this new peak in Fig. 5.5.

5.3.2 Near-field distribution

We performed 3D FDTD simulations in order to better understand the coupling behavior of the complex antenna/NW system. We calculate the spatial distribution of the electric near-field amplitude for the single NW and the different configurations of the coupled system. The FDTD electric near-field distributions calculated in the horizontal plane of the array are plotted in Fig. 5.6. *a* and *b* show the case of NW/antennas system with $d = 500 \text{ nm}$ at the peak of the calculated scattering ($\lambda = 850 \text{ nm}$). *c*, *d*, *e*, *f* and *g* show the case of $d = 90 \text{ nm}$ for $\lambda = 735 \text{ nm}$ and $\lambda = 1165 \text{ nm}$.

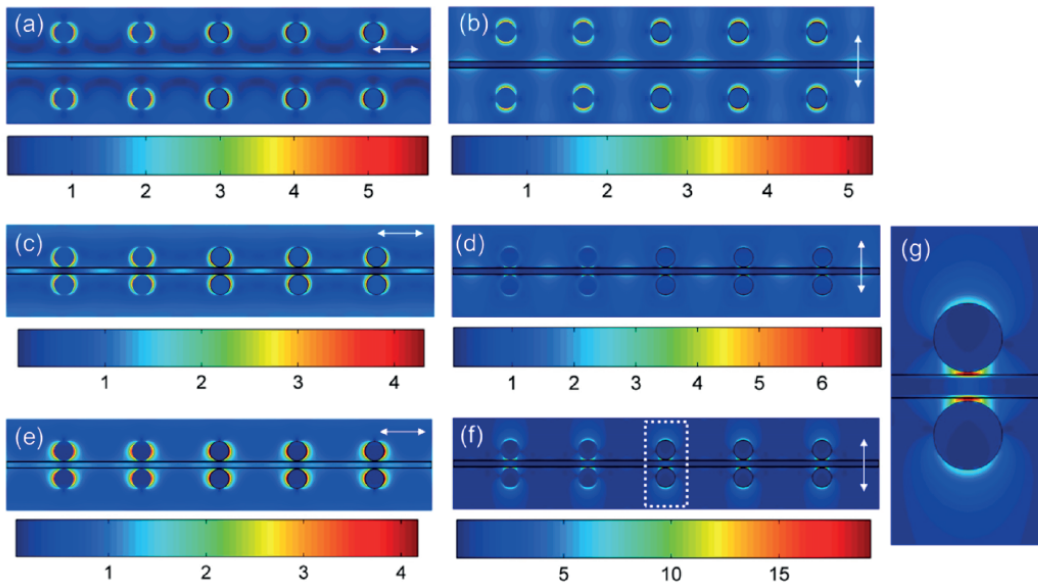


Figure 5.6: Calculated electric near-field distribution of the nanoantenna coupled NW systems plotted in the horizontal plane of the array (half-way up the cylinder in the z -direction). Electric field intensity for the longitudinal (a) and transverse (b) polarization with respect to the wire for $d = 500 \text{ nm}$ and $\lambda = 850 \text{ nm}$. In (c), (d), (e), (f) and (g) is represented the longitudinal and transverse near-field distribution for $d = 90 \text{ nm}$. In the case of (c) and (d) λ is 735 nm and for (e) and (f) λ is 1165 nm . The magnified region denoted by the dashed box in panel (f) is plotted in panel (g). Copyright ©2014, American Chemical Society.

The field is plotted for (a,c,e) longitudinal and (b,d,f,g) transverse polarizations with respect to the NW, as indicated in the figure by the white arrows. The coupling with the incident light is very polarization sensitive due to the particular geometry of the NWs, several microns long in one direction and with diameter of sub-wavelengths dimension. In high aspect ratio NWs the longitudinal polarization is always more efficient than the transverse polarization in

5.3. Photonic-plasmonic coupling of GaAs NWs with disk nanoantennas

establishing the internal EM field. The smallest is the NW diameter the largest is the anisotropy in the absorption behavior [184, 185]. For the weak plasmonic coupling regime (Fig. 5.6a and 5.6b), the nanoantennas have only a small influence on the NW response for both longitudinal and transverse polarizations. In addition, the EM field is concentrated into the NW only in the case of longitudinal polarization. In this regime the nanoantennas are too separated from the NWs to alter significantly their polarization sensitive optical behavior. A weak field modulation due to the nanoantennas can be appreciated in the NW region in between the two metal disks. In these spatial regions the field is less intense. This effect becomes stronger in the case of the strong plasmonic coupling regime (Figs. 5.6c,d,e,f).

Figure 5.6(c,d) plots the near-field distribution for the device with $d = 90 \text{ nm}$ excited with longitudinal and perpendicular light at $\lambda = 735 \text{ nm}$. Here the nanoantennas clearly couple to the NW for both polarizations. In the longitudinal polarization the plasmonic antennas locally decrease the electric field intensity in the NW. This interference behavior leads to a confinement of the electric field between one dimer and the other (Fig. 5.6c). On the other hand, for the transverse polarization, the field is strongly localized by the nanoantennas into their feed-gap regions. In the case of longer wavelength, $\lambda = 1150 \text{ nm}$, the near-field distribution for transverse polarization has a maximum peak that corresponds to an enhancement of the electric field intensity of approximately 20 times compared to the incident one (Fig. 5.6(f,g)). The coupling here is very strong and the electric field, usually confined outside the NW surface for this polarization, begins to penetrate into the NWs (Fig. 5.6g). This enhancement of the electric field inside the NW is confirmed also by second harmonic measurements later discussed in the thesis.

We calculated the cross-sectional (z-y plane) electric field distribution along the dimer axis to further investigate the electric field enhancement in the NW due to incident light with both transverse and longitudinal polarizations. Figure 5.7a shows the maximum electric field value (black) and the spatially-averaged electric field (red) calculated inside the NW region as a function of the incident wavelength. Fig. 5.7b,c and d show the relative electric field of an isolated dimer antenna with $d = 90 \text{ nm}$, for the coupled NW/antennas system with $d = 500 \text{ nm}$ and with $d = 90 \text{ nm}$. In the case of isolated NW the electric field intensity inside is very low for all wavelengths, around 0.5 of the incident light intensity. In Fig. 5.7b the dimer antenna shows a plasmonic resonance and it concentrates the electric field within its small feed-gap region. In the cross sectional plane analyzed, the nanoantennas are contributing to enhance only the electric field induced by the transverse polarized light as shown in Fig. 5.6. For the coupled system with $d = 500 \text{ nm}$ the NW and the nanoantennas show only weak coupling. On the other hand, for the coupled system with $d = 90 \text{ nm}$ the field peaks inside the NW at 1165 nm reaches an enhancement of 5.5 times (with respect to the incident field) close to the NW surface. The electric field spatial intensity profiles are also shown in the insets in figure 5.7 at 1165 nm . These results indicate that the designed nanostructures offer the possibility to tailor the electromagnetic coupling regime between NWs and nanoantennas. Moreover, we have shown that the dimer antennas can strongly concentrate in the NW the incident light with transverse polarization, which is normally only weakly absorbed. This

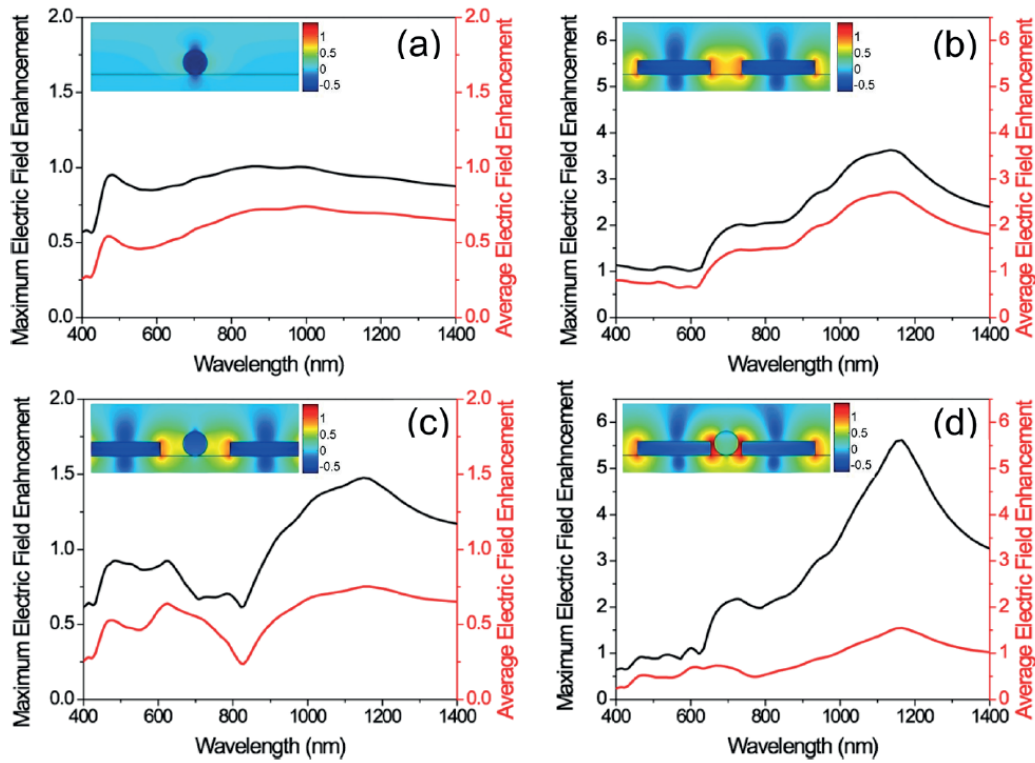


Figure 5.7: Cross-sectional average (red) and maximum (black) electric field enhancement values inside the region of the NW under incident light with both transverse and longitudinal polarization. The graphs refer to (a) isolated NW, (b) isolated dimer pair with $d = 90 \text{ nm}$, (c) antenna coupled NW with $d = 500 \text{ nm}$, and (c) antenna coupled NW with $d = 90 \text{ nm}$. Insets are electric field cross-sections, plotted at 1165 nm in log-scale for each configuration. Copyright ©2014, American Chemical Society.

offers the possibility to manipulate the NW polarization response by tuning the gaps of the nanoantennas. This new functionality can make these coupled systems ideal candidates for engineered nano-photodetectors and more efficient NW-based solar cells.

5.3.3 Second harmonic generation (SH-G)

The second harmonic spectra measured for the investigated samples are plotted in Figure 5.8. Figure 5.8a shows the spectrum of an isolated NW featuring a prominent peak localized at 880 nm . This correspond to the two-photon resonance of the E_1 inter-band transition in GaAs bulk material[186, 187]. In the spectral range analyzed no other resonances are observed. For the coupled NW-nanoantennas systems we note that some SH-G emissions could in principle be generated by the gold nanodisks[188, 189]. However we can neglect any contribution related to the gold nanodisk in our structure. Indeed by comparing the SH-G of an isolated NW (Fig. 5.8a) and the coupled system for $d = 500 \text{ nm}$ (Fig 5.8b), it becomes evident that the

5.3. Photonic-plasmonic coupling of GaAs NWs with disk nanoantennas

SH-G contribution of gold nanoantenna is negligible. In our system, the only role of metal nanoparticles is to change the distribution of the electric field in the nanowire.

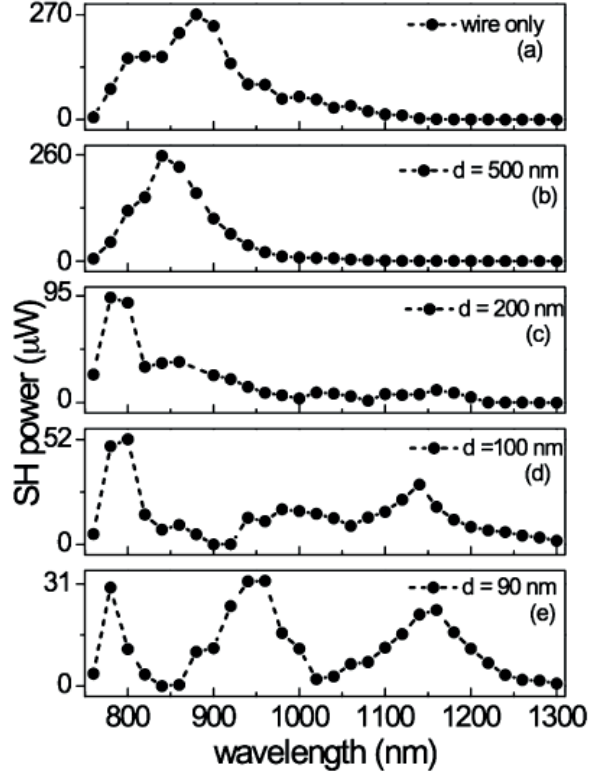


Figure 5.8: Experimentally measured second harmonic generation spectra from NW only and NW-coupled antennas with $d = 500 \text{ nm}$, $d = 200 \text{ nm}$, $d = 100 \text{ nm}$ and $d = 90 \text{ nm}$, as labeled in the figure. Copyright ©2014, American Chemical Society.

We consider the effect of the electric field localization due to the nanoantennas as based by two main contributions: one is related to transverse polarized light (perpendicular to the NW axis), and the other to the longitudinal polarized light (parallel to the NW axis). Due to the large aspect ratio, an isolated NW of sub-wavelength diameter is efficiently excited only for the longitudinal polarization[97]. This topic will be also further discussed in the next chapter. The nanoantennas investigated in this thesis are focusing the transverse polarized light into the NW and on its surface. As shown in the simulation in Fig. 5.7d, at 1165 nm we observe a maximum field enhancement of 5.5 at the NW surface. At this wavelength, for small nanoantennas feed-gap distances, novel SH-G peaks appear. The measured intensity at this wavelength scales with the gap d as follow: $I_{Single_{NW}} = 0.8 \mu W$, $I_{d=500} = 0.3 \mu W$, $I_{d=200} = 11 \mu W$, $I_{d=100} = 19 \mu W$ and $I_{d=90} = 23 \mu W$. In order to estimate the electric field enhancement measured by SH-G, we assume that the second harmonic intensity scales like E^4 , where E is the maximum value of the electric field on the wire. We compare the isolated NW and the coupled system for $d = 90 \text{ nm}$ and we estimate a maximum enhancement of 2.3, which is in

qualitative agreement with the simulation data shown in Fig. 5.7. In Fig. 5.8e another peak at 950 nm is observed. However, the intensity of the peak does not scale as predicted. We think that it is possibly due to small deviations from the ideal system geometry. These small perturbations in the system become more significant when the distance between the NW and the nanoantennas is of the order of few nanometers.

The SH-G peak at 880 nm that appears for the isolated NW (Fig. 5.8a) is related to the excitation of the transverse polarized light. By adding nanoantennas in the system, we observe a reduction in the intensity of the peak. In principle, the absorption of longitudinal polarized light is reduced due to the perturbing effect of the gold nanoantennas on the local field distribution along the nanowire (see Fig. 5.6c). Indeed, we notice that the distance between two nanoantennas along the NW is 840 nm which corresponds to the wavelength of maximum drop in the SH-G intensity (from $162\text{ }\mu\text{W}$ in the isolated NW to $0.01\text{ }\mu\text{W}$ in the coupled system with $d = 90\text{ nm}$). Our experimental data demonstrate that the distance between nanoantennas along the NW also plays a significant role in the overall local field distribution and the resulting SH-G intensity in the coupled system. This provides an additional degree of freedom that needs to be taken into account. In the next chapter a deep investigation of d is performed on bow-tie nanoantennas. This study is intended to bring more light into the design of such complex nanosystems which could be useful for solar cells and photodetectors applications.

5.4 Controlling the directional emission of GaAs NWs with Yagi-Uda antennas

In addition to the coupling of incident light in nanostructures, in the past decade, many efforts have been done to enhance the photoluminescence and modify the directional emission of quantum emitters including quantum dots and fluorescent molecules [190, 191, 161]. Yagi-Uda optical antenna is one of the remarkable systems showing pronounced directionality [192, 193]. The dielectric function of noble metals including Au, Ag and Al causes the plasmonic resonances occurring in the visible range of electromagnetic spectrum and leads to a strong enhancement of spontaneous emission rate of the feed element. Subsequently, the scattering of the feed emission with the antenna elements and the interference of scattered radiation in the far-field lead to a strong directional emission, that can be controlled with the Yagi Uda antenna geometry.

In this and the next paragraphs, we show how replacing the resonant metallic feed element of Yagi-Uda antenna by a non-resonant semiconductor nanowire we obtain a strong directional emission. The measurements have been done on GaAs nanowires using Fourier microscope. To demonstrate the strong dependence of the emission with the length pa-

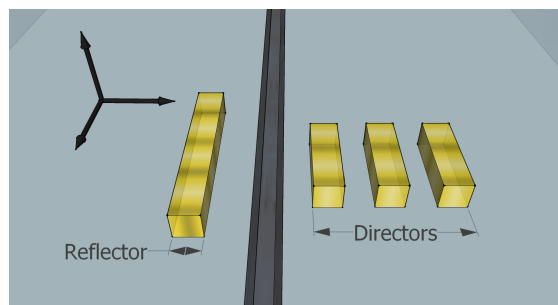


Figure 5.9: Schematic of nanowire/Yagi-Uda antennas system.

rameters, we have fabricated two antennas with different dimensions to direct the emission in opposite directions. The mechanism leading to the directional emission is studied by means of the Finite-difference Time-Domain (FDTD) method and the experimental radiation patterns were verified by simulations of the far-field radiation patterns. The schematic representation of the nanowire-Yagi-Uda hybrid system is represented in Figure 5.9.

5.5 Results and discussions on NW/Yagi-Uda systems

5.5.1 Fourier spectroscopy microscope

A Fourier microscope consists of an objective lens that focuses on the sample. Scattered light or photoluminescence from the sample is collected by the objective. The operation of the lens is like a Fourier transformer. It decomposes the waves to plane waves with defined k -vectors, focusing them on the back focal plane of the lens. Each point on the back focal plane corresponds to one k -vector in direction of emission. This directionality can be recorded with CCD camera placed on the back focal plane of the objective. An interesting feature of the Fourier microscopy is its *shift invariance property*. Since the Fourier pattern is dependent on the direction of the signal coming toward the lens, the lens should not be focused precisely on the emitter and it gives relatively high depth of focus to the microscope.

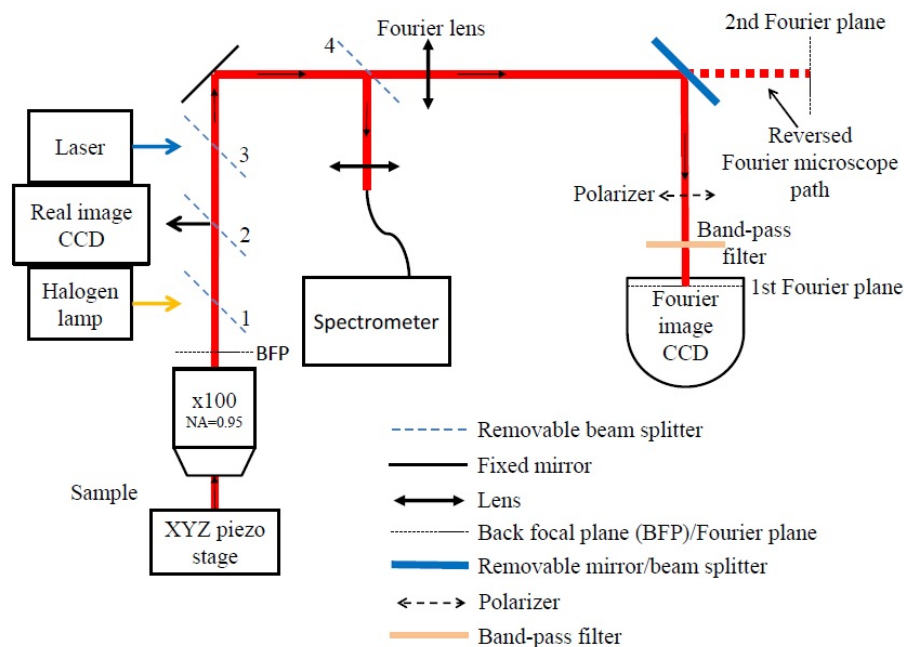


Figure 5.10: Fourier microscope setup scheme. From [194].

One crucial aspect in the Fourier microscope is angular acceptance of the objective lens. To get the most of the information we need to collect light in the largest possible range of angles. To achieve it, we need to use the objective lens with a high numerical aperture. In our experiment, the nanowire is excited with a focused beam from a CW laser diode ($\lambda = 785 \text{ nm}$) and we used 0.95 N.A. , which allows to collect the light up to 72° with respect to the normal to the sample. In the schematic representation of Figure 5.10, the experimental realization of the Fourier microscope setup is shown.

5.5.2 Fourier spectroscopy measurements

The Fourier emission of a single NW exhibits circular symmetry with the intensity perpendicular to the surface. This behavior is typical of the leaky mode emission in small diameter nanowires where guided modes are not allowed [195]. On the other hand, when the nanowire is coupled with Yagi-Uda antennas the directionality becomes strong. Two plasmonic antennas with different geometrical parameters were fabricated. The SEM picture of the fabricated antennas with the reflector length of 175 nm and 300 nm are shown in Figure 5.11a and 5.11d, respectively. The reflectors of the two antennas have different lengths, hence, we call the antenna with the length 175 nm as YU175 and the one with 300 nm reflector is YU300.

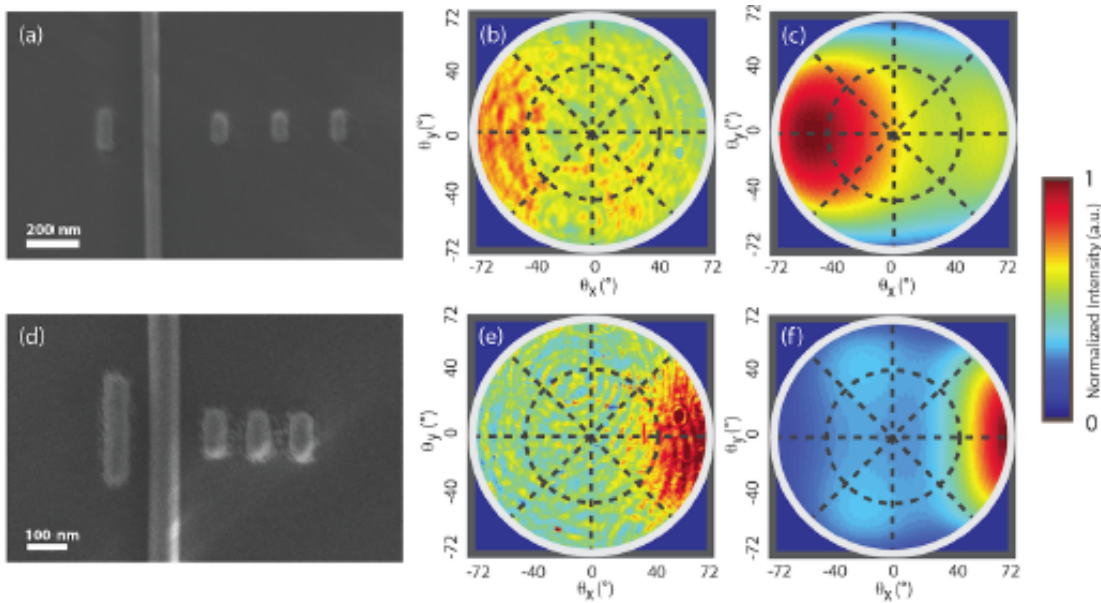


Figure 5.11: a) SEM images of YU175 with the reflector length of 175 nm . b) Corresponding radiation pattern measurement. Most of the radiation is directed toward the reflector (left) and c) simulation of the radiation pattern. d), e) and f) represent respectively the SEM, the radiation pattern and the radiation pattern simulations of YU300 with reflector length of 300 nm . In this second case the large part of the emission of the nanowire is directed toward the directors (right). Reprinted with permission from [196] copyright ©2015, American Chemical Society.

Figure 5.11b shows the measurement of the radiation pattern in YU175. The directionality of the antenna emission is toward the reflector element ($-K_x$), which is in opposite with respect to the usual Yagi-Uda behavior. Moreover, weak directionality and beaming are obtained by this device. By increasing the length of the reflector element to 300 nm in the YU300 antenna, the direction of the radiation pattern changes substantially to the right side along $+K_x$ direction (Forward). The simulation of the radiation patterns (Fig: 5.11c and 5.11f) are implemented by Finite-Difference Time-Domain method using Lumerical's FDTD Solution. The GaAs nanowire with the length of 6 μm and the diameter of 70 nm is placed horizontally on top of a silica substrate. On top of the substrate, air ($n = 1$) is considered as the surrounding medium. The optical constants were extracted from [182]. An oscillating electrical dipole along the long axis of the nanowire is considered as the emission source.

One criterion in the assessment of the antenna performance is the Front to Back ratio (F/B). This factor is defined as the ratio between maximum intensity point along the radiation direction to the intensity of the identical point on the opposite side. The F/B ratio for YU300 (YU175) is 4 (1.72) in the calculated radiation patterns and 1.78 (1.6) in the experiments. The difference between the experimental and theoretical F/B values can be attributed to the background intensity originating from the excitation of the nanowire in the far-field radiation pattern. As discussed earlier, to simulate the radiation pattern of the devices, a single electrical dipole is placed in the middle of the nanowire, oriented along its long axis. As a result, a local excitation of the emission is considered. However, in experiment, the nanowire is excited by the diffraction limit laser spot with diameter around 785 nm. This method of illumination excites some regions of the nanowire relatively (around 300 nm) far from the Yagi-Uda antenna and introduces a background intensity in directional emission measurement.

The change in directionality between the two Yagi-Uda systems is attributed to the the phase difference between the reflector and directors. The necessary condition to have strong directionality relies in having an anti-phase conditions between the reflector and the first Yagi-Uda director. This is achieved for YU300, while only weak directionality is observed in YU175 where reflector and first director are in phase resonance [196].

5.6 Conclusions

In conclusion, we demonstrated photonic-plasmonic resonances of Au nanoantennas coupled to a GaAs NW in a controlled and reproducible way. We used dark-field scattering and SH-G spectroscopy in partnership with analytical and full-vector FDTD modeling to demonstrate electromagnetic coupling between arrays of nanoantennas and individual NWs and the NW near-field enhancement. We analyzed the system ability to tailor the nonlinear optical response of individual GaAs NWs by engineering near-field coupling regime. These findings represent an initial and very promising step towards the development of novel metal-semiconductor resonant nanostructures. These hybrid systems leverage the plasmonic properties of metallic nanoantennas and the semiconductor NWs technology for the realization of

high-efficiency solar cells, high resolution nanodetectors and nonlinear optical devices.

We have also shown a strong directionality in the emission by measuring the radiation pattern of the Yagi-Uda antenna fabricated around a nanowire. We experimentally demonstrated that the directionality can be modified by the geometrical parameters of the antenna. FDTD simulations of the antennas shows an excellent agreement with the experimental data. The obtained results can be applied to design and fabricate electrically driven optical antennas based on semiconductor nanowires.

6 Nanoantennas to control the nanowire polarization response

One of the major challenges for NW full technological deployment, is their strong polarization dependence in light absorption and emission. In the past, metal nanostructures have been shown to have the ability to modify their light response. Today optical nanoantennas are used to enhance the absorption and modify the polarization response of the system.

This chapter is addressed to enhance and optimize the absorption of a NW. To achieve this we embed the NW in a bow-tie nanoantennas array. In the first part, the photonic properties of NWs are illustrated. Particular attention is devoted on the analysis of resonant modes and on the effects of the NW cross section and substrate. The bow-tie nanoantennas geometry is designed around the NW using COMSOL Multiphysics in order to engineer a platform for the NW absorption enhancement. The more significant parameters are used in the realization of the physical devices and photoconductivity measurements have been performed. Measurements and calculation show the possibility to enhance the NW absorption as well as invert its polarization response. Finally, the photocurrent scanning map on the NW/nanoantennas system is shown. Although the scanning resolution is of the order of $1\ \mu\text{m}$, we can observe the effect of the local field enhancement produced by the nanoantennas array.

Publication:

A. Casadei, E. Alarcon-Llado, F. Amaduzzi, E. Russo, D. Ruffer, M. Heiss, L. Dal Negro and A. Fontcuberta i Morral *Polaritation response of nanowires à la carte*, Scientific Reports, 5, 7651 (2015);

6.1 Introduction

NWs exhibit a highly anisotropic polarization response both in light absorption and emission: light absorption occurs preferentially for light polarization along the NW axis, with some dependence on the diameter [97, 184]. This means that a NW responds mostly to light polarized along its axis, and it is almost transparent for light polarized perpendicular to the NW axis. Thus, almost half of all incoming light passes through a NW without effectively interacting. This anisotropy limits the use of NWs in some photonic applications, such as photodetectors and solar cells [123]. Recent works have shown that the combination of semiconductor NWs and metal nanoparticles can enhance and localize the light absorption [175, 197, 198, 158, 161, 199]. In particular, the results achieved in the previous chapter of this thesis, have shown the optical coupling between disk-shaped nanoantennas and NWs [200]. Some evidence of polarization dependent response have been reported by the use of second harmonic generation. In this case, the electric field enhancement was only observed in the infrared region and therefore the design was not suitable for photovoltaic purposes. Another recent work on carbon nanotubes [201], shown an increase of Raman scattering in presence of disk nanoantennas, but all these previous studies did not involve any deliberate engineering of the absorption spectra or absorption rate.

In this work, we design a plasmonic antenna to directly counteract the characteristic anisotropic polarization response of GaAs NWs. We also carefully engineer the system in order to not diminish the absorption rate of light polarized along the NW. We modified the NW polarization response up to the point of inversion and we enhanced the NW absorption in the visible spectrum. We also calculated a NW absorption enhancement up to 15 times in the infrared region. This design principle is not restricted to the materials and wavelengths under study; these principles can be extended to other materials and other regions of the electromagnetic spectrum. This platform benefits of the large parameter space for light absorption design and the special opto-electrical properties of GaAs, such as a direct band-gap in the visible range, high absorption coefficient and high charge mobility. This imply a very high potential for a multitude of nano-optoelectronic devices.

6.2 NW photonics

A very attractive feature of NWs is that small structural changes can lead to dramatic changes in their optical properties. As a result, NWs allow for modulation of optical properties and thus enable efficient photonic devices. Different studies have shown that semiconductor NWs can function as photonic waveguides [168, 179, 202]. They can also act as ultra-small optoelectronic components in integrated circuits or nanolaser [203, 204]. In addition, NW photovoltaic devices exhibit enhanced light absorption compared to conventional planar devices due to highly confined resonant modes and large absorption cross section [170, 16]. As a result of resonant modes, they have the ability to selectively tune several or selected resonant modes through morphological changes.

Light absorption in NWs is described by several parameters: (i) the absorption coefficient, (ii) the coupling efficiency between incident light and a NW, (iii) the spatial profile of resonant modes, and (iv) the NW size-dependent optical antenna effect, which means that a NW can interact with incident photons beyond its projected area. All these parameters together compete to an overall enhancement in the absorption efficiency.

6.2.1 Resonant modes

In this work particular attention is given to engineer the electric field in the NW upon illumination. The generated photocurrent, which is the driving property of opto-electronic devices, is proportional to the square of the local electric field. In contrast to a bulk structure, in a NW it is less straightforward to predict the wavelength-dependent absorption, because of its optical antenna effect and localized resonant modes. The optical antenna effect from a NW cavity is one of the primary determinants of the absorption efficiency. These effects are maximized at each resonance and they are enhanced with decreasing NW size [184]. Another important factor affecting the absorption efficiency of a NW is the presence of localized resonant modes. Since a NW can be regarded as a waveguide with a high refractive index, resonant modes in a NW cavity can be identified using standard nomenclature (l, m) and according to their polarization states, transverse electric (TE) or transverse magnetic (TM). In order to couple effectively to resonant modes of a cavity, incident photons must satisfy stringent conditions including momentum matching as well as frequency matching. For this reason, it is important to note that not all calculated modes will necessarily appear in a measured absorption spectrum. Figure 6.1 shows the absorption spectra (normalized on the NW volume and in function of its diameter) of a single GaAs NW laying on a glass substrate under light polarized perpendicularly to the NW axis. In general we can make the following considerations: (i) The number of peaks in the absorption spectrum increases with the NW size; (ii) in a larger NW, all the absorption peaks are red-shifted, while the mode profiles corresponding to those peaks is preserved [98], and (iii) the maximum external quantum efficiency (EQE) amplitude for the larger NW is decreased as compared to the smaller NW owing to a reduced optical antenna effect [205].

6.2.2 Cross-section and substrate dependence

The aspect ratio and cross-sectional shape of a NW influence the type of resonance modes. In particular if a NW is composed of highly absorptive material, the short attenuation depth of photons will reduce optical feedback within the cavity leading to weak excitation of resonant modes [170]. This is the case shown by Cao *et al.* in figure 6.2a, 6.2b and 6.2c, where the amorphous Si NWs with different cross sections do not exhibit distinct absorption features in current densities, absorption spectrum, or resonant mode profile. The difference in current density results only in different cross sectional areas. On the other hand, if the NW is composed by less absorptive material, the attenuation depth become larger than the NW size allowing the excitation of defined resonant modes. In this last scenario, the cross sectional shape strongly

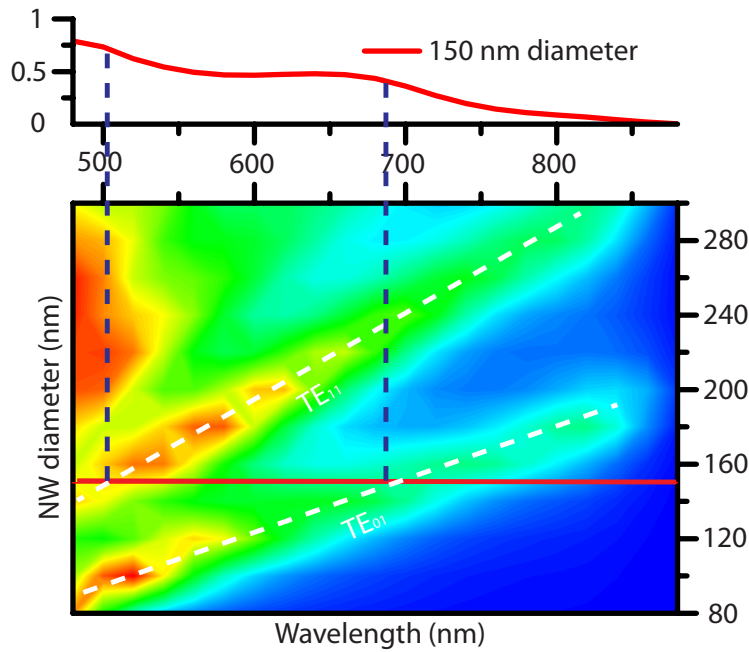


Figure 6.1: Calculated absorption efficiency map of a NW laying on a glass substrate under transverse polarized incident light. The white dots lines are guide to the eyes to indicate the NW modes TE_{01} and TE_{11} . The absorption profile is taken for a NW with diameter of 150 nm and the blue dots line show the guided modes position.

influence the NW optical properties [206].

Previous papers have indicated that the introduction of an appropriately designed substrate can increase the NW absorption efficiency [207, 208]. In general, the substrate effect is more pronounced for a NW than a thin film because of its good resonator properties. The substrate enhances the amplitude of all cavity modes and in particular, the NW absorption efficiency increases dramatically when it is positioned on metal substrate. In figure 6.2d the substrate effects on the NW absorption is evaluated. The internal quantum efficiency (IQE) of a device corresponds to the efficiency of light conversion once the light has been absorbed in the device. The external quantum efficiency (EQE) refers to the one measured with respect to the incident light. In planar solar cells, an anti-reflecting treatment is incorporated so that the ratio EQE/IQE can be as close as 1 as possible. Heiss *et al.* in 2011 shown that the ratio EQE/IQE, for GaAs NWs with diameter of 80 nm on ideally reflective substrate, reach 1.1. For this conditions the NW will absorb more photons than what are geometrically incident to its projected surface area.

Reflection losses can also be reduced by introducing a dielectric shell layer. The dielectric coating assists photons trapping and reduces backscattering losses [209]. Essentially, a dielectric shell on a NW increases the probability for photons to couple to the cavity leading to an enhancement of current density.

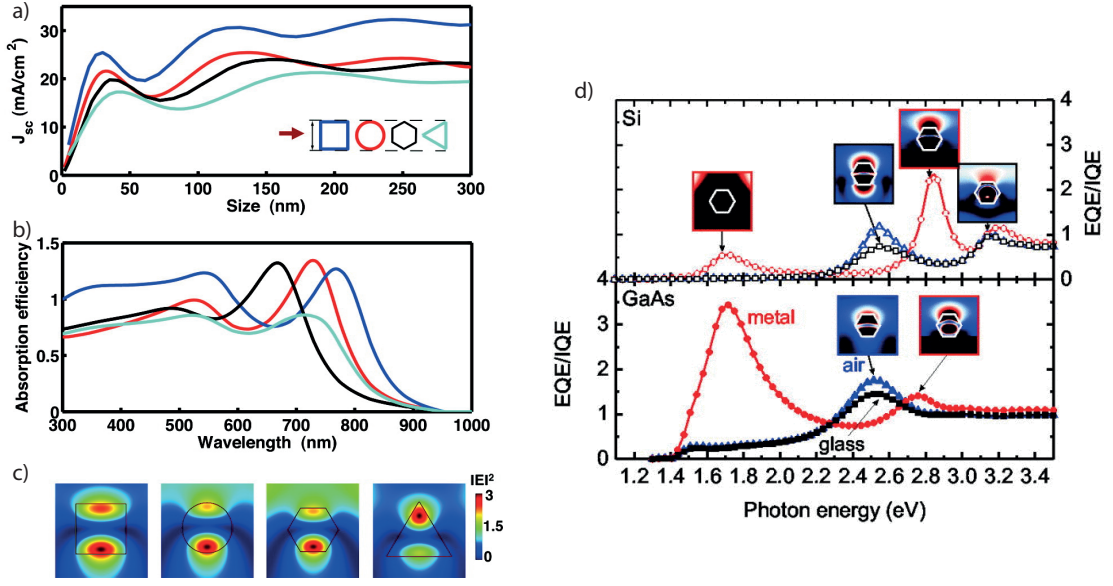


Figure 6.2: a) Simulated short-circuit photocurrent density J_{sc} for one-dimensional amorphous Si structures of circular, rectangular, hexagonal, and triangular cross section as a function of size. The inset schematic illustrates the way to compare the size for different structures, and the red arrow indicates the illumination geometry used in the calculations. b) Simulated absorption spectra of these one-dimensional amorphous Si structures in a size lying in the regime that corresponds to their second enhancement peaks shown in (a). Specifically, the size is 180 nm for the triangular NW and 130 nm for all other structures. c) Calculated electric field distribution (normalized to the incidence) of these structures upon the resonance corresponding to the absorption peak at $\approx 700\text{ nm}$ in (b). d) Ratio of external quantum efficiency to internal quantum efficiency (EQE/IQE) in dependence of photon energy for cases of NW in air (triangles), on glass substrate (squares) and on an ideally reflecting metal surface (circles). The open symbols correspond to crystalline silicon NWs while the filled symbols correspond to crystalline GaAs. The data shown corresponds to incident light polarized parallel to the NW axis and a wire diameter of 80 nm . The inset shows the calculated electric field energy distribution for selected data points indicated by the arrows. a), b) and c) adapted from [170], Copyright ©2010, American Chemical Society; and d) adapted from [208], Rights managed by AIP Publishing LLC.

6.3 Geometry optimization of the nanoantennas

The interaction of incident light on the NW/nanoantennas system is calculated with COMSOL Multiphysics by using the electromagnetic waves module and the frequency domain study based on Maxwell's equations. In particular we solve the following equation for the three spatial dimensions:

$$\nabla \times \mu_r^{-1} (\nabla \times E) - k_0^2 \left(e_r - \frac{j \cdot \sigma}{w \cdot e_0} \right) E = 0 \quad (6.1)$$

where $\mu_r = 1$ (for all materials) is the magnetic permittivity, E is the electric field, k_0 is the wave-vector, e_r and e_0 are the relative and absolute permittivity and $\sigma = \sigma_s + w \cdot e_0 \cdot e_{imm}$ is the electrical conductivity. σ_s is the static conductivity, it is negligible for GaAs, glass and air and it is $\sigma_s = 4 \cdot 10^7 S/m$ in the case of gold. $e_r = (n - i \cdot k)^2$, where n and k are the dielectric real and imaginary part of the material and for gold and GaAs these values are delivered from Palik[182]. Although the NWs have a 40 nm doped shell with a concentration of $2.2 \times 10^{18} atoms/cm^3$, the doping is only affecting the NW optical properties for wavelengths very close to the band-gap[210]. Since in our work we are not interested in this particular task we consider the doping effect negligible on the NW optical properties. Plane wave excitation is perpendicularly incident on the NW-nanoantennas system, made of a hexagonal cross section NW and bow-tie nanoantennas. The nanoantennas are designed with a rounded shaped edges with 15 nm radius in order to better simulate the real device. Periodic continuity conditions are introduced on the surfaces that limit the NW length in order to obtain an infinitely long NW/nanoantennas array and the boundary conditions $E_x = E_y = E_z = 0$ are set along the other external simulation surfaces. A free tetrahedral mesh is used for all the domains with size below 20 nm in the NW and respectively larger sizes for nanoantennas, substrate and surrounding air.

Figure 6.3a shows the range of geometrical parameters investigated in the calculations. Figure 6.3b) reports the energy density in a single NW and a device NW/nanotennas in function of the NW diameter. For very small diameters ($< 40 nm$) the nanoantennas enhance the energy density by more than 26 times. Despite the large energy density enhancement, GaAs NWs with small diameter are not optimal candidates for the investigation of opto-electrical properties. The presence of surface states generates a depletion region that completely inhibits the electrical transport. On the other hand for big diameters ($> 250 nm$) the distance between the two nanoantenna sides becomes very large, breaking the nanoantennas resonances and leading to an inefficient coupling. For 150 nm in diameter we have the higher electric field energy density and we then use this value for the device fabrication. Fig. 6.3c and 6.3d show how the energy density changes in function of the nanoantennas size and thickness and the dimensions selected for the devices fabrication are represented by the blue dashed lines. Also in these cases the parameters chosen for the device realization are selected to maximize the absorption.

The nanoantenna distance d is directly linked to their density along the NW. For small distances ($d = 400 nm$) the density is high, and therefore we expect the largest effects on the NW absorption. We calculated the field energy density in the NW for the distance of 400 nm and we find the largest absorption for transverse polarized light at $\lambda = 680 nm$. Here we notice that the total nanoantenna dimension along its axis is around 680 nm and only transverse polarized wavelengths above this dimension can activate the antenna dimer and efficiently enhance the NW absorption. For λ below 680 nm the nanoantennas produce a small reduction in the calculated absorption of the system, while for $\lambda > 680 nm$ the absorption enhancement is extended to the infrared with some dependence on the nanoantennas density. As a general rule, in order to enhance the absorption for smaller wavelengths, nanoantennas with smaller

6.3. Geometry optimization of the nanoantennas

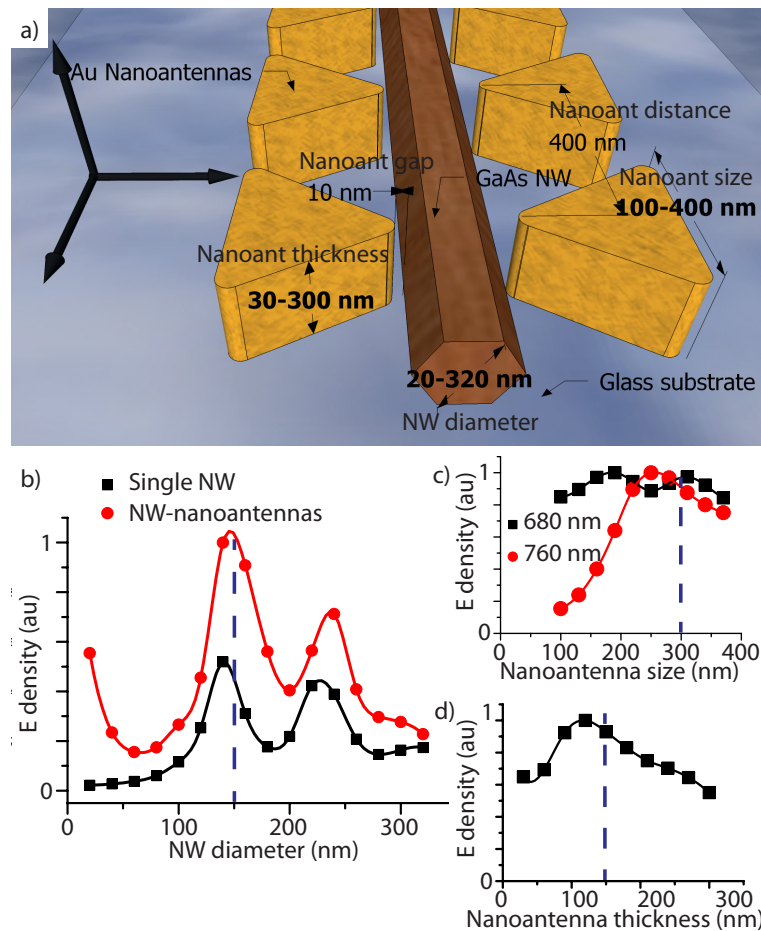


Figure 6.3: a) NW-nanoantennas geometry scheme. In bold are represented the range of parameters we investigate in the simulations b),c) and d). Simulations show the electric field energy density inside the NW for transverse polarized incident light with $\lambda = 680 \text{ nm}$ in function of NW diameter (b), nanoantennas size (c) and nanoantennas thickness (d). The effect of the nanoantennas size (c) is also shown for $\lambda = 760 \text{ nm}$. The blue dot lines indicate the parameter chosen for the realization of the devices.

dimensions need to be designed.

The absorption efficiency maps (fig. 6.4a - 6.4b) show the perfect dipole nanoantennas behavior. Bow-tie nanoantennas actively couple the incident light into the NW only when the light polarization is along the nanoantennas dimer axis and they do not interfere in the NW absorption of the light polarized in the perpendicular direction. In fact they are totally inactive for longitudinal polarized light leaving unaltered the NW absorption but they are efficiently coupling into the NW the transverse polarized light. The profile curves on top show the absorption spectra for the system $d = 400 \text{ nm}$ and $d = 1000 \text{ nm}$, corresponding to the dimensions used for the device fabrication. Finally we notice that the absorption efficiency profiles for $d = 1000 \text{ nm}$ and transverse polarized light is perfectly homogeneous between 550 and 750

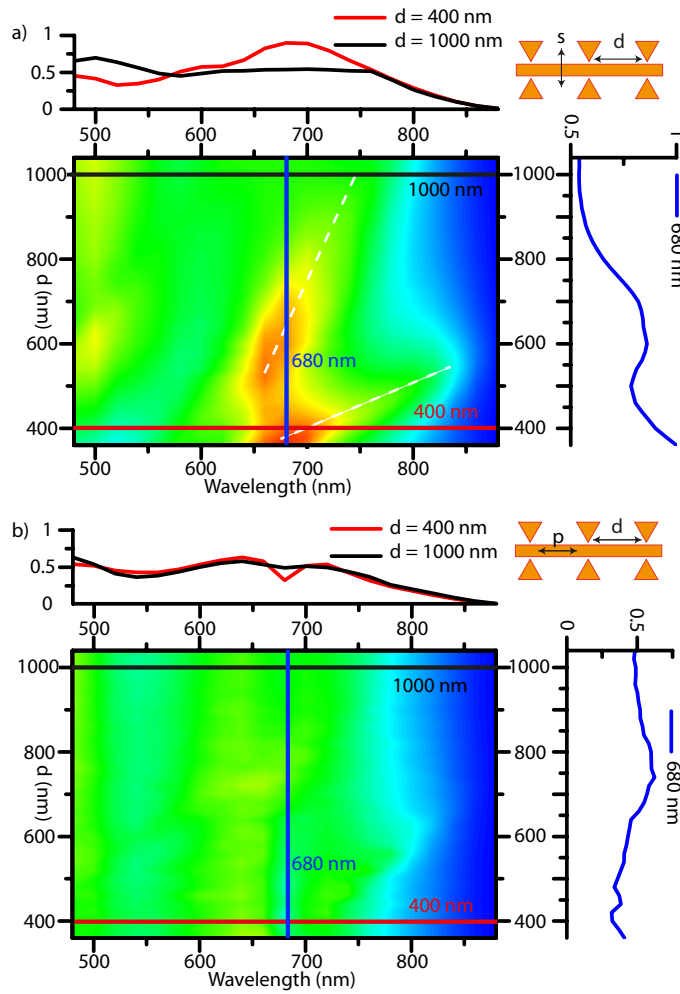


Figure 6.4: Calculated absorption efficiency map for a NW/nanoantennas system on a glass substrate as a function of the nanoantenna distance d (represented in the insets) for s-polarization (a) and p-polarization (b). The intensity profiles are taken at 680 nm wavelength and for $d = 400$ and 1000 nm. The dashed lines are used as a guide to the eye in the identification of the guided modes.

nm wavelength.

6.4 Absorption in the hybrid system

The proposed system is presented schematically in Fig. 6.5a. In order to engineering the NW spectra and polarization response we embedded a NW in a bow-tie antenna array . The nanoantenna dimensions are chosen in the previous paragraphs to maximize the electric field inside the NW. The nanoantennas height and width are set at 150 and 300 nm respectively. These values optimization are linked to the NW diameter (150 nm) and they are designed to

optimize the absorption of incident transverse polarized light. In addition, for the bow-tie antennas to modify the light interaction with the NW, they need to be positioned as close as possible to the NW [200]. In our case, the nanoantenna/NW gap is as small as 10 nm, which corresponds to the finest fabrication precision available for us. Fig. 6.5b shows an example of a fabricated device. We embedded a GaAs NW with a diameter between 140 and 146 nm in a dense bow-tie antenna array and we electrically contacted it to allow photoconductance measurements. In order to ensure ohmic contacts, a highly p-doped 40 ($2 \times 10^{18} \text{ cm}^{-3}$) nm shell was added [51] using carbon as dopant. NWs present mainly zinc blende crystal structure with few twins per μm and a small tapering leading to around 10 nm of difference between the top and bottom diameter. The devices were prepared by transferring NWs to a fused silica substrate. Their position was localized by using an optical microscope and the pre-patterned substrate. A glass substrate is preferable over an oxidized silicon wafer because it reduces possible light interference effects [99]. A different substrate would influence the overall shape of the response, though the bow-tie antennas would continue to enhance the NW polarization. We designed the nanoantennas around the NWs using a custom-made fitting software. The pattern encodes the relative position on the wafer and circular shapes recognition is used for nanoscale alignment. The position is determined via shape recognition algorithms leading to an accuracy between 10 and 50 nm. We used electron beam lithography (Vistec EBPG5000) to position the nanoantennas along the NW axis in close proximity to its surface. Before the exposure, a MMA and PMMA resist layer were spin coated on the substrate and the evaporation of 40 nm of Cr was needed in order to dissipate the electron charges. The Cr was then etched away and we evaporated 5 nm of Ti and 150 nm of Au after the developing of the resist. The electrical contacts consist of Pd/Ti/Au (40/10/200 nm) metal layer in contact with the NW doped shell leading [58].

For light polarized along the bow-tie axis, the antennas provide a strong energy confinement in their gap [211]. By positioning a dielectric NW in the gap, the antenna resonances result in an increase of energy field in the NW. In order to show this, we calculated the corresponding light absorption and field energy distribution in a single NW, in bow-tie antenna arrays and in a hybrid NW/bow-tie antenna system. These results are shown in 6.6.

The normalized calculated absorption spectra of a GaAs NW with a diameter of 150 nm and hexagonal cross-section for light perpendicular to the NW axis is shown in Fig. 6.6a. The absorption tends to decrease for longer wavelengths and we identify two absorption peaks at 500 and 680 nm. These peaks correspond to photonic resonances in the NW and have been studied extensively in the literature [98, 212]. Figure 6.6b depicts the light intensity within the NW cross-section in these resonant cases. Because the NW acts as a cavity, we obtain an absorption enhancement with respect to an equivalently thick film. The field energy distribution profile and the in plane electric field lines indicate the presence of the TE_{01} and TE_{11} coupled modes [213]. Figure 6.6c corresponds to the field energy calculations of the bow-tie antenna arrays. On the vertical axis we change the system geometry by varying inter-antenna distance. The electric field intensity is integrated on the volume corresponding to the NW in the NW/nanoantennas system in order to represent the capacity of the antennas

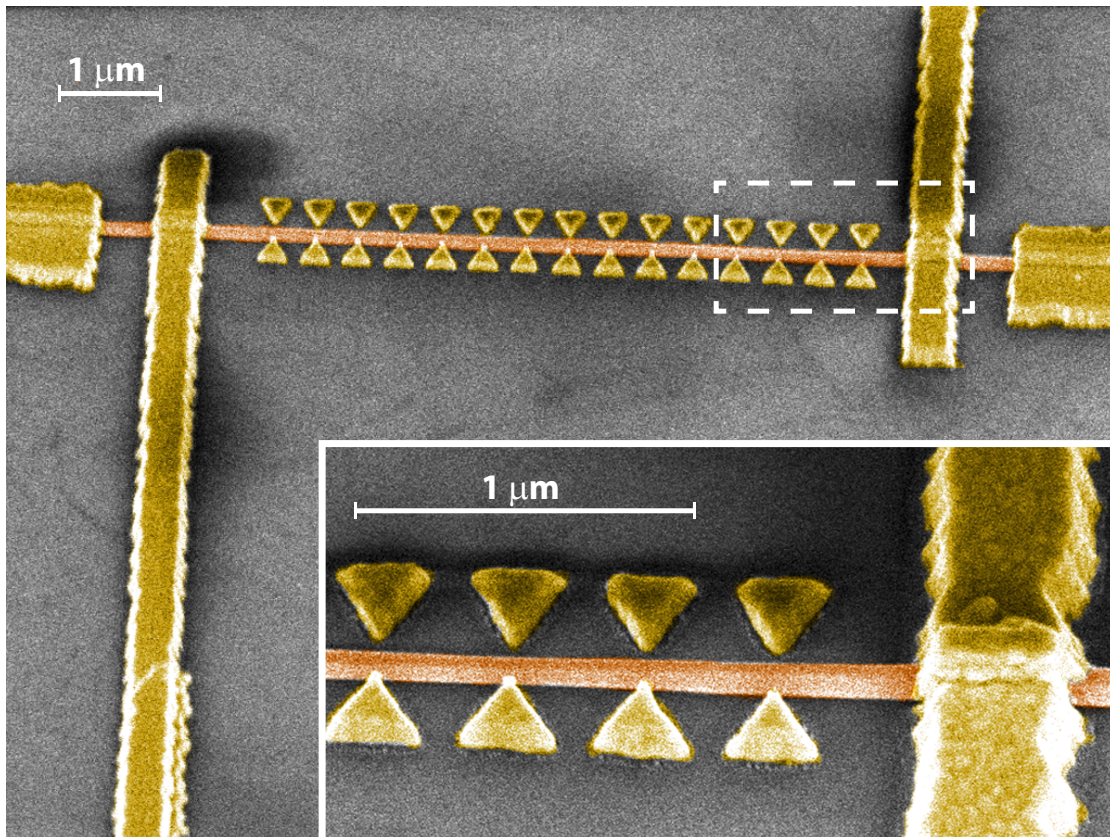


Figure 6.5: a) Scheme of the NW-nanoantenna system. The different colors in the NW are an illustrative representation of the field energy distribution inside the NW during the excitation of transverse polarized light. The red color indicates the highest field energy density and the green the lowest. b) SEM image of a contacted NW embedded in a bow-tie nanoantennas array. The NW diameter is 150 nm and the distance between nanoantennas is $d = 400 \text{ nm}$.

to concentrate the light. Overall, the capacity of the antennas to concentrate light increases when their density is high. There are certain wavelengths for which this concentration is remarkably enhanced. For example, we observe resonances at 660 and 770 nm for an inter-antenna distance of 550 nm . In the system, the resonances move spectrally as a function of the inter-antenna distance due to their capacitive coupling. Fig. 6.6d plots the square of the electric field across the antenna gap for these resonances. Light is concentrated in the gap region closest to the antennas. The absorption spectrum of the full NW when sandwiched between a bow-tie antenna array is shown in Fig. 6.6e, as a function of the inter-antenna distance. At large inter-antenna distances, the absorption in the NW is lightly affected. The absorption is instead enhanced in the spectral region between 650 and 840 nm , by bringing the antennas closer together. If we look now at the profile of the absorption modes in the NW for an inter-antenna distance of 550 nm , we can see that the intensity of modes α_1 and β_1 has changed. We also underline that for $\lambda = 840 \text{ nm}$, the nanoantennas generate an absorption enhancement in the NW of 15 times. This enhanced point γ_3 exhibits an intensity profile

6.4. Absorption in the hybrid system

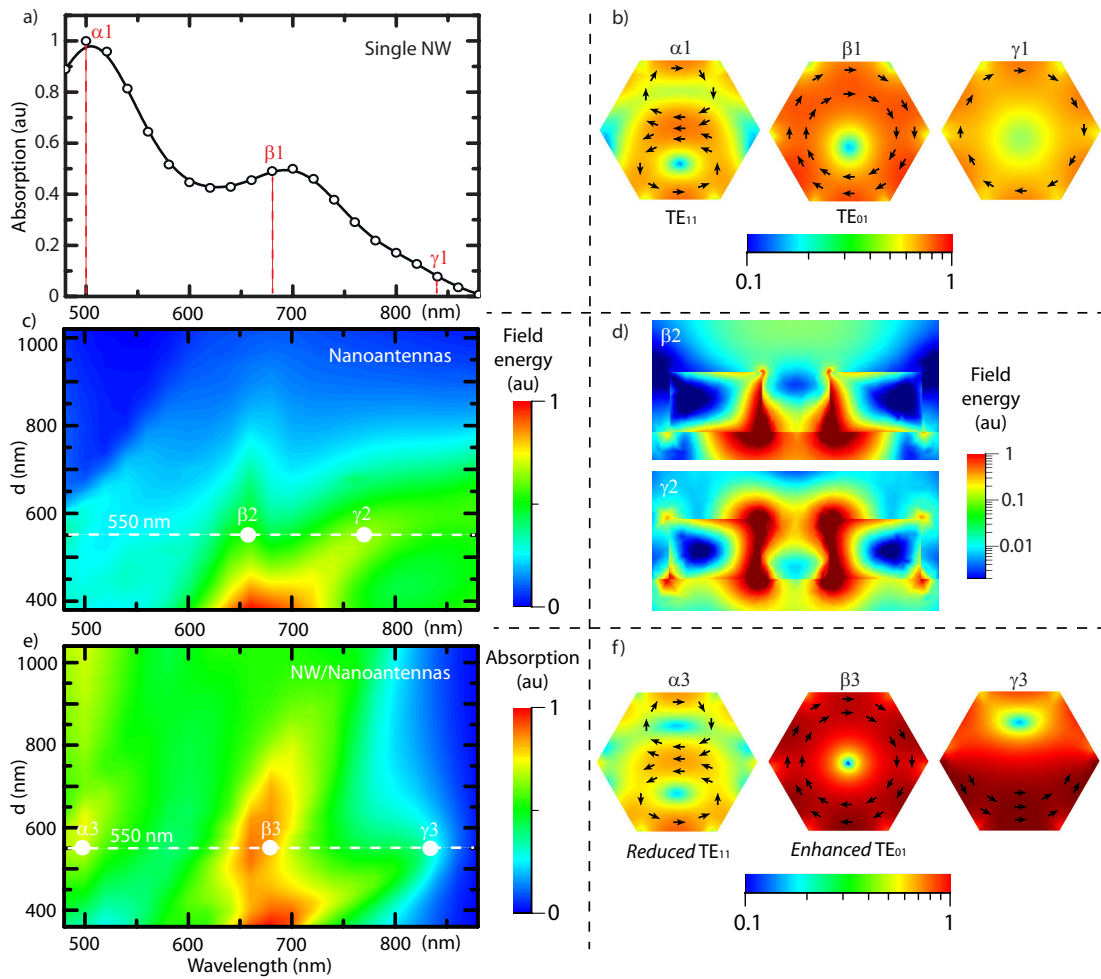


Figure 6.6: a) Calculated absorption spectra of a GaAs NW of 150 nm in diameter laying on a glass substrate. For the points α_1 , β_1 and γ_1 the electric field intensity and the electric field lines are represented along the NW cross section in b). c) Calculated field energy map for an array of gold antennas on glass in function of the wavelength and the nanoantennas distance d . d) Field energy distribution in the plane along the antennas axis corresponding to the points β_2 and γ_2 . e) Calculated absorption map for the NW/nanoantennas system on a glass substrate as a function of the nanoantenna distance d . The corresponding α_3 , β_3 and γ_3 electric field intensity and in-plane electric field lines are shown in f). All the calculations are made with perpendicularly incident transverse polarized light. *Copyright ©2015, Rights Managed by Nature Publishing Group.*

similar to what it is expected from the antenna geometry.

We have calculated the field energy distribution cross section with and without the NW (Fig: 6.7) in order to highlight the nanoantennas ability to concentrate the incoming light into the NW. We observe that the field energy distribution is concentrated along the gold antennas edges. A very small part of energy is localized in the middle nanoantennas gap (Fig. 6.7c). The

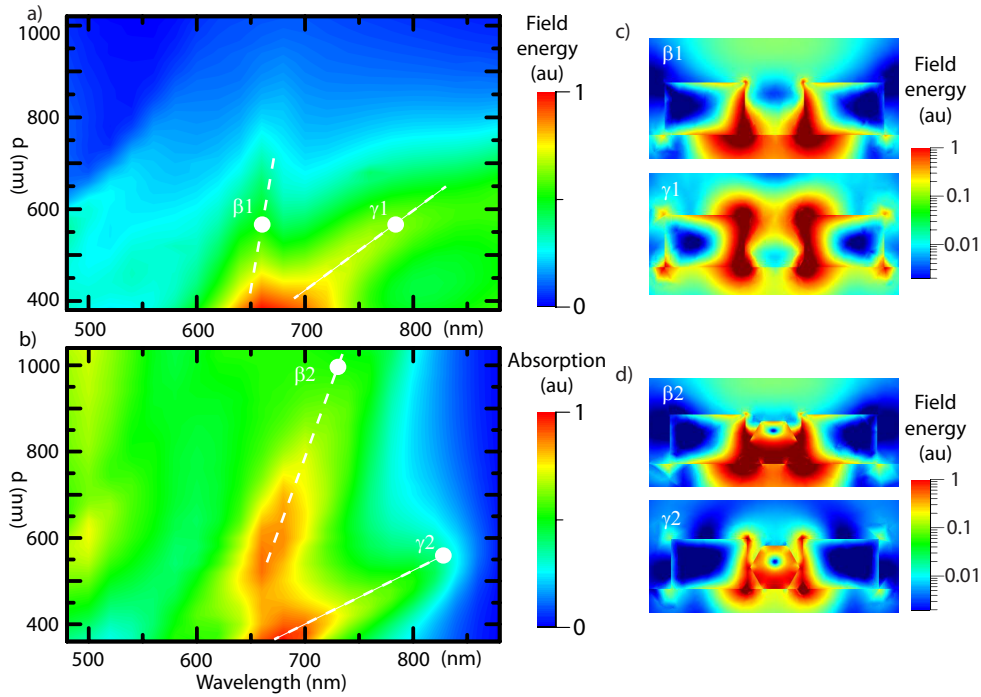


Figure 6.7: a) Field energy map for transverse polarization in the system with only nanoantennas in function of the wavelength and the nanoantennas distance. The electric field intensity is integrated on the volume that would correspond to the NW volume in the system NW-nanoantennas. b) Map of the NW absorption for transverse polarized light. c) and d) show the field energy distribution along the system cross section for the corresponding white points of figure a) and b).

GaAs NWs have a dielectric constant almost 13 times higher than one of the vacuum. Because of this the NW embedded in the antenna array acts as a cavity and it collects the electric field energy. In fig. 6.7, we observe that the absorption modes are wider and more pronounced for the hybrid NW/nanoantennas system. The energy field distribution is localized inside the NW beside to the antennas edges (fig.6.7d).

6.5 Photocurrent response

The absorption in the NW/bow-tie antenna system has been obtained by photoconductivity measurements. Photoconductivity measurements are performed with two point electrical measurements. A superK Koheras continuous laser is used to excite the devices with monochromatic light. Light is incident on the full hybrid system and the power is set constant for all the wavelengths to $10 \mu W$. We used an optical polarizer to change the light polarization and a CCD camera is used to control the location of the incident light on the sample. During the data acquisition we supplied a power with a constant voltage of $50 mV$ and we measure the current passing through the NW.

We have fabricated devices with various inter-antenna distances: 1000 and 400 nm. The predicted absorption and experimental photoconductivity spectra of NWs for polarizations along and across the NW axis are shown in Figures 6.8a-c and d-f respectively. Fig. 6.8a shows the photoconductivity spectra of a single NW. As expected, we observe higher absorption for wavelengths close to 500 nm and 650 nm, corresponding to the existence of optical guided modes. As a consequence of the one-dimensional shape of the NW [184, 185], the absorption is significantly higher for polarization parallel to the NW axis. In Fig. 6.8b we show that the polarization anisotropy is suppressed by the addition of low dense bow-tie antennas ($d = 1000$ nm). Moreover, this suppression is broad-band and is valid from 500 to 900 nm. By bringing the antenna closer together (400 nm), we favor light absorption for light polarized perpendicular to the NW axis, at least for the spectral range between 600 and 750 nm.

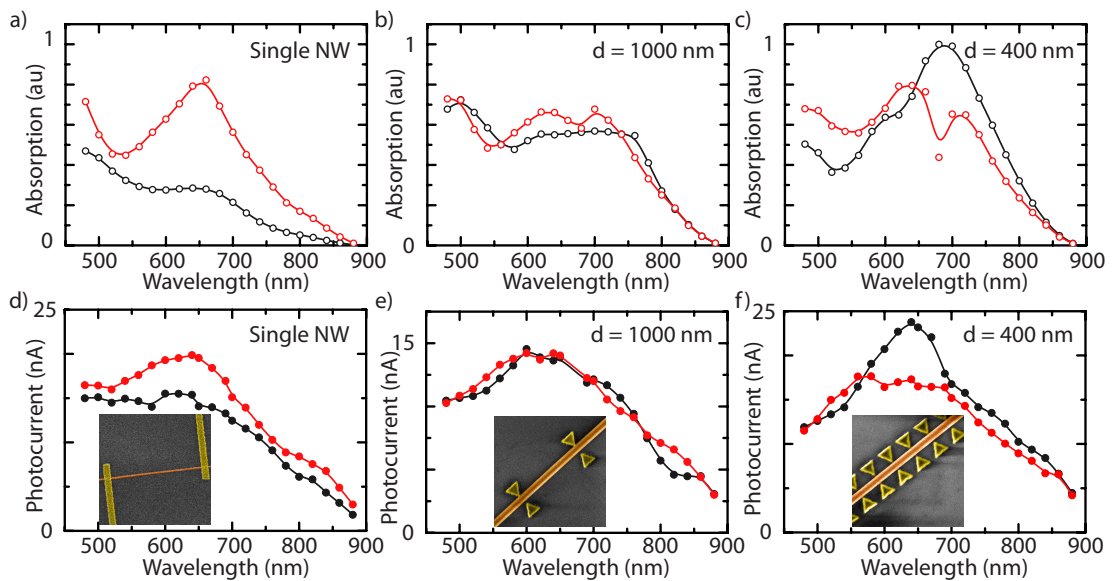


Figure 6.8: Calculated absorption efficiency spectra of a single NW a) and NW/nanoantennas systems with antenna distance $d = 1000$ b) and $d = 400$ nm c). The black points correspond to calculation for light perpendicular to the NW axis and the red for light parallel to the NW. d), e) and f) represent the photo-current electrical measurements of the corresponding above calculations obtained for a laser power of $10 \mu W$. In the insets the scanning electron microscopy images of the analyzed devices. The lines between the points are guides for the eyes. Copyright ©2015, Rights Managed by Nature Publishing Group.

In Figs. 6.8d-f we experimentally observe the predicted switched anisotropic absorption through photocurrent measurements in real devices. Thanks to the addition of the bow-tie nanoantennas close to the NW, we concentrate the incoming light and thereby we increase the photo-current related to light polarized across the NW axis. Our calculation show that light absorption can be enhanced up to a factor 3.6 with respect to a single NW in the spectral region between 650 and 750 nm. In addition, the absorption for longitudinal polarized

light is not significantly modified. The simulated absorption efficiency values can be quantitatively compared between all device configurations. In contrast, a direct comparison of photo-current absolute values between different real devices is not possible. Changes in the photoconductance and measured photocurrent between different devices can be attributed to small variations in the NW diameter and distance between the contacts. For this reason, we report in figures 6.8d, 6.8e and 6.8f the absolute values of the photocurrent. More than two devices have been fabricated for each design and the results are consistent.

6.6 Photocurrent scanning map

Here we demonstrate that bow-tie nanoantennas are able to extremely localize the incoming light into the NW. As a proof of increased photo-current in sub-wavelength NW regions we performed photo-scanning electrical measurements. We use a piezo-stage to automatically scan the laser spot around the device, while collecting the current at each position. The scan was taken with steps of 200 nm. The laser spot on the sample is diffraction limited and is approximatively 1 μm . This value will thus correspond to our lower-limit for the spatial resolution. Therefore, in order to excite one nanoantenna at a time, only devices with $d = 1000$ nm have been analyzed.

By increasing the inter-antenna distance d , the nanoantennas loose most of their capability to increase the absorption in the NW. However, still for $d = 1000$ nm there is an absorption mode at $\lambda = 750$ nm that enhances the NW absorption efficiency. Therefore we set this wavelength to investigate the photo-carrier generation in the system for both s and p-polarizations.

We report the photo-current map related to transverse polarized incident light at $\lambda = 750$ nm in Fig. 6.9a. The GaAs NW and antenna positions have been overladed for clarity. The device is excited by a laser power of 18 μW and 50 mV are also applied at the electrodes in order to extract the photo-carriers. The blue region in the contour plot corresponds to the area where the laser is not probing the NW, thus is related to the dark current. When the laser spot is on the NW the current increases due to the generation of photo-carriers. It is worth to notice that there is no Schottky barrier in proximity to the contacts, which indicates that any effects related to the contacts can be excluded.

It is also interesting to notice that the photo-current is not homogeneous along the NW. In particular, we observe an enhancement of photo-current right in the vicinity of the nanoantennas position. This trend is more clear by plotting the photo-current profile along the NW (Fig. 6.9b). We also include the photo-current profile given by longitudinal polarized light. At first sight, one can already observe that the two photo-current profiles are different at the position of the nanoantenna. In order to explain this phenomenon, let us distinguish between the laser spot being on the nanoantenna (region 1) and when located between two nanoantennas (region 2). In the profile for the s-polarised light, the photo-current is always enhanced in regions of type 1, while is reduced in regions of type 2. We notice that, the nanoantennas adjacent to the electrical contacts give a smaller contribution to the creation of photo-carriers.

The close presence of the contacts change the light coupling which becomes less efficient.

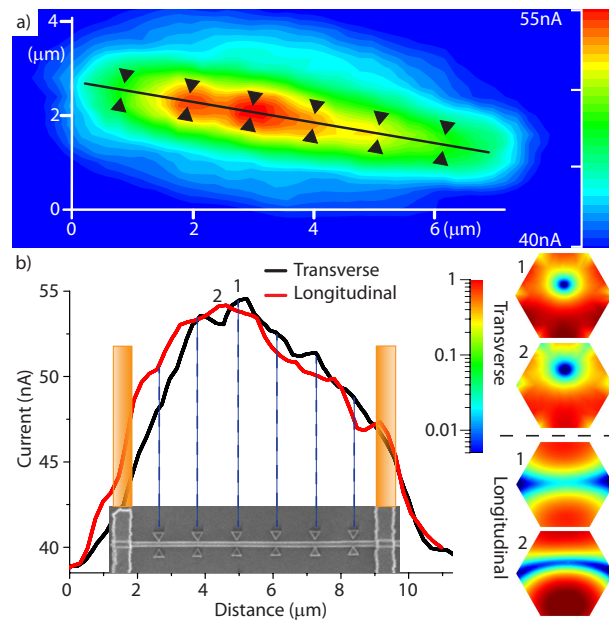


Figure 6.9: a) 2D photo-current map of a system $d = 1000 \text{ nm}$ with 6 nanoantennas represented in back. A super-continuum laser and a piezo-stage are used to scan the device with incident transverse polarized light with $\lambda = 750 \text{ nm}$. The different colors correspond to different photo-current levels: blue the lowest and white the highest. b) Current profile along the NW axis for transverse polarized (black) and longitudinally polarized (red) light with $\lambda = 750 \text{ nm}$. The SEM shows the position of the contacts and the nanoantennas. On the left, the simulated field energy distribution along the NW cross section for both polarizations in 2 different positions: 1) on the nanoantenna position and 2) at half way between 2 nanoantennas. The color scale is in logarithmic values.

6.7 Conclusions

We have demonstrated the control and engineer of the polarization and spectra response of NWs through the coupling with a bow-tie antenna array. Calculations and photo-conductivity measurements show that bow-tie nanoantennas behave like a dipole antennas. We also show that when excited with transverse polarized light, nanoantennas plasmonic couple with the NW. The NW/bow-tie antenna platform gives the opportunity to engineer a class of devices with a light response that can be adapted the the technological need. The adaptability and control of this design makes this platform an optimal candidate for engineering nano opto-electronic devices like solar cells, photo-detectors optical switches, optical emitters and modulators.

Conclusions

In this work, optical and electrical properties of low dimensional semiconductor nanowires (NWs) were investigated. The main goal of this thesis was the understanding of the NW physical properties followed by the engineering of new systems with desired characteristics. A detailed understanding of the electrical transport and the NW light interaction are fundamental for the realization of NW based devices. In particular this work is dedicated to the investigation of GaAs/AlGaAs heterostructure for high mobility nano-devices and hybrid NW/nanoantennas system for light detection and emission.

In order for NWs to become a technological reality, control of the conductivity by doping is extremely important. The incorporation paths of dopants in NWs have been discussed in the last few years, with a goal of controlling their concentration and position in the NW. For this, the understanding of the growth process is important. Bottom-up grown NWs have been grown via the vapor-liquid-solid mechanism in a molecular beam epitaxy (MBE) chamber. It is generally accepted that the incorporation paths of dopants are similar from the growth precursors and result either from the radial growth of the NW or through diffusion through the catalyst. Still, one may consider a third path, which consists of the diffusion of dopants in the core and/or from the shell to the nanowire core. The relevance of this path should depend on the diffusion coefficient of the dopants and the growth temperatures used. Typical dopants with a high diffusion coefficients in III-Vs are Be and Te. In chapter 3 we investigate GaAs NWs doped with Be. The existence of this third path is found by means of conductivity measurements on samples with doping concentrations ranging between $6 \cdot 10^{17}$ and $2 \cdot 10^{19} \text{ cm}^{-3}$. On the other hand we show that Be atoms are mostly incorporated from the side facets and that the incorporation through the Ga droplet is negligible.

In chapter 3, we report on the electrical properties of Carbon-doped GaAs NWs. As C is not soluble in Ga, its incorporation in the nanowire core through the droplet remains difficult. Our strategy is then to grow an intrinsic NW core and a doped shell around it. The growth of the shell is similar to the thin film growth. Since in ambient conditions there is a formation of a thin oxide layer on the GaAs NW surface, the Fermi level is pinned in the middle of the band-gap. The existence of this region reduces the electrically active part of the NWs. Here we avoid this problem by passivating the GaAs with a wider band gap semiconductor, AlGaAs. We measure the carrier concentration, mobility and minority diffusion length for core-shell GaAs NWs where the shell is C-doped at different concentrations. The effect of

Conclusions

the surface states is evaluated by comparing the values for passivated and unpassivated NWs. A priori, one would expect a higher mobility for passivated nanowires with respect to the unpassivated, but we do not observe this. By calculating the electrical carriers' profile inside the NW, we observe two mechanisms that contribute to the observation of the highest mobility in unpassivated NWs. First, the depletion region in unpassivated and low-doped NWs ensures that carrier transport occurs at a certain distance from the surface and reduces the surface-related scattering. Second, a higher proportion of the transport occurs through the undoped core, which exhibits higher mobility due to the absence of dopants. The highest mobility ($30 \text{ cm}^2/V \cdot \text{s}$) was obtained for unpassivated NWs with a doping concentration of $1.3 \cdot 10^{18} \text{ cm}^{-3}$. Finally, we observe a minority carrier diffusion lengths up to 190 nm for passivated NWs with a doping concentration of 10^{18} cm^{-3} . This corresponds to a diffusion increase of 10 times respect to unpassivated NWs.

In chapter 4, we investigate the physical properties of modulation doping structure in the NW geometry. Our simulations show that electrons can be localized in the core with a 3D, 2D or 1D distribution as a function of the doping concentration. In the ideal situation we would like to have a large amount of carriers in the core, but technical limitation related to the growth prevent having a highly doped Si shell. In this chapter we overcome this by increasing the δ -doped shell thickness from 3 to 10 nm . This change in geometry leads to a larger number of carriers and leave the modulation doping principle of having carriers migrating from the doped region to the core intrinsic region unaltered. Additional calculations demonstrate that by substituting the AlGaAs doped shell with the GaAs doped shell, part of the carriers do not migrate to the core and this number is directly linked to the thickness of the doped region. We also observed that, in terms of carrier distribution, the ideal spacer between the GaAs core and the doped shell should be less than 15 nm , confirming analogous results obtained for the thin-film geometry. Michael B. Johnston *et al.* analyzed our modulation doped GaAs/AlGaAs NWs with terahertz spectroscopy obtaining a carrier mobility of $2200 \pm 300 \text{ cm}^2/V \cdot \text{s}$, which is one of the highest mobility values obtained for GaAs NWs.

In chapter 5, we fabricate a hybrid system made of a single NW and an array of nanoantennas. Although a significant amount of work has been devoted to understanding and manipulating the optical responses of individual semiconductor NWs and plasmonic systems, little was currently known about their optical coupling regime. Here, we investigate the resonant coupling of semiconductor NWs and plasmonic nanoantennas. We demonstrate photonic-plasmonic resonances of Au nanoantennas coupled to a GaAs NW in a controlled and reproducible way. We use dark-field scattering and second harmonic generation spectroscopy in partnership with analytical and full-vector finite-difference time-domain (FDTD) modeling, to investigate the electromagnetic coupling and near-field concentration between nanoantennas and NWs. Moreover, we show the ability to tailor the nonlinear optical response of individual GaAs NWs by engineering their near-field coupling regime. A complementary work has been performed with Yagi-Uda antennas and NWs. Yagi-Uda optical antennas are an example of a structure showing a pronounced directionality of emission. We realize a hybrid semiconductor-metal Yagi-Uda antenna by replacing the resonant metallic feed element of the Yagi-Uda by a non-

resonant semiconductor NW. By using Fourier spectroscopy, we observe strong directional emission from this hybrid system. We also demonstrate that the directionality of the emission is modified by varying the size of the Yagi-Uda elements. FDTD simulations of the emission show excellent agreement with the experimental data. These results constitute the first steps toward the realization of electrically driven directional antennas based on semiconductor NWs.

In the last chapter of the thesis (chapter 6) we design a plasmonic antenna to directly counteract the characteristic anisotropic polarization response of GaAs nanowires, without diminishing the absorption rate of light polarized along the NW. This enables to engineer the NW polarization response up to the point of inversion. It also allow to enhance the NW absorption in the visible spectrum. Our calculation indicate light absorption enhancement up to 15 times in the infrared. This design principles can be extended to other materials and other regions of the electromagnetic spectrum. Calculations and measurements show that bow-tie nanoantennas couple plasmonically with the NW when excited with transverse polarized light. The NW/bow-tie antenna platform gives the opportunity to engineer the devices light response. The optimal opto-electrical properties of GaAs, such as a direct band-gap in the visible range, high absorption coefficient and high charge mobility, imply a very high potential of this platform for a multitude of nano-optoelectronic devices.

Bibliography

- [1] D. Chandler and E. V. Thomas, "Progress in infrared photodetectors since 2000," *Advanced Functional Materials*, vol. 13, no. 14, pp. 5054–5098, 2013.
- [2] R. Wagner and W. Ellis, "Vapor-liquid-solid mechanism of single crystal growth," *Applied Physics Letters*, vol. 4, pp. 89 – 90, Jan. 1964.
- [3] M. Yazawa, M. Koguchi, and K. Hiruma, "Heteroepitaxial ultrafine wire-like growth of InAs on GaAs substrates," *Applied Physics Letters*, vol. 58, p. 1080, Jan. 1991.
- [4] K. Hiruma, M. Yazawa, and T. Katsuyama, "Growth and optical properties of nanometer-scale GaAs and InAs whiskers," *Journal of Applied Physics*, vol. 77, p. 477, Jan. 1995.
- [5] V. Mourik, K. Zuo, S. M. Frolov, S. R. Plissard, E. P. A. M. Bakkers, and L. P. Kouwenhoven, "Signatures of Majorana Fermions in Hybrid Superconductor-Semiconductor Nanowire Devices," *Science*, vol. 336, pp. 1003–1007, May 2012.
- [6] W. Lu, J. Xiang, B. Timko, and Y. Wu, "One-dimensional hole gas in germanium/silicon nanowire heterostructures," *PNAS*, vol. 102, p. 10046, Jan. 2005.
- [7] J. Xiang, W. Lu, Y. Hu, Y. Wu, H. Yan, and C. M. Lieber, "Ge/Si nanowire heterostructures as high-performance field-effect transistors," *Nature*, vol. 441, pp. 489–493, May 2006.
- [8] C. V. Falub, H. von Kanel, F. Isa, R. Bergamaschini, A. Marzegalli, D. Chrastina, G. Isella, E. Muller, P. Niedermann, and L. Miglio, "Scaling Hetero-Epitaxy from Layers to Three-Dimensional Crystals," *Science*, vol. 335, pp. 1330–1334, Mar. 2012.
- [9] M. Nolan, S. O'Callaghan, G. Fagas, J. C. Greer, and T. Frauenheim, "Silicon Nanowire Band Gap Modification," *Nano Letters*, vol. 7, pp. 34–38, Jan. 2007.
- [10] K.-H. Hong, J. Kim, S.-H. Lee, and J. K. Shin, "Strain-Driven Electronic Band Structure Modulation of Si Nanowires," *Nano Letters*, vol. 8, pp. 1335–1340, May 2008.
- [11] S. Assali, I. Zardo, S. Plissard, D. Kriegner, M. A. Verheijen, G. Bauer, A. Meijerink, A. Belabbes, F. Bechstedt, J. E. Haverkort, and E. P. Bakkers, "Direct Band Gap Wurtzite Gallium Phosphide Nanowires," *Nano Letters*, vol. 13, pp. 1559–1563, Mar. 2013.

Bibliography

- [12] A. Bertoni, M. Royo, F. Mahawish, and G. Goldoni, "Electron and hole gas in modulation-doped $GaAs/Al_{1-x}Ga_xAs$ radial heterojunctions," *Physical Review B*, vol. 84, p. 205323, Nov. 2011.
- [13] S. Funk, M. Royo, I. Zardo, D. Rudolph, S. Morkötter, B. Mayer, J. Becker, A. Bechtold, S. Matich, M. Döblinger, M. Bichler, G. Koblmüller, J. J. Finley, A. Bertoni, G. Goldoni, and G. Abstreiter, "High Mobility One- and Two-Dimensional Electron Systems in Nanowire-Based Quantum Heterostructures," *Nano Letters*, vol. 13, pp. 6189–6196, Dec. 2013.
- [14] M. Heiss, Y. Fontana, A. Gustafsson, G. Wüst, C. Magen, D. D. O'Regan, J. W. Luo, B. Ketterer, S. Conesa-Boj, A. V. Kuhlmann, J. Houel, E. Russo-Averchi, J. R. Morante, M. Cantoni, N. Marzari, J. Arbiol, A. Zunger, R. J. Warburton, A. F. i. Morral, D. D. O'Regan, and A. F. Morral, "Self-assembled quantum dots in a nanowire system for quantum photonics," *Nature Materials*, Feb. 2013.
- [15] B. Kayes, H. Atwater, and N. Lewis, "Comparison of the device physics principles of planar and radial pn junction nanorod solar cells," *Journal of Applied Physics*, Jan. 2005.
- [16] P. Krogstrup, H. I. Jørgensen, M. Heiss, O. Demichel, J. V. Holm, M. Aagesen, J. Nygard, A. F. i. Morral, and A. F. Morral, "Single-nanowire solar cells beyond the shockley–queisser limit," *Nature Photonics*, vol. 7, pp. 306–310, April 2013.
- [17] X. Duan, Y. Huang, Y. Cui, J. Wang, and C. Lieber, "Indium phosphide nanowires as building blocks for nanoscale electronic and optoelectronic devices," *Nature*, vol. 409, pp. 66–69, Jan. 2001.
- [18] M. H. Huang, S. Mao, H. Feick, H. Yan, Y. Wu, H. Kind, E. Weber, R. Russo, and P. Yang, "Room-Temperature Ultraviolet Nanowire Nanolasers," *Science*, vol. 292, pp. 1897–1899, June 2001.
- [19] X. Duan, Y. Huang, R. Agarwal, and C. Lieber, "Single-nanowire electrically driven lasers," *Nature*, vol. 421, pp. 241–245, Jan. 2003.
- [20] H. Joyce, P. Parkinson, N. Jiang, C. Docherty, and Q. Gao, "Electron Mobilities Approaching Bulk Limits in " Surface-Free " GaAs Nanowires," *Nano Letters*, vol. 14, pp. 5989–5994, Jan. 2014.
- [21] J. Boland, S. Conesa-Boj, P. Parkinson, G. Tutuncuoglu, F. Matteini, D. Ruffer, C. A. A. Amaduzzi, F. Jabeen, C. Davies, H. Joyce, A. i. Morral, and M. Johnston, "Modulation Doping of GaAs/AlGaAs Core–Shell Nanowires With Effective Defect Passivation and High Electron Mobility," *Nano Letters*, vol. 15, pp. 1336–1342, Jan. 2015.
- [22] Y. Huang, X. Duan, and C. Lieber, "Nanowires for integrated multicolor nanophotonics," *Small*, vol. 1, pp. 142 – 147, Jan. 2005.
- [23] W. Guo, A. Banerjee, and P. Bhattacharya, "InGaN/GaN disk-in-nanowire white light emitting diodes on (001) silicon," *Applied Physics Letters*, vol. 98, p. 193102, Jan. 2011.

- [24] Y. Cui, Q. Wei, H. Park, and C. Lieber, "Nanowire nanosensors for highly sensitive and selective detection of biological and chemical species," *Science*, vol. 93, pp. 1289–1292, Jan. 2001.
- [25] Q. Wan, Q. Li, Y. Chen, T. Wang, and X. He, "Fabrication and ethanol sensing characteristics of ZnO nanowire gas sensors," *Applied Physics Letters*, vol. 84, pp. 3654 – 3656, Jan. 2004.
- [26] A. Kolmakov, Y. Zhang, and G. Cheng, "Detection of CO and O₂ using tin oxide nanowire sensors," *Advanced Materials*, vol. 15, pp. 997–1000, Jan. 2003.
- [27] F. Patolsky, B. Timko, G. Yu, Y. Fang, A. Greytak, G. Zheng, and C. Lieber, "Detection, Stimulation, and Inhibition of Neuronal Signals with High-Density Nanowire Transistor Arrays," *Science*, vol. 313, pp. 1100–1104, Aug. 2006.
- [28] R. S. Kane and A. D. Stroock, "Nanobiotechnology: Protein-Nanomaterial Interactions," *Biotechnology Progress*, vol. 23, pp. 316–319, Apr. 2007.
- [29] A. I. Hochbaum, R. Chen, R. D. Delgado, W. Liang, E. C. Garnett, M. Najarian, A. Majumdar, and P. Yang, "Enhanced thermoelectric performance of rough silicon nanowires," *Nature*, vol. 451, pp. 163–167, Jan. 2008.
- [30] M. S. Dresselhaus, G. Chen, M. Y. Tang, R. G. Yang, H. Lee, D. Z. Wang, Z. F. Ren, J. P. Fleurial, and P. Gogna, "New Directions for Low-Dimensional Thermoelectric Materials," *Advanced Materials*, vol. 19, pp. 1043–1053, Apr. 2007.
- [31] V. Schmidt, J. V. Wittemann, S. Senz, and U. Gösele, "Silicon Nanowires: A Review on Aspects of their Growth and their Electrical Properties," *Advanced Materials*, vol. 21, pp. 2681–2702, July 2009.
- [32] S. T. Pantelides, *Deep Centers in Semiconductors*. Gordon and Breach Science Publisher, 1992.
- [33] E. R. Hemesath, D. K. Schreiber, E. B. Gulsoy, C. F. Kieselowski, A. K. Petford-Long, P. W. Voorhees, and L. J. Lauhon, "Catalyst Incorporation at Defects during Nanowire Growth," *Nano Letters*, vol. 12, pp. 167–171, Jan. 2012.
- [34] A. F. Morral, C. Colombo, G. Abstreiter, J. Arbiol, and J. R. Morante, "Nucleation mechanism of gallium-assisted molecular beam epitaxy growth of gallium arsenide nanowires," *Applied Physics Letters*, vol. 92, p. 063112, Jan. 2008.
- [35] C. Colombo, D. Spirkoska, M. Frimmer, G. Abstreiter, and A. Fontcuberta i Morral, "Ga-assisted catalyst-free growth mechanism of GaAs nanowires by molecular beam epitaxy," *Phys. Rev. B*, vol. 77, p. 155326, Apr 2008.
- [36] J. H. Paek, T. Nishiwaki, M. Yamaguchi, and N. Sawaki, "Catalyst free MBE-VLS growth of GaAs nanowires on (111)Si substrate," *Physica Status Solidi (c)*, vol. 6, pp. 1436–1440, June 2009.

Bibliography

- [37] S. Plissard, K. Dick, G. Larrieu, and S. Godey, "Gold-free growth of GaAs nanowires on silicon: arrays and polytypism," *Nanotechnology*, vol. 21, p. 385602, Jan. 2010.
- [38] P. Krogstrup, R. Popovitz-Biro, E. Johnson, M. H. Madsen, J. Nygard, and H. Shtrikman, "Structural phase control in self-catalyzed growth of GaAs nanowires on silicon (111)," *Nano Letters*, vol. 10, no. 11, pp. 4475–4482, 2010.
- [39] E. Uccelli, J. Arbiol, C. Magen, P. Krogstrup, E. Russo-Averchi, M. Heiss, G. Mugny, F. Morier-Genoud, J. Nygard, J. R. Morante, and A. Fontcuberta i Morral, "Three-dimensional multiple-order twinning of self-catalyzed GaAs nanowires on Si substrates," *Nano Letters*, vol. 11, no. 9, pp. 3827–3832, 2011.
- [40] E. Russo-Averchi, M. Heiss, L. Michelet, P. Krogstrup, J. Nygard, C. Magen, J. R. Morante, E. Uccelli, J. Arbiol, and A. F. Morral, "Suppression of three dimensional twinning for GaAs on silicon," *Nanoscale*, vol. 4, p. 1486, Jan. 2012.
- [41] C. Somaschini, S. Bietti, A. Trampert, U. Jahn, C. Hauswald, H. Riechert, S. Sanguinetti, and L. Geelhaar, "Control over the Number Density and Diameter of GaAs Nanowires on Si(111) Mediated by Droplet Epitaxy," *Nano Letters*, vol. 13, pp. 3607–3613, Aug. 2013.
- [42] F. Matteini, V. G. Dubrovskii, D. Ruffer, G. Tutuncuoglu, Y. Fontana, and A. Fontcuberta i Morral, "Tailoring the diameter and density of self-catalyzed GaAs nanowires on silicon," *Nanotechnology*, vol. 26, p. 105603, 2015.
- [43] P. Caroff, K. A. Dick, J. Johansson, M. E. Messing, K. Deppert, and L. Samuelson, "Controlled polytypic and twin-plane superlattices in III–V nanowires," *Nature Nanotechnology*, vol. 4, pp. 50–55, Nov. 2008.
- [44] V. Zannier, V. Grillo, F. Martelli, J. R. Plaisier, A. Lausi, and S. Rubini, "Tuning the growth mode of nanowires via the interaction among seeds, substrates and beam fluxes," *Nanoscale*, vol. 6, p. 8392, Jan. 2014.
- [45] B. Tian, X. Zheng, T. J. Kempa, Y. Fang, N. Yu, G. Yu, J. Huang, and C. M. Lieber, "Coaxial silicon nanowires as solar cells and nanoelectronic power sources," *Nature*, vol. 449, pp. 885–889, Oct. 2007.
- [46] C. Colombo, M. Heibeta, M. Gratzel, and A. F. i Morral, "Gallium arsenide p-i-n radial structures for photovoltaic applications," *Applied Physics Letters*, vol. 94, no. 17, p. 173108, 2009.
- [47] O. Hayden, R. Agarwal, and C. Lieber, "Nanoscale avalanche photodiodes for highly sensitive and spatially resolved photon detection," *Nature Materials*, vol. 5, p. 352, Jan. 2006.
- [48] O. Hayden, A. Greytak, and D. Bell, "Core–Shell Nanowire Light Emitting Diodes," *Advanced Materials*, vol. 17, pp. 701 – 704, Jan. 2006.

- [49] M. Tchernycheva, A. Messanvi, A. Luna de Bugallo, G. Jacopin, P. Lavenus, L. Rigutti, H. Zhang, Y. Halioua, F. H. Julien, J. Eymery, and C. Durand, "Integrated Photonic Platform Based on InGaN/GaN Nanowire Emitters and Detectors," *Nano Letters*, vol. 14, pp. 3515–3520, June 2014.
- [50] C.-C. Chang, C.-Y. Chi, M. Yao, N. Huang, C.-C. Chen, J. Theiss, A. W. Bushmaker, S. LaLumondiere, T.-W. Yeh, M. L. Povinelli, C. Zhou, P. D. Dapkus, and S. B. Cronin, "Electrical and optical characterization of surface passivation in GaAs nanowires," *Nano Letters*, vol. 12, pp. 4484–4489, October 2012.
- [51] A. Casadei, J. Schwender, E. Russo-Averchi, D. Ruffer, M. Heiss, E. Alarcó-Lladó, F. Jabeen, M. Ramezani, K. Nielsch, and A. Fontcuberta i Morral, "Electrical transport in C-doped GaAs nanowires: surface effects," *physica status solidi (RRL) - Rapid Research Letters*, vol. 7, pp. 890–893, Oct. 2013.
- [52] J. R. Riley, S. Padalkar, Q. Li, P. Lu, D. D. Koleske, J. J. Wierer, G. T. Wang, and L. J. Lauhon, "Three-Dimensional Mapping of Quantum Wells in a GaN/InGaN Core–Shell Nanowire Light-Emitting Diode Array," *Nano Letters*, vol. 13, pp. 4317–4325, Sept. 2013.
- [53] L. J. Lauhon, M. S. Gudiksen, D. Wang, and C. M. Lieber, "Epitaxial core–shell and core–multishell nanowire heterostructures," *Nature*, vol. 420, pp. 57–61, Nov. 2002.
- [54] D. C. Dillen, K. Kim, E.-S. Liu, and E. Tutuc, "Radial modulation doping in core–shell nanowires," *Nature Nanotechnology*, vol. 9, pp. 116–120, Jan. 2014.
- [55] M. Heigoldt, J. Arbiol, D. Spirkoska, and J. Rebled, "Long range epitaxial growth of prismatic heterostructures on the facets of catalyst-free GaAs nanowires," *Journal of Materials Chemistry*, vol. 19, p. 840, February 2009.
- [56] A. Baca, F. Ren, J. Zolper, R. Briggs, and S. Pearton, "A survey of ohmic contacts to III-V compound semiconductors," *Thin Solid Films*, vol. 308-309, pp. 599–606, Jan. 1997.
- [57] J. Dufouleur, C. Colombo, T. Garma, B. Ketterer, E. Uccelli, M. Nicotra, and A. Fontcuberta i Morral, "P-doping mechanisms in catalyst-free gallium arsenide nanowires," *Nano Letters*, vol. 10, no. 5, pp. 1734–1740, 2010.
- [58] A. Casadei, P. Krogstrup, M. Heiss, and J. Rohr, "Doping incorporation paths in catalyst-free Be-doped GaAs nanowires," *Applied Physics Letters*, vol. 102, p. 013117, February 2013.
- [59] C. Gutsche, A. Lysov, I. Regolin, K. Blekker, W. Prost, and F.-J. Tegude, "n-type doping of vapor-liquid-solid grown GaAs nanowires," *Nanoscale Research Letters*, vol. 6, pp. 1–6, 2010.
- [60] C. Gutsche, A. Lysov, I. Regolin, and A. Brodt, "Ohmic contacts to n-GaAs nanowires," *Journal of Applied Physics*, vol. 110, p. 014305, Jan. 2011.

Bibliography

- [61] R. E. Williams, *Modern GaAs Processing Methods*. 1990.
- [62] J. Kim, D. Lim, and G. Yang, "Selective etching of AlGaAs/GaAs structures using the solutions of citric acid/H₂O₂ and de-ionized H₂O/buffered oxide etch," *Journal of Vacuum Science and Technology B*, vol. 16, p. 558, Jan. 1998.
- [63] S. Wirths, M. Mikulics, and P. Heintzmann, "Preparation of Ohmic contacts to GaAs/AlGaAs-core/shell-nanowires," *Applied Physics Letters*, vol. 100, p. 042103, Jan. 2012.
- [64] D. Ruffer, "qstarter by nccr qsit, <http://www.qstarter.ch/projects/automated-contacting-of-random-microstructures>," 2014.
- [65] S. Dayeh, D. Aplin, X. Zhou, P. Yu, E. Yu, and D. Wang, "High Electron Mobility InAs Nanowire Field-Effect Transistors," *Small*, vol. 3, pp. 326–332, Jan. 2007.
- [66] R. A. Schlitz, D. E. Perea, J. L. Lensch-Falk, E. R. Hemesath, and L. J. Lauhon, "Correlating dopant distributions and electrical properties of boron-doped silicon nanowires," *Applied Physics Letters*, vol. 95, p. 162101, Jan. 2009.
- [67] Z. Zhang, K. Yao, Y. Liu, C. Jin, X. Liang, Q. Chen, and L.-M. Peng, "Quantitative analysis of current-voltage characteristics of semiconducting nanowires: Decoupling of contact effects," *Advanced Functional Materials*, vol. 17, no. 14, pp. 2478–2489, 2007.
- [68] E. Lind, A. I. Persson, L. Samuelson, and L.-E. Wernersson, "Improved Subthreshold Slope in an InAs Nanowire Heterostructure Field-Effect Transistor," *Nano Letters*, vol. 6, pp. 1842–1846, Sept. 2006.
- [69] K. Tomioka, M. Yoshimura, and T. Fukui, "A iii-v nanowire channel on silicon for high-performance vertical transistors," *Nature*, vol. 488, pp. 189–192, September 2012.
- [70] O. Shirak, O. Shtempluck, V. Kotchtakov, G. Bahir, and Y. E. Yaish, "High performance horizontal gate-all-around silicon nanowire field-effect transistors," *Nanotechnology*, vol. 23, pp. 1–9, Sept. 2012.
- [71] J. Goldberger, D. J. Sirbuly, M. Law, and P. Yang, "ZnO Nanowire Transistors," *The Journal of Physical Chemistry B*, vol. 109, pp. 9–14, Jan. 2005.
- [72] M. Egard, S. Johansson, A. C. Johansson, K. M. Persson, A. W. Dey, B. M. Borg, C. Thelander, L. E. Wernersson, and E. Lind, "Vertical InAs Nanowire Wrap Gate Transistors with $f_t > 7$ GHz and $f_{max} < 20$ GHz," *Nano Letters*, vol. 10, pp. 809–812, Mar. 2010.
- [73] K. Keem, D.-Y. Jeong, S. Kim, M.-S. Lee, I.-S. Yeo, U.-I. Chung, and J.-T. Moon, "Fabrication and Device Characterization of Omega-Shaped-Gate ZnO Nanowire Field-Effect Transistors," *Nano Letters*, vol. 6, pp. 1454–1458, July 2006.

- [74] R. Tu, L. Zhang, Y. Nishi, and H. Dai, "Measuring the Capacitance of Individual Semiconductor Nanowires for Carrier Mobility Assessment," *Nano Letters*, vol. 7, pp. 1561–1565, June 2007.
- [75] A. M. Burke, D. E. Waddington, D. J. Carrad, R. W. Lyttleton, H. H. Tan, P. J. Reece, O. Klochan, A. R. Hamilton, A. Rai, D. Reuter, A. D. Wieck, and A. P. Micolich, "Origin of gate hysteresis in p-type Si-doped AlGaAs/GaAs heterostructures," *Physical Review B*, vol. 86, p. 165309, Oct. 2012.
- [76] D. R. Khanal and J. Wu, "Gate coupling and charge distribution in nanowire field effect transistors," *Nano Letters*, vol. 7, pp. 2778–2783, September 2007.
- [77] C. Blömers, T. Grap, M. I. Lepsa, J. Moers, S. Trelenkamp, D. Grützmacher, H. Lüth, and T. Schäpers, "Hall effect measurements on InAs nanowires," *Applied Physics Letters*, vol. 101, p. 152106, Jan. 2012.
- [78] K. Storm, F. Halvardsson, M. Heurlin, D. Lindgren, A. Gustafsson, P. M. Wu, B. Monemar, and L. Samuelson, "Spatially resolved Hall effect measurement in a single semiconductor nanowire," *Nature Nanotechnology*, vol. 7, pp. 718–722, Oct. 2012.
- [79] M. L. Roukes, A. Scherer, S. J. Allen, Jr., H. G. Craighead, R. M. Ruthen, E. D. Beebe, and J. P. Harbison, "Quenching of the Hall Effect in a One-Dimensional Wire," *Physical Review Letters*, vol. 59, pp. 1–5, Mar. 2011.
- [80] A. Gustafsson, M. Björk, and L. Samuelson, "Locating nanowire heterostructures by electron beam induced current," *Nanotechnology*, vol. 18, p. 205306, Jan. 2007.
- [81] M. Troyon and K. Smaali, "Scanning near-field electron beam induced current microscopy: Application to III-V heterostructures and quantum dots," *Applied Physics Letters*, vol. 90, p. 212110, Jan. 2007.
- [82] J. Allen, E. Hemesath, D. Perea, J. Lensch-Falk, Z. Li, F. Yin, M. Gass, P. Wang, A. Bleloch, R. Palmer, and L. Lauhon, "High-resolution detection of Au catalyst atoms in Si nanowires," *Nature Nanotechnology*, vol. 3, pp. 168–173, Feb. 2008.
- [83] Y. Gu, J. P. Romankiewicz, J. K. David, J. L. Lensch, and L. J. Lauhon, "Quantitative Measurement of the Electron and Hole Mobility Lifetime Products in Semiconductor Nanowires," *Nano Letters*, vol. 6, pp. 948–952, May 2006.
- [84] O. Kurniawan and V. K. Ong, "Determination of Diffusion Lengths With the Use of EBIC From a Diffused Junction With Any Values of Junction Depths," *IEEE Transactions on Electron Devices*, vol. 53, pp. 2358–2363, Sept. 2006.
- [85] S. K. Ghosh and T. Pal, "Interparticle coupling effect on the surface plasmon resonance of gold nanoparticles: from theory to applications," *Chemical Reviews*, vol. 107, no. 11, pp. 4797–4862, 2007.

Bibliography

- [86] E. F. Pecora, A. Capretti, G. Miano, and L. D. Negro, "Generation of second harmonic radiation from sub-stoichiometric silicon nitride thin films," *Applied Physics Letters*, vol. 102, p. 141114, Jan. 2013.
- [87] E. F. Pecora, G. F. Walsh, C. Forestiere, A. Handin, E. Russo-Averchi, A. Dalmau-Mallorqui, I. Canales-Mundet, A. F. i. Morral, and L. D. Negro, "Enhanced second harmonic generation from InAs nano-wing structures on silicon," *Nanoscale*, vol. 5, p. 10163, Jan. 2013.
- [88] H. Kind, H. Yan, B. Messer, M. Law, and P. Yang, "Nanowire ultraviolet photodetectors and optical switches," *Advanced Materials*, vol. 14, pp. 158–160, Jan. 2002.
- [89] S. M. Sze, . *Physics of semiconductor devices*. Hoboken, New Jersey, John Wiley & Sons, Inc., 2007.
- [90] S. Thunich, L. Prechtel, D. Spirkoska, G. Abstreiter, A. F. Morral, and A. W. Holleitner, "Photocurrent and photoconductance properties of a GaAs nanowire," *Applied Physics Letters*, vol. 95, p. 083111, Jan. 2009.
- [91] M. Ahmad, K. Rasool, and M. Rafiq, "Enhanced and persistent photoconductivity in vertical silicon nanowires and ZnS nanoparticles hybrid devices," *Applied Physics Letters*, vol. 101, p. 223103, Jan. 2012.
- [92] G. Chen, G. Sun, Y. J. Ding, P. Prete, I. Miccoli, N. Lovergine, H. Shtrikman, P. Kung, T. Livneh, and J. E. Spanier, "Direct Measurement of Band Edge Discontinuity in Individual Core–Shell Nanowires by Photocurrent Spectroscopy," *Nano Letters*, vol. 13, pp. 4152–4157, Sept. 2013.
- [93] H.-Y. Chen, R.-S. Chen, N. K. Rajan, F.-C. Chang, L.-C. Chen, K.-H. Chen, Y.-J. Yang, and M. A. Reed, "Size-dependent persistent photocurrent and surface band bending in m-axial GaN nanowires," *Physical Review B*, vol. 84, p. 205443, Nov. 2011.
- [94] C. Soci, A. Zhang, B. Xiang, S. A. Dayeh, D. Aplin, J. Park, X. Bao, Y.-H. Lo, and D. Wang, "ZnO nanowire UV photodetectors with high internal gain," *Nano Letters*, vol. 7, pp. 1003–1009, Jan. 2007.
- [95] D. Rudolph, S. Funk, M. Döblinger, S. Morkötter, S. Hertenberger, L. Schweickert, J. Becker, S. Matich, M. Bichler, D. Spirkoska, I. Zardo, J. J. Finley, G. Abstreiter, and G. Koblmüller, "Spontaneous Alloy Composition Ordering in GaAs-AlGaAs Core–Shell Nanowires," *Nano Letters*, vol. 13, pp. 1522–1527, Mar. 2013.
- [96] O. Demichel, M. Heiss, J. Bleuse, H. Mariette, and A. F. Morral, "Impact of surfaces on the optical properties of GaAs nanowires," *Applied Physics Letters*, vol. 97, pp. 201907–201907–3, Jan. 2010.
- [97] J. Wang, M. S. Gudixsen, X. Duan, Y. Cui, and C. M. Lieber, "Highly Polarized Photoluminescence and Photodetection from Single Indium Phosphide Nanowires," *Science*, vol. 293, pp. 1455–1457, Aug. 2001.

- [98] L. Cao, J. S. White, J.-S. Park, J. A. Schuller, B. M. Clemens, and M. L. Brongersma, "Engineering light absorption in semiconductor nanowire devices," *Nature Materials*, vol. 8, pp. 643–647, July 2009.
- [99] C. Colombo, P. Krogstrup, J. Nygard, M. L Brongersma, and A. Fontcuberta i Morral, "Engineering light absorption in single-nanowire solar cells with metal nanoparticles," *New Journal of Physics*, vol. 13, p. 123026, 2011.
- [100] A. Casadei, E. A. Llado, F. Amaduzzi, E. Russo-Averchi, D. Ruffer, M. Heiss, L. D. Negro, and A. F. i. Morral, "Polarization response of nanowires à la carte," *Scientific reports*, vol. 5, p. 7651, Jan. 2015.
- [101] K. E. Moselund, H. Ghoneim, H. Schmid, M. T. Bjork, E. Lortscher, S. Karg, G. Signorello, D. Webb, M. Tschudy, R. Beyeler, and H. Riel, "Solid-state diffusion as an efficient doping method for silicon nanowires and nanowire field effect transistors," *Nanotechnology*, vol. 21, p. 435202, Sept. 2010.
- [102] H. Schmid, M. T. Björk, J. Knoch, S. Karg, H. Riel, and W. Riess, "Doping limits of grown in situ doped silicon nanowires using phosphine," *Nano Letters*, vol. 9, pp. 173–177, Jan. 2009.
- [103] C. Gutsche, I. Regolin, K. Blekker, A. Lysov, W. Prost, and F. J. Tegude, "Controllable p-type doping of GaAs nanowires during vapor-liquid-solid growth," *Journal of applied physics*, vol. 105, p. 024305, Jan. 2009.
- [104] O. Salehzadeh, K. L. Kavanagh, and S. P. Watkins, "Controlled axial and radial Te-doping of GaAs nanowires," *Journal of applied physics*, vol. 112, p. 054324, Jan. 2012.
- [105] M. Hilse, M. Ramsteiner, S. Breuer, L. Geelhaar, and H. Riechert, "Incorporation of the dopants si and be into gaas nanowires," *Applied Physics Letters*, vol. 96, no. 19, p. 193104, 2010.
- [106] S. Upadhyay, T. S. Jespersen, M. H. Madsen, P. Krogstrup, and J. Nygård, "Low temperature transport in p-doped inas nanowires," *Applied Physics Letters*, vol. 103, p. 162104, Jan. 2013.
- [107] B. Ketterer, E. Mikheev, E. Uccelli, and A. F. i. Morral, "Compensation mechanism in silicon-doped gallium arsenide nanowires," *Applied Physics Letters*, vol. 97, no. 22, p. 223103, 2010.
- [108] E. Dimakis, M. Ramsteiner, C.-N. Huang, A. Trampert, A. Davydok, A. Biermanns, U. Pietsch, H. Riechert, and L. Geelhaar, "In situ doping of catalyst-free inas nanowires with si: Growth, polytypism, and local vibrational modes of si," *Applied Physics Letters*, vol. 103, p. 143121, Jan. 2013.
- [109] J. Wallentin, M. Ek, L. R. Wallenberg, L. Samuelson, and M. T. Borgström, "Electron trapping in inp nanowire fets with stacking faults," *Nano Letters*, vol. 12, pp. 151–155, February 2012.

Bibliography

- [110] M. T. Borgstrom, E. Norberg, P. Wickert, H. A. Nilsson, J. Tragardh, K. A. Dick, G. Statkute, P. Ramvall, K. Deppert, and L. Samuelson, "Precursor evaluation for in situ InP nanowire doping," *Nanotechnology*, vol. 19, p. 445602, Sept. 2008.
- [111] H. Ghoneim, P. Mensch, H. Schmid, C. D. Bessire, R. Rhyner, A. Schenk, C. Rettner, S. Karg, K. E. Moselund, H. Riel, and M. T. Björk, "In situ doping of catalyst-free InAs nanowires," *Nanotechnology*, vol. 23, p. 505708, Nov. 2012.
- [112] D. E. Perea, E. R. Hemesath, E. J. Schwalbach, J. L. Lensch-Falk, P. W. Voorhees, and L. J. Lauhon, "Direct measurement of dopant distribution in an individual vapour-liquid-solid nanowire," *Nature Nanotechnology*, vol. 4, pp. 315–319, May 2009.
- [113] E. J. Schwalbach and P. W. Voorhees, "Doping nanowires grown by the vapor-liquid-solid mechanism," *Applied Physics Letters*, vol. 95, no. 6, p. 063105, 2009.
- [114] F. E. Rosztochy and K. B. Wolfstirn, "Distribution Coefficient of Germanium in Gallium Arsenide Crystals Grown from Gallium Solutions," *Journal of applied physics*, vol. 42, p. 426, Jan. 1971.
- [115] J. Wallentin and M. T. Borgstrom, "Doping of semiconductor nanowires," *Journal of Material Research*, vol. 26, pp. 2142–2156, sep 2011.
- [116] J. E. Allen, D. E. Perea, E. R. Hemesath, and L. J. Lauhon, "Nonuniform nanowire doping profiles revealed by quantitative scanning photocurrent microscopy," *Advanced Materials*, vol. 21, no. 30, pp. 3067–3072, 2009.
- [117] S. Vinaji, A. Lochthofen, W. Mertin, I. Regolin, C. Gutsche, W. Prost, F. J. Tegude, and G. Bacher, "material and doping transitions in single GaAs-based nanowires probed by kelvin probe force microscopy," *Nanotechnology*, vol. 20, no. 38, p. 385702, 2009.
- [118] S. Yu, T. Y. Tan, and U. Gosele, "Diffusion mechanism of zinc and beryllium in gallium arsenide," *Journal of Applied Physics*, vol. 69, pp. 3547–3565, mar 1991.
- [119] O. Salehzadeh, M. X. Chen, K. L. Kavanagh, and S. P. Watkins, "Rectifying characteristics of Te-doped GaAs nanowires," *Applied Physics Letters*, vol. 99, no. 18, p. 182102, 2011.
- [120] J. A. Czaban, D. A. Thompson, and R. R. LaPierre, "GaAs core-shell nanowires for photovoltaic applications," *Nano Letters*, vol. 9, no. 1, pp. 148–154, 2009.
- [121] S. M. Sze, *Semiconductor Devices: Physics and Technology*. John Wiley and Sons, 2001.
- [122] G. Landgren, R. Ludeke, Y. Jugnet, J. F. Morar, and F. J. Himpsel, "The oxidation of GaAs(110): A reevaluation," *Journal of Vacuum Science Technology B: Microelectronics and Nanometer Structures*, vol. 2, pp. 351–358, jul 1984.
- [123] M. Heiss, C. Colombo, and A. F. i Morral, "Nanowire based heterostructures: fundamental properties and applications," *Nanoepitaxy: Materials and Devices III, Proceeding of SPIE*, pp. 8106, 810603–1, 2011.

- [124] M. T. Bjork, H. Schmid, J. Knoch, H. Riel, and W. Riess, "Donor deactivation in silicon nanostructures," *Nature Nanotechnology*, vol. 4, pp. 103–107, Feb. 2009.
- [125] H. Demers, N. Poirier-Demers, D. Drouin, and N. de Jonge, "Simulating stem imaging of nanoparticles in micrometers-thick substrates," *Microscopy and Microanalysis*, vol. 16, p. 795, February 2010.
- [126] K. Tateno, H. Gotoh, and Y. Watanabe, "Gaas/algaas nanowires capped with algaas layers on gaas(311)b substrates," *Applied Physics Letters*, vol. 85, p. 1808, February 2004.
- [127] A. Green and W. Spicer, "Do we need a new methodology for gaas passivation?," *Journal of Vacuum Science Technology A: Vacuum, Surfaces, and Films*, vol. 11, pp. 1061–1069, Jul 1993.
- [128] S. Breuer, C. Pfüller, T. Flissikowski, O. Br, and t, "Suitability of Au-and self-assisted GaAs nanowires for optoelectronic applications," *Nano Letters*, vol. 11, pp. 1276–1279, Jan. 2011.
- [129] P. Parkinson, H. J. Joyce, Q. Gao, H. H. Tan, X. Zhang, J. Zou, C. Jagadish, L. M. Herz, and M. B. Johnston, "Carrier Lifetime and Mobility Enhancement in Nearly Defect-Free Core-Shell Nanowires Measured Using Time-Resolved Terahertz Spectroscopy," *Nano Letters*, vol. 9, pp. 3349–3353, Sept. 2009.
- [130] L. Titova, T. Hoang, and H. Jackson, "Temperature dependence of photoluminescence from single core-shell GaAs–AlGaAs nanowires," *Applied Physics Letters*, vol. 89, p. 173126, Jan. 2006.
- [131] N. Jiang, Q. Gao, P. Parkinson, J. Wong-Leung, S. Mokkaṭṭi, S. Breuer, H. H. Tan, C. L. Zheng, J. Etheridge, and C. Jagadish, "Enhanced Minority Carrier Lifetimes in GaAs/Al-GaAs Core–Shell Nanowires through Shell Growth Optimization," *Nano Letters*, vol. 13, pp. 5135–5140, Nov. 2013.
- [132] E. Russo-Averchi, M. Heiss, L. Michelet, P. Krogstrup, J. Nygard, C. Magen, J. Ramon Morante, E. Uccelli, J. Arbiol, and A. Fontcuberta i Morral, "Suppression of three dimensional twinning for a 100nanowires on silicon," *Nanoscale*, vol. 4, pp. 1486–1490, jan 2012.
- [133] K. A. Walsh, *Beryllium chemistry and processing*. ASM International, 2009.
- [134] B. Ketterer, E. Uccelli, and A. Fontcuberta i Morral, "Mobility and carrier density in p-type gaas nanowires measured by transmission raman spectroscopy," *Nanoscale*, vol. 4, pp. 1789–1793, jan 2012.
- [135] M. Ilegems, "Beryllium doping and diffusion in molecular-beam epitaxy of gaas and al_xga_{1-x}as," *Journal of Applied Physics*, vol. 48, no. 3, pp. 1278–1287, 1977.

Bibliography

- [136] M. Kazuya, K. Makoto, and T. Kiyoshi, "Diffusion of beryllium into gaas during liquid phase epitaxial growth of p-ga0.2al0.8as," *Journal of Applied Physics*, vol. 54, pp. 1574–1578, mar 1983.
- [137] E. Koren, J. K. Hyun, U. Givan, E. R. Hemesath, L. J. Lauhon, and Y. Rosenwaks, "Obtaining uniform dopant distributions in vls-grown si nanowires," *Nano Letters*, vol. 11, no. 1, pp. 183–187, 2011.
- [138] P. Blanc, M. Heiss, C. Colombo, and A. Mallorquì, "Electrical contacts to single nanowires: a scalable method allowing multiple devices on a chip. application to a single nanowire radial p–i–n junction," *Int. J. Nanotechnology*, vol. 10, p. Nos. 5/6/7, February 2013.
- [139] N. Han, F. Wang, J. J. Hou, F. Xiu, S. Yip, A. T. Hui, T. Hung, and J. C. Ho, "Controllable p–n switching behaviors of gaas nanowires via an interface effect," *ACS Nano*, vol. 6, pp. 4428–4433, February 2012.
- [140] D. Drouin, A. R. Couture, D. Joly, X. Tastet, V. Aimez, and R. Gauvin, "Casino v2.42: a fast and easy-to-use modeling tool for scanning electron microscopy and microanalysis users," *Scanning*, vol. 29, no. 3, pp. 92–101, 2007.
- [141] L. Pfeiffer, K. West, and H. Stormer, "Electron mobilities exceeding $10^7 \text{ cm}^2/V \cdot \text{s}$ in modulation-doped GaAs," *Applied Physics Letters*, vol. 55, p. 1888, Jan. 1989.
- [142] R. Dingle, H. Störmer, and A. Gossard, "Electron mobilities in modulation-doped semiconductor heterojunction superlattices," *Applied Physics*, vol. 33, p. 665, Jan. 1978.
- [143] G. E. Stillman and C. M. Wolfe, "Electrical characterization of epitaxial layers," *Thin Solid Films*, vol. 31, pp. 69–88, Jan. 1976.
- [144] W. Walukiewicz, H. Ruda, J. Lagowski, and H. Gatos, "Electron mobility in modulation-doped heterostructures," *Physical Review B*, vol. 30, pp. 4571–4582, Jan. 1984.
- [145] S. Adachi, *Properties of Aluminium Gallium Arsenide*. Institution of Engineering and Technology, 1993.
- [146] S. Duenas, I. Izpura, J. Arias, L. Enriquez, and J. Barbolla, "Characterization of the DX centers in AlGaAs:Si by admittance spectroscopy," *J. Appl. Phys*, vol. 69, pp. 4300–4306, 1991.
- [147] J. Yang, L. Moudy, and W. Simpson, "Donor energy level for Se in $Ga_{1-x}Al_xAs$," *Applied Physics Letters*, vol. 40, p. 244, Jan. 1982.
- [148] E. Schubert and K. Ploog, "Shallow and deep donors in direct-gap n-type $Al_xGa_{1-x}As$: Si grown by molecular-beam epitaxy," *Physical Review B*, vol. 30, pp. 7021–7029, Dec. 1984.

- [149] A. J. Ritenour, J. W. Boucher, R. DeLancey, A. L. Greenaway, S. Aloni, and S. W. Boettcher, "Doping and electronic properties of GaAs grown by close-spaced vapor transport from powder sources for scalable III-V photovoltaics," *Energy Environ. Sci.*, vol. 8, pp. 278–285, Jan. 2015.
- [150] S. Morkötter, N. Jeon, D. Rudolph, and B. Loitsch, "Demonstration of confined electron gas and steep-slope behavior in delta-doped GaAs-AlGaAs core-shell nanowire transistors," *Nano Letters*, vol. 15, pp. 3295–3302, Jan. 2015.
- [151] G. Mie, "Beiträge zur Optik trüber Medien, speziell kolloidaler Metallösungen," *Ann. Phys.*, vol. 25, pp. 377–445, 1908.
- [152] R. Ritchie, "Plasma losses by fast electrons in thin films," *Physical Review*, vol. 106, Jan. 1957.
- [153] K. R. Catchpole and A. Polman, "Design principles for particle plasmon enhanced solar cells," *Applied Physics Letters*, vol. 93, no. 19, p. 191113, 2008.
- [154] J. A. Schuller, E. S. Barnard, W. Cai, Y. C. Jun, J. S. White, and M. L. Brongersma, "Plasmonics for extreme light concentration and manipulation," *Nature Materials*, vol. 9, pp. 193–204, Feb. 2010.
- [155] S. Mokkalapati, F. J. Bech, R. de Waele, A. Polman, and K. R. Catchpole, "Resonant nano-antennas for light trapping in plasmonic solar cells," *J. Phys. D: Appl. Phys.*, vol. 44, no. 9, p. 185101, 2011.
- [156] S. Brittman, H. Gao, E. C. Garnett, and P. Yang, "Absorption of light in a single-nanowire silicon solar cell decorated with an octahedral silver nanocrystal," *Nano Letters*, vol. 11, no. 12, pp. 5189–5195, 2011.
- [157] H. A. Atwater and A. Polman, "Plasmonics for improved photovoltaic devices," *Nature Materials*, vol. 9, pp. 205–213, Mar. 2010.
- [158] P. Mühlischlegel, H.-J. Eisler, O. J. F. Martin, B. Hecht, and D. W. Pohl, "Resonant Optical Antennas," *Science*, vol. 308, pp. 1607–1609, June 2005.
- [159] P. J. Schuck, D. P. Fromm, A. Sundaramurthy, G. S. Kino, and W. E. Moerner, "Improving the Mismatch between Light and Nanoscale Objects with Gold Bowtie Nanoantennas," *Physical Review Letters*, vol. 94, p. 017402, Jan. 2005.
- [160] T. Hanke, J. Cesar, V. Knittel, A. Trügler, U. Hohenester, A. Leitenstorfer, and R. Bratschkitsch, "Tailoring Spatiotemporal Light Confinement in Single Plasmonic Nanoantennas," *Nano Letters*, vol. 12, pp. 992–996, Feb. 2012.
- [161] L. Novotny and N. van Hulst, "Antennas for light," *Nature Photonics*, vol. 5, pp. 83–90, Feb. 2011.

Bibliography

- [162] M. T. Borgström, V. Zwiller, E. Müller, and A. Imamoglu, "Optically Bright Quantum Dots in Single Nanowires," *Nano Letters*, vol. 5, pp. 1439–1443, July 2005.
- [163] A. Irrera, P. Artoni, F. Iacona, E. F. Pecora, G. Franzò, M. Galli, B. Fazio, S. Boninelli, and F. Priolo, "Quantum confinement and electroluminescence in ultrathin silicon nanowires fabricated by a maskless etching technique," *Nanotechnology*, vol. 23, p. 075204, Jan. 2012.
- [164] B. Tian, T. Kempa, and C. Lieber, "Single nanowire photovoltaics," *Chemical Society Reviews*, vol. 38, pp. 16–24, Jan. 2009.
- [165] J. Wallentin, N. Anttu, D. Asoli, M. Huffman, I. Aberg, M. Magnusson, G. Siefert, P. Fuss-Kailuweit, F. Dimroth, B. Witzigmann, H. Xu, L. Samuelson, K. Deppert, and M. Borgstrom, "Inp nanowire array solar cells achieving 13.8% efficiency by exceeding the ray optics limit," *Science*, vol. 339, pp. 1057–1060, March 2013.
- [166] M. D. Kelzenberg, S. W. Boettcher, J. A. Petykiewicz, D. B. Turner-Evans, M. C. Putnam, E. L. Warren, J. M. Spurgeon, R. M. Briggs, N. S. Lewis, and H. A. Atwater, "Enhanced absorption and carrier collection in Si wire arrays for photovoltaic applications," *Nature Materials*, vol. 9, pp. 239–244, Feb. 2010.
- [167] C. Winkelmann, I. Ionica, X. Chevalier, G. Royal, S. Bucher, and V. Bouchiat, "Optical Switching of Porphyrin-Coated Silicon Nanowire Field Effect Transistors," vol. 7, pp. 1454–1458, May 2007.
- [168] A. Greytak, C. Barrelet, Y. Li, and C. Lieber, "Semiconductor nanowire laser and nanowire waveguide electro-optic modulators," *Applied Physics Letters*, vol. 87, p. 151103, Jan. 2005.
- [169] R. Yan, D. Gargas, and P. Yang, "Nanowire photonics," *Nature Photonics*, vol. 3, pp. 569–576, Oct. 2009.
- [170] L. Cao, P. Fan, A. P. Vasudev, J. S. White, Z. Yu, W. Cai, J. A. Schuller, S. Fan, and M. L. Brongersma, "Semiconductor Nanowire Optical Antenna Solar Absorbers," *Nano Letters*, vol. 10, pp. 439–445, Feb. 2010.
- [171] G. Bronstrup, N. Jahr, C. Leiterer, A. Csáki, and W. Fritzsche, "Optical properties of individual silicon nanowires for photonic devices," *ACS Nano*, vol. 4, pp. 7113–7122, Jan. 2010.
- [172] A. V. Maslov and C. Z. Ning, "Reflection of guided modes in a semiconductor nanowire laser," *Applied Physics Letters*, vol. 83, p. 1237, Jan. 2003.
- [173] D. Saxena, S. Mokkalapati, P. Parkinson, N. Jiang, Q. Gao, H. H. Tan, and C. Jagadish, "Optically pumped room-temperature GaAs nanowire lasers," *Nature Photonics*, vol. 7, pp. 963–968, Nov. 2013.

- [174] C. F. Bohren and D. R. Huffman, *Absorption and Scattering of Light by Small Particles*. Wiley: Hoboken, 2004.
- [175] S. Mokkalapati, D. Saxena, N. Jiang, P. Parkinson, J. Wong-Leung, Q. Gao, H. H. Tan, and C. Jagadish, "Polarization Tunable, Multicolor Emission from Core–Shell Photonic III–V Semiconductor Nanowires," *Nano Letters*, vol. 12, pp. 6428–6431, Dec. 2012.
- [176] R. Zia, J. Schuller, and M. Brongersma, "Near-field characterization of guided polariton propagation and cutoff in surface plasmon waveguides," *Physical Review B*, vol. 74, Oct. 2006.
- [177] S. A. Maier, *Plasmonics: Fundamentals and Applications*. Springer: New York, 2007.
- [178] L. D. Negro and S. V. Boriskina, "Deterministic aperiodic nanostructures for photonics and plasmonics applications," *Laser & Photonics Reviews*, vol. 6, pp. 178–218, Apr. 2012.
- [179] P. Fan, C. Colombo, K. C. Huang, P. Krogstrup, J. Nygård, A. F. Morral, and M. L. Brongersma, "An Electrically-Driven GaAs Nanowire Surface Plasmon Source," *Nano Letters*, vol. 12, pp. 4943–4947, Sept. 2012.
- [180] J. Hyun and L. Lauhon, "Spatially Resolved Plasmonically Enhanced Photocurrent from Au Nanoparticles on a Si Nanowire," *Nano Letters*, vol. 11, pp. 2731–2734, June 2011.
- [181] M. W. Knight, N. K. Grady, R. Bardhan, F. Hao, P. Nordlander, and N. J. Halas, "Nanoparticle-Mediated Coupling of Light into a Nanowire," *Nano Letters*, vol. 7, pp. 2346–2350, Aug. 2007.
- [182] E. D. Palik, *Handbook of Optical Constants of Solids*. Academic Press; 1 edition, 1997.
- [183] P. Johnson and R. Christy, "Optical constants of the noble metals," *Physical Review B*, vol. 6, Jan. 1972.
- [184] G. Chen, J. Wu, Q. Lu, H. R. Gutierrez, Q. Xiong, M. E. Pellen, J. S. Petko, D. H. Werner, and P. C. Eklund, "Optical Antenna Effect in Semiconducting Nanowires," *Nano Letters*, vol. 8, pp. 1341–1346, May 2008.
- [185] G. Bronstrup, C. Leiterer, N. Jahr, C. Gutsche, A. Lysov, I. Regolin, W. Prost, F. J. Tegude, W. Fritzsche, and S. Christiansen, "A precise optical determination of nanoscale diameters of semiconductor nanowires," *Nanotechnology*, vol. 22, p. 385201, Aug. 2011.
- [186] P. Lautenschlager, M. Garriga, S. Logothetidis, and M. Cardona, "Interband critical points of GaAs and their temperature dependence," vol. 35, p. 17, Mar. 2011.
- [187] S. Bergfeld and W. Daum, "Second-Harmonic Generation in GaAs: Experiment versus Theoretical Predictions of $\chi_{xyz}(2)$," *Physical Review Letters*, vol. 90, p. 3, Jan. 2003.
- [188] J. Dadap, "Optical second-harmonic scattering from cylindrical particles," *Physical Review B*, vol. 78, p. 205322, Nov. 2008.

Bibliography

- [189] B. K. Canfield, H. Husu, J. Laukkanen, B. Bai, M. Kuittinen, J. Turunen, and M. Kauranen, "Local Field Asymmetry Drives Second-Harmonic Generation in Noncentrosymmetric Nanodimers," *Nano Letters*, vol. 7, pp. 1251–1255, May 2007.
- [190] S. Kühn, U. Håkanson, L. Rogobete, and V. Sandoghdar, "Enhancement of Single-Molecule Fluorescence Using a Gold Nanoparticle as an Optical Nanoantenna," *Physical Review Letters*, vol. 97, p. 017402, July 2006.
- [191] O. L. Muskens, V. Giannini, J. A. Sánchez-Gil, and J. G. Rivas, "Strong Enhancement of the Radiative Decay Rate of Emitters by Single Plasmonic Nanoantennas," *Nano Letters*, vol. 7, pp. 2871–2875, Sept. 2007.
- [192] A. G. Curto, G. Volpe, T. H. Taminiau, M. P. Kreuzer, R. Quidant, and N. F. van Hulst, "Unidirectional Emission of a Quantum Dot Coupled to a Nanoantenna," *Science*, vol. 329, pp. 930–933, Aug. 2010.
- [193] H. Hofmann, T. Kosako, and Y. Kadoya, "Design parameters for a nano-optical Yagi-Uda antenna," *New Journal of Physics*, vol. 9, Jan. 2007.
- [194] G. Grzela, *Directional light emission and absorption by semiconductor nanowires*. PhD thesis, FOM Institute AMOLF, 2013.
- [195] J. A. Stratton, *Electromagnetic Theory. International Series in Pure and Applied Physics*. McGraw-Hill Book Company, 1941.
- [196] M. Ramezani, A. Casadei, G. Grzela, and F. Matteini, "Hybrid semiconductor nanowire-metallic Yagi-Uda antennas," *Nano Letters*, vol. 15, pp. 4889–4895, Jan. 2015.
- [197] S. Mokkaṭpati, D. Saxena, H. H. Tan, and C. Jagadish, "Design considerations for semiconductor nanowire-plasmonic nanoparticle coupled systems for high quantum efficiency nanowires.," *Small*, vol. 9, pp. 3964–3969, Dec. 2013.
- [198] S. A. Mann and E. C. Garnett, "Extreme light absorption in thin semiconductor films wrapped around metal nanowires.," *Nano Letters*, vol. 13, pp. 3173–3178, July 2013.
- [199] P. Bharadwaj, B. Deutsch, and L. Novotny, "Optical Antennas.," *Advances in Optics and Photonics*, vol. 1, p. 438, Jan. 2009.
- [200] A. Casadei, E. F. Pecora, J. Trevino, C. Forestiere, D. Ruffer, E. Russo, F. Matteini, G. Tutuncuoglu, M. Heiss, A. Fontcuberta i Morral, and L. Dal Negro, "Photonic-plasmonic coupling of GaAs single nanowires to optical nanoantennas.," *Nano Letters*, vol. 14, no. 5, pp. 2271–2278, 2014.
- [201] S. Heeg, A. Oikonomou, R. Fernandez-Garcia, C. Lehmann, S. A. Maier, A. Vijayaraghavan, and S. Reich, "Plasmon-enhanced raman scattering by carbon nanotubes optically coupled with near-field cavities.," *Nano Letters*, vol. 14, pp. 1762–1768, Apr. 2014.

- [202] C. J. Barrelet, J. Bao, M. Lončar, H.-G. Park, F. Capasso, and C. M. Lieber, "Hybrid Single-Nanowire Photonic Crystal and Microresonator Structures," *Nano Letters*, vol. 6, pp. 11–15, Jan. 2006.
- [203] J. C. Johnson, H.-J. Choi, K. P. Knutsen, R. D. Schaller, P. Yang, and R. J. Saykally, "Single gallium nitride nanowire lasers," *Nature Materials*, vol. 1, pp. 106–110, Sept. 2002.
- [204] B. Mayer, D. Rudolph, J. Schnell, and S. Morkötter, "Lasing from individual GaAs-AlGaAs core-shell nanowires up to room temperature," *Nature Communication*, vol. 4, Jan. 2013.
- [205] T. J. Kempa, J. F. Cahoon, S. K. Kim, R. W. Day, D. C. Bell, H. G. Park, and C. M. Lieber, "Coaxial multishell nanowires with high-quality electronic interfaces and tunable optical cavities for ultrathin photovoltaics," *PNAS*, vol. 109, pp. 1407–1412, Jan. 2012.
- [206] S. Kim, R. Day, J. Cahoon, T. J. Kempa, K. Song, H.-G. Park, and C. M. Lieber, "Tuning Light Absorption in Core/Shell Silicon Nanowire Photovoltaic Devices through Morphological Design," *Nano Letters*, vol. 12, pp. 4971–4976, Aug. 2012.
- [207] M. D. Kelzenberg, D. B. Turner-Evans, M. C. Putnam, S. W. Boettcher, R. M. Briggs, J. Y. Baek, N. S. Lewis, and H. A. Atwater, "High-performance Si microwire photovoltaics," *Energy & Environmental Science*, vol. 4, p. 866, Jan. 2011.
- [208] M. Heiss and A. Fontcuberta i Morral, "Fundamental limits in the external quantum efficiency of single nanowire solar cells," *Applied Physics Letters*, vol. 99, p. 263102, Jan. 2011.
- [209] W. F. Liu, J. I. Oh, and W. Z. Shen, "Light absorption mechanism in single c-Si (core)/a-Si (shell) coaxial nanowires," *Nanotechnology*, vol. 22, pp. 125705–5, Feb. 2011.
- [210] H. C. Casey, D. D. Sell, and K. W. Wecht, "Concentration dependence of the absorption coefficient for n- and p-type GaAs between 1.3 and 1.6 eV.," *Journal of applied physics*, vol. 46, p. 250, Jan. 1975.
- [211] C. Forestiere *et al.*, "Genetically Engineered Plasmonic Nanoarrays.," *Nano Letters*, vol. 12, pp. 2037–2044, Apr. 2012.
- [212] Y.-F. Huang, C.-Y. Chen, L.-C. Chen, K.-H. Chen, and S. Chattopadhyay, "Plasmon management in index engineered 2.5D hybrid nanostructures for surface-enhanced Raman scattering," *NPG Asia Materials*, vol. 6, p. e123, Sept. 2014.
- [213] J. Bures, *Guided optics*. Wiley-VCH, 2009.

A List of publications

During my work on the present thesis I authored or co-authored the following publications. The thesis is based on a subset of these.

1. A. Casadei*, P. Krogstrup*, M. Heiss, J. A. Rohr, C. Colombo, T. Ruelle, S. Uphadyay, C. B. Sorensen, J. Nygard, A. F. i Morral, *Doping incorporation paths in catalyst-free Be-doped GaAs nanowires*, **Appl. Phys. Lett**, **102**, 013117 (2013);
2. A. Casadei, J. Schwender, E. Russo-Averchi, D. Ruffer, M. Heiss, E. Alarcon-Llado, F. Jabeen, M. Ramezani, K. Nielsch and A. F. i Morral, *Electrical transport in C-doped GaAs nanowires: surfaces effects*, **Phys. Status Solidi RRL** **7**, 10, 890-893 (2013);
3. A. Casadei*, E. F. Pecora*, J. Trevino*, C. Forestiere, D. Ruffer, E. Russo-Averchi, F. Matteini, G. Tutuncuoglu, M. Heiss, A. F. i Morral and L. Dal Negro *Photonic-plasmonic coupling of GaAs single nanowires to optical nanoantennas*, **Nano Letters**, **14**, 2271-2278 (2014);
4. A. Casadei, E. Alarcon-Llado, F. Amaduzzi, E. Russo, D. Ruffer, M. Heiss, L. Dal Negro and A. Fontcuberta i Morral *Polaritation response of nanowires à la carte*, **Scientific Reports**, **5**, 7651 (2015);
5. J. L. Boland, S. Conesa-Boj, P. Parkinson, G. Tutuncuoglu, F. Matteini, D. Ruffer, A. Casadei, F. Amaduzzi, F. Jabeen, C. L. Davies, H. J. Joyce, L. M. Herz, A. Fontcuberta i Morral and M. B. Johnston, *Modulation doping of GaAs/AlGaAs core-shell nanowires with effective defect passivation and high electron mobility*, **Nano Letters**, **15**, 1336-1342, (2015);
6. M. Ramezani, A. Casadei, G. Grzela, F. Matteini, G. Tutuncuoglu, D. Ruffer, A. Fontcuberta i Morral and J. Gomez Rivas, *Hybrid semiconductor nanowire-metallic Yagi-Uda*

Appendix A. List of publications

antennas, **Nano Letters**, **15**, 4889-4895 (2015).

B List of conferences and seminars

1. **Frontiers in Nanophotonics**, Ascona (CH), 30 August - 4 September 2015,
Poster "*Nanoantennas and nanowires integration for light engineering*";
2. **2015 MRS Spring Meeting & Exhibit**, San Francisco (US), 6-10 April 2015,
Oral presentation "*Nanowire/nanoantennas: unconventional light interaction*";
Oral presentation "*Engineer light interaction: a new system at the nanoscale*";
3. **8th Nanowire Growth Workshop**, Eindhoven (NE), 25-29 August 2014,
Oral presentation "*Nanowire/nanoantennas: unconventional light interaction*";
Poster "*Doping in GaAs nanowires and surface effects*";
4. **University of Canberra**, Canberra (AU), 14 January 2014,
Seminar "*Control and engineering the electronic properties of GaAs nanowires*";
5. **EDMX Research Day**, Lausanne (CH), 25 October 2013,
Oral presentation "*Light coupling in single nanowire with metal nano-antennas*";
6. **International Conference on One-Dimensional Nanomaterials (ICON)**, Annecy (FR),
23-26 September 2013,
Oral presentation "*Engineering light coupling in single nanowire with metal nano-antennas*";
7. **7th Nanowire Growth Workshop**, Lausanne (CH), 10-12 June 2013,
Poster "*Doping in GaAs nanowires and surface effects*";
8. **E-MRS**, Strasbourg (FR), 27-31 May 2013,
Oral presentation "*Electrical properties of Carbon doped GaAs nanowires and related heterostructures*";
9. **5th Plenary Workshop of the GdR**, Montpellier (FR), 2-5 April 2013,
Oral presentation "*Electrical properties of Carbon doped GaAs nanowires and surface effects*";

Appendix B. List of conferences and seminars

10. **Nanowire2012 (NW12)**, Berlin (DE), 19-21 September 2012,
Poster "*Doping incorporation and acceptor deactivation in Be-doped GaAs nanowires*";
11. **International Conference on the Physics of Semiconductors (ICPS)**, Zurich (CH), July
29th - August 3rd 2012,
Poster "*Doping mechanisms in GaAs Nanowires*";

Alberto Casadei

Av. D'Echallens 35, 1004, Lausanne, Switzerland

+41 78 61 88 059

albicasadei@gmail.com

Skype - alberto_casadei



Key Skills:

- ✓ Ph.D. in Engineering, Master in Physics
- ✓ Optical and electrical characterization of nanostructures
- ✓ Broad international experience, proven team work attitude

2011 – Present: (4 years)

École Polytechnique Fédérale de Lausanne, EPFL (CH)

Ph.D. in Material Science and Engineering

Investigation of nanostructures from physical properties to applications

- **Optical and electrical measurements of nanostructures:**
Resistivity Measurements, Four Probes, Photoconductivity, Field Effect Transistor, Solar Cell Absorption, Second Harmonic Generation, SEM, EBIC, Dark Scattering.
- **Problem solving**
Designed a new setup for solar cell characterizations, increased the nanowire absorption of 300%; Designed special sample holder for electrical measurements in a SEM chamber.
- **Team leading**
Coordinator of master student projects, defined research projects and found international collaborations; Organizer of a material science program (2015): “*New materials from Physics to Applications*”.
- **Responsible of the opto-electric laboratory**
Installed a new optical setup for nano-scale detectors characterization; Purchasing coordinator for laboratory’s equipment (± 100 K€ / annum).
- **Data analysis and simulations of physical phenomena**
Analyze data with Mathematica and R, find regressions and correlations; present in graphics and figures; Simulations of physical systems with NextNano, Comsol Multiphysics and Mathematica.
- **Write articles and make Oral Presentations**
Daily prepare oral presentations for collaborators, team work, efficient to obtain results, write scientific papers, respond to referees requests.

2010 – 2011: (1 year)

Stanford University (USA)

Researcher in Material Science (Exchange Program)

Realization of a new generation of low cost flexible solar cells

- **Analysis of organic polymer**
Device fabrication and characterization (AFM, X-Ray Spectroscopy and electrical meas.)

2006 – 2011: (5 years)

Bologna University (IT)

Bachelor and Master Degree in Physics (cum laude, 110/110)

Statistic, math and physics background

Competences:

- **Six years’ experience in micro- and nano-technology:** fabrication and characterization of solar cells, transistors, detectors and antennas.
- **Four years’ clean room experience in fabrication:** Thermal and E-beam evaporation, E-beam lithography, photo-lithography, SEM, wet etching.
- **Computer skills:** R, Excel, Power Point, Origin, SQL, C++, Python, Illustrator, Photoshop, Comsol Multiphysics, Mathematica, Latex, NextNano.

Alberto Casadei

Av. D'Echallens 35, 1004, Lausanne, Switzerland

+41 78 61 88 059

albicasadei@gmail.com

Skype - alberto_casadei

Languages:

English (Fluent), French (Advanced), Italian (mother tongue)

Awards:

2014 – Best publication of the year in the journal '*Physica Status Solidi*'

2010-2011 – First Italian award form: '*Italian Scientists and Scholars of North America Foundation*' (ISSNAF)

2010 – Scholarship: '*Alma Mater Studiorum*', merit award for the year.

2006 – '*Math and Physics Olympic Games*' (Top 100 students in Italy)

Extra activities:

Athletics. Competing in the Italian national championship (Top 20 at 800 meters)

Water-polo player on Lausanne Team (Regional league)

Personal Situation:

Age: 28, Nationality: Italian, Swiss permit: B, Status: Single